

Molecular deuterations in massive Starless Clump Candidates

KAI YANG,^{1,2,3,*} JUNZHI WANG,⁴ KEPING QIU,^{1,2,†} AND TIANWEI ZHANG^{3,5}

¹*School of Astronomy and Space Science, Nanjing University, 163 Xianlin Avenue, Nanjing 210023, P.R.China*

²*Key Laboratory of Modern Astronomy and Astrophysics (Nanjing University), Ministry of Education, Nanjing 210023, P.R.China*

³*I. Physikalisches Institut, Universität zu Köln, Zùlpicher Str. 77, 50937 Köln, Germany*

⁴*School of Physical Science and Technology, Guangxi University, Nanning 530004, P.R.China*

⁵*Research Center for Intelligent Computing Platforms, Zhejiang Laboratory, Hangzhou 311100, P.R.China*

ABSTRACT

Deuterated molecules are valuable probes for investigating the evolution and the kinematics in the earliest stages of star formation. In this study, we conduct a comprehensive investigation by performing a single point survey of 101 starless clump candidates, and carrying out on-the-fly (OTF) observations of 11 selected sources, focusing on deuterated molecular lines using the Institut de Radioastronomie Millimétrique (IRAM) 30-m telescope. In the single-point observation, we make 46 detections for DCO⁺ $J=1-0$, 12 for DCN $J=1-0$, 51 for DNC $J=1-0$, 7 for N₂D⁺ $J=1-0$, 20 for DCO⁺ $J=2-1$, and 10 for DCN $J=2-1$. The starless clump candidates (SCCs) with deuterated molecule detections exhibit lower median kinetic temperatures and narrower H₂CO (1_(0,1)-0_(0,0)) median full width at half maximum (FWHM) compared to those without such detections, while simultaneously displaying similar median values of 1.1mm intensity, mass, and distance. Furthermore, our OTF observations reveal that deuterated molecules predominantly have peaks near the 1.1mm continuum peaks, with the DCO⁺ $J=1-0$ emission demonstrating higher intensity in the deuterated peak region compared to the DCN and DNC $J=1-0$ emissions. Additionally, the majority of emissions from deuterated molecules and ¹³C-isotopologues exhibit peak positions close to those of the 1.1mm continuum peaks. By analyzing the 20''×20'' regions with strongest deuterated emissions in the OTF observations, we estimated deuterated abundances of 0.004–0.045, 0.011–0.040, and 0.004–0.038 for D_{frac}(HCN), D_{frac}(HCO⁺), and D_{frac}(HNC), respectively. The differential detection of deuterated molecular lines in our OTF observations could be attributed to variations in critical densities and formation pathways.

Keywords: Massive stars (732); Interstellar abundances (832); Interstellar molecules (849); Stars formation (1569)

1. INTRODUCTION

High-mass stars play a significant role in dominating the energetics of the interstellar medium (ISM) through their feedback mechanisms (e.g., Bolatto et al. 2013; Schilke 2015). Several theories have been developed to investigate the formation of high-mass stars (McKee & Tan 2003; Belloche et al. 2006; Smith et al. 2009; Motte et al. 2018; Padoan et al. 2020). A pivotal difference among these models lies in their treatment of the early stage of this process. However, our comprehension of the initial phases of high-mass star formation remains incomplete when derived from observation. Therefore, revealing initial conditions of massive stars is paramount to gaining insights into their formation process.

During early stages of high-mass star forming regions, they are deeply embedded in their parental molecular clouds. Consequently, recent observational studies focus on studying the cold gas (e.g., Wienen et al. 2021; Galloway-Sprietsma et al. 2022; Sakai et al. 2022; van Gelder et al. 2022; Giers et al. 2023) and dust (e.g., Svoboda et al. 2016; Sanhueza et al. 2019; Redaelli et al. 2022; Li et al. 2023; Morii et al. 2023) in high-mass star forming regions at (sub-)millimeter wavelengths.

* E-mail: kyang@nju.edu.cn

† E-mail: kpqiu@nju.edu.cn

Deuterated molecules are useful diagnostic tools for studying cold (~ 10 K) and dense environments ($n_{\text{H}_2} > 10^5 \text{ cm}^{-3}$) (e.g., Fontani et al. 2011; Pillai et al. 2011). Due to the small zero-point energy differences which ensure that deuterium is preferentially bonded into molecules compared to hydrogen, deuterated molecules can occur effectively at a previous cold phase in the molecular evolution of the gas with very low temperatures and D atoms in molecules can be much enhanced over the cosmic D/H abundance ratio, which is $\sim 1.5 \times 10^{-5}$ (Roberts & Millar 2000). At temperatures below 20 K and assuming low ortho-to-para H_2 ratio, deuterium fractionation increases mainly due to the effective reaction (Roberts & Millar 2000),



This reaction is exothermic, resulting in a significant increase in H_2D^+ abundance. Furthermore, under cold (< 10 K) and dense ($> 10^5 \text{ cm}^{-3}$) conditions, deuterium fractionation is further enhanced due to the depletion interaction between CO and H_2D^+ (e.g., Caselli et al. 1999). This explains why the processes that form the high abundances of several deuterated molecular lines occur in massive starless clumps and they are promising candidates for us to study the physical and kinematic conditions where star forms.

Various deuterated molecules have been studied towards star-forming regions at an early evolutionary stage, such as deuterated NH_3 (e.g., Busquet et al. 2010; Pillai et al. 2011; Li et al. 2022b), deuterated H_2CO (e.g., Roueff et al. 2007; Bergman et al. 2011; Zahorecz et al. 2021), deuterated CH_3OH (e.g., Bizzocchi et al. 2014; Fontani et al. 2015; van Gelder et al. 2022), DCN (e.g., Turner 2001; Gerner et al. 2015), DNC (e.g., Hirota et al. 2003; Sakai et al. 2012; Fontani et al. 2014), DCO^+ (e.g., Caselli et al. 2002; Miettinen et al. 2011) and N_2D^+ (e.g., Caselli et al. 2003; Crapsi et al. 2005; Albertsson et al. 2013). Among them, DCO^+ is thought to form in the gas phase and is expected to be abundant below ~ 30 K (Millar et al. 1989). The pathway of DCN is much more complicated and can form in both cold and warm regions (Willacy 2007; Roueff et al. 2013). In addition to this, due to their relatively high abundances and accessible rotational transitions, DCO^+ and DCN are among the primary tracers for studying the physical conditions in the early stage of massive star formation. N_2D^+ is frequently found in the early phases of protostellar cores (e.g., Fontani et al. 2011; Giannetti et al. 2019; Li et al. 2022a).

As powerful tracers of cold pre-stellar phase in star-forming regions, many deuterated molecules had been found in Galactic low-mass and high-mass star-forming regions in the past few decades (e.g., Caselli et al. 2003; Crapsi et al. 2005; Crapsi et al. 2007; Friesen et al. 2010), as well as in regions thought to be precursors of massive stars and stellar clusters (e.g., Fontani et al. 2006; Fontani et al. 2009; Fontani et al. 2011; Pillai et al. 2007; Pillai et al. 2012). Both DCN and DCO^+ have been observed toward proto-planetary disks (Huang et al. 2017). Observations of DCN have been done toward OMC-1 (Schilke et al. 1992) and Orion Bar (Leurini et al. 2006), and detections of DCO^+ have been confirmed toward dark clouds (Tin e et al. 2000; Turner 2001). However, there have been few surveys of deuterated molecules toward a sample of star-forming regions and the deuterium chemistry in high-mass star formation needs more investigations.

The deuterium fraction D_{frac} is a ratio between the abundance of a deuterated molecule and that of its hydrogenated counterpart. Many deuterated molecules (e.g., DCN and DCO^+) have been used to study their deuterium fractions. In an ALMA observation toward seven proto-planetary disks (Huang et al. 2017), $\text{DCO}^+/\text{HCO}^+$ and DCN/HCN abundance ratios range from 0.02–0.06 and 0.005–0.08, respectively. $\text{DCO}^+/\text{HCO}^+$ of 2 sources in Tin e et al. (2000) are 0.18 and 0.02. Observations of the abundance of interstellar deuterated molecules offer a valuable probe into the situation of star formation.

In this paper, we present the results of a single-point survey of deuterated molecular lines toward 101 massive starless clump candidates and OTF observations towards 11 selected sources. The outline of this paper is as follows: we introduce the observations and data reduction in Section 2 and describe the main results in Section 3. In Section 4, we present the analysis and discussion of the results, and a summary is given in Section 5.

2. SAMPLE AND OBSERVATIONS

Based on observational diagnostics related to star formation activity: compact $70 \mu\text{m}$ sources, mid-IR color-selected young stellar objects (YSOs), H_2O and CH_3OH masers, and UCH II regions, Svoboda et al. (2016) identified 2223 starless clump candidates devoid of indicators of star formation activities from the 1.1mm Bolocam Galactic Plane Survey. Furthermore, Calahan et al. (2018) blindly selected 101 targets from this SCC catalog, specifically those with $\text{NH}_3(1,1)$ detections, in order to investigate potential inflow signatures. In this study (Calahan et al. 2018), $\text{HCO}^+ J=1-0$ was detected in all sources, except for two sources with non-detections at the NH_3 velocity. In addition, six clumps exhibited blue asymmetric, self-absorbed line profiles in the presence of inflow.

The 101 massive starless clump candidates, listed in Table 1, are also chosen as our source sample. These targets are situated in the first quadrant of the Galactic plane, with a median distance of ~ 4.1 kpc. A comparison of the mass and mass surface density between the selected sample and the 2223 complete SCCs in Calahan et al. (2018) reveals that the selected sample adequately represents the mass range of the complete catalog. However, the selected sample exhibits higher peak mass surface densities, approximately twice as much as those found in the complete SCC sample. For the identification of line detection, the v_{LSR} of NH_3 reported in Svoboda et al. (2016) is regarded as the systemic velocity for each source.

Our observation was performed with the IRAM 30-m telescope at Pico Veleta, Spain, in May 2019. We checked the pointing about every two hours with nearby strong millimeter emitting quasi-stellar objects, and the focus after starting of the observation, sunrise, and sunset with Mars and Jupiter. We started from single-point line survey of deuterated molecular lines, such as DCN , DCO^+ , N_2D^+ $J=1-0$, and DCN , DCO^+ $J=2-1$ toward SCCs. A position-switching mode was used and each source was observed in two on-off cycles, with each cycle lasting four minutes. We set the off position ($1^\circ 0$, $0^\circ 0$) in R.A. and DEC. from the on position. The Eight Mixer Receiver (EMIR) with dual-polarization and the Fourier Transform Spectrometers (FTS) backend with 8 GHz frequency coverage and 195 kHz spectral resolution were used to record signals. The 3 mm (E0) band and 2 mm (E1) band of the EMIR receiver were used to cover two frequency ranges, 71.3-79 GHz and 138.3-146 GHz, respectively. The typical system temperatures are 134 K and 161 K at 72 GHz and 144 GHz, respectively. The beam sizes of the IRAM 30-m telescope are roughly $34''$ and $17''$ at 72 GHz and 144 GHz, respectively. The root-mean-square (rms) noise levels are 61.4 mK at 72 GHz and 66.9 mK at 144 GHz. The velocity resolution and aperture efficiency at different frequencies of deuterated molecular lines are shown in Table 2.

After single-point observation, we chose 11 sources with strong flux densities of DCO^+ and DNC $J=1-0$ or the most detection of the deuterated molecular lines and then carried out the on-the-fly (OTF) mode mapping observation toward them. We used the OTF PSW observing mode with EMIR to cover a field of view of $2' \times 2'$. The scan spacing is $6''$. The FTS backend with 8 GHz frequency coverage and 195 kHz spectral resolution was also used in our OTF mode mapping. On the one hand, we set the frequency ranges of EMIR to be the same as in single-point observation. We obtained a sensitivity of 44.3 mK (T_a^*) in 1.5 hours for each source and a system temperature of 183 K at 72 GHz. On the other hand, to cover H^{13}CN , H^{13}CO^+ $J=1-0$ and N_2D^+ $J=2-1$, we also mapped each source for 0.5 hours with two frequency ranges, 86-94 GHz and 148-156 GHz, set respectively for the 3 mm (E0) band and 2 mm (E1) band. The sensitivity was 60.2 mK and the system temperature was around 137 K at 87 GHz. Table 2 also lists the other detailed observational information on different molecular lines.

The CLASS and GREG packages of GILDAS¹ are used to reduce data from the single-point and OTF observation. We fit and subtract first-order polynomial baselines of the spectrum. The rest frequencies of the molecular lines from the Cologne Database for Molecular Spectroscopy (CDMS; Müller et al. 2001, 2005; Endres et al. 2016). The velocity-integrated intensities of these molecular lines are derived from a single-component Gaussian fit to the spectra. We convert the antenna temperature (T_a^*) to the main beam brightness temperature (T_{mb}) with $T_{\text{mb}} = T_a^* \cdot F_{\text{eff}}/B_{\text{eff}}$, where the forward efficiency (F_{eff}) and the beam efficiency (B_{eff}) from the IRAM 30-m homepage² are listed in Table 2. The final data cube is produced by combining all data and re-gridding the image to a pixel size of $10''$ at 3 mm band and $6''$ at 2 mm band, approximately one third of the beam sizes.

3. RESULTS

We made single-point observations towards the 101 starless clump candidates with the IRAM 30-m telescope and further conducted OTF mode observation towards 11 selected sources to obtain the spatial distribution of deuterated molecules and their ^{13}C -isotopologues. DCO^+ and DNC $J=1-0$ have higher detection rates than DCN and N_2D^+ $J=1-0$. $1-0$ rotational lines of deuterated molecules and ^{13}C -isotopologues have peaks near the 1.1 mm continuum peaks. The results of the single-point observations are described in Section 3.1 and the OTF mode observations are shown in Section 3.2.

3.1. Single-point observations

3.1.1. Deuterated molecules

¹ <http://www.iram.fr/IRAMFR/GILDAS>

² <http://www.iram.es/IRAMES/mainWiki/Iram30mEfficiencies>

In total, the DCO^+ , DCN , DNC , N_2D^+ $J=1-0$, and DCO^+ , DCN $J=2-1$ emissions are detected in 46, 12, 51, 7, 20, and 10 out of the 101 sources with velocity integrated intensities above $3\sigma_{\text{area}}$, respectively. The rms of the velocity integrated intensity σ_{area} is derived from the single component Gaussian fitting. Table 1 presents the detection status of these deuterated molecular lines and Figure 3–8 displays the detected spectra. Gaussian fitting parameters of DCO^+ , DCN , and DNC $J=1-0$ detections are listed in Table 3, and the results of N_2D^+ $J=1-0$, and DCO^+ , DCN $J=2-1$ detections are shown in Table 4. Owing to the limited signal-to-noise level and velocity resolution, we have not applied deconvolution to the data. As a result, we present the observed velocity width directly in the tables.

Among 101 SCCs observed, 64 of them exhibit detections of deuterated molecules (DCO^+ , DCN , DNC , N_2D^+), while 37 do not. We compare their physical properties obtained from Svoboda et al. (2016) and visualize the results in Figure 1. The SCCs with and without deuterated molecule detections share similar median values for three parameters, including 1.1 mm intensity (0.90 and 0.94 Jy), mass (246.2 and 266.9 M_{\odot}), and distance (4.3 and 4.1 kpc). However, the SCCs with deuterated molecule detections display a lower median kinetic temperature (13.2 K) obtained from NH_3 observations compared to those without such detections (15.7 K).

For the $1-0$ rotational lines of DCO^+ , DCN , DNC , and N_2D^+ , five sources, BGPS2940, BGPS2945, BGPS2986, BGPS3018, and BGPS3134, are detected with all four lines. Among the 101 sources, 5, 28, and 26 sources are detected with three, two, and one lines in the four $1-0$ rotational lines, respectively. We do not detect deuterated line emissions above $3\sigma_{\text{area}}$ towards the rest 37 sources.

Sources detected with emissions of DCO^+ and DCN $J=2-1$ are also detected with their $1-0$ rotational lines. For the 46 DCO^+ $J=1-0$ sources, the peak flux densities of 20 sources which are also detected with DCO^+ $J=2-1$ emissions have a range of 0.094 to 1.684 K, the remaining 26 sources without DCO^+ $J=2-1$ detection have peak flux densities ranging from 0.100 to 0.689 K. Among 12 DCN $J=1-0$ sources, there are 10 sources also detected with DCN $J=2-1$ emissions.

There are 39 sources detected with both DCO^+ and DNC $J=1-0$ emissions, and the peak flux density ratios of DCO^+/DNC range from 0.39 to 2.86 with a median value of 1.45, which indicates that DCO^+ $J=1-0$ mostly has a stronger emission than DNC $J=1-0$. DNC $J=1-0$ has a higher FWHM median value (1.6 km s^{-1}) than that of DCO^+ $J=1-0$ (1.2 km s^{-1}) towards these sources.

We present the integrated intensities of DCO^+ , DCN , and N_2D^+ $J=1-0$ in relation to DNC $J=1-0$ in Figure 2. The upper limit values for the non-detected lines are estimated by $3\sigma_{\text{area}}$. These relations could be fitted by the following equations: $\log(I_{\text{DCO}^+}) = 1.12 \times \log(I_{\text{DNC}}) + 0.06$, $\log(I_{\text{DCN}}) = 0.31 \times \log(I_{\text{DNC}}) - 0.53$, and $\log(I_{\text{N}_2\text{D}^+}) = 0.30 \times \log(I_{\text{DNC}}) - 0.55$. The positive slopes in these equations indicate that higher DNC $J=1-0$ integrated intensity is associated with a higher integrated intensity for the other three deuterated molecular lines. In addition, DCO^+ and DNC $J=1-0$ exhibit comparable integrated intensities, whereas the intensities of DCN , and N_2D^+ $J=1-0$ are comparatively weaker, which indicates that the molecular lines with higher detection rates have stronger intensities than those with lower detection rates.

3.1.2. H_2CO

Information from simultaneously obtained H_2CO ($1_{(0,1)}-0_{(0,0)}$) at 72.837951 GHz can be used to probe dense gas properties in these sources. H_2CO ($1_{(0,1)}-0_{(0,0)}$) emissions are detected in 91 sources with velocity integrated intensities above $3\sigma_{\text{area}}$, most of which can be fitted with a single-component Gaussian profile. Their parameters and spectra are shown in Table 5 and Figure 9. Sixty among these H_2CO ($1_{(0,1)}-0_{(0,0)}$) sources are detected with deuterated line emissions, their FWHMs range from 0.8 to 4.6 km s^{-1} with a median value of 2.1 km s^{-1} . For the remaining 31 sources, their FWHMs range from 0.8 to 4.8 km s^{-1} with a higher median value of 2.8 km s^{-1} .

In order to get a better understanding of the spatial distribution of these deuterated molecular lines in these regions at the early stage of star-formation, after taking the sources with strong emissions or most detection of the deuterated molecular lines into consideration, we finally choose 11 sources as our targets to conduct our continuous OTF mode observation.

3.2. OTF observations toward selected sources

Aiming to study the distribution of deuterated molecules, we made OTF observations towards 11 selected sources. Furthermore, pairs of DCO^+ and H^{13}CO^+ $J=1-0$ (3.2×10^4 and $6.2 \times 10^4 \text{ cm}^{-3}$), DCN and H^{13}CN $J=1-0$ (2.6×10^5 and $4.3 \times 10^5 \text{ cm}^{-3}$), DNC and HN^{13}C $J=1-0$ (8.2×10^4 and $9.6 \times 10^4 \text{ cm}^{-3}$) have similar critical densities at a temperature of 10 K, as reported in Feng et al. (2020). Therefore, the observations of these lines will help us figure out whether the critical densities influence the detectability of the deuterated molecules. Consequently, we focus on the spatial

distributions of deuterated molecules, namely, DCO^+ , DCN , DNC , and N_2D^+ , along with their ^{13}C -isotopologues, H^{13}CN , H^{13}CO^+ , and HN^{13}C , which are listed in Table 2. Figure 10 – 20 displays the maps of deuterated molecules and ^{13}C -isotopologues from the OTF observation toward the 11 sources, the centre point of each map is the 1.1 mm continuum peak for each source obtained from Svoboda et al. (2016). The regions enclosed by blue squares represent the peak regions of the deuterated molecular lines. The spectra averaged from these regions are presented in Figure 21. Their parameters are shown in Table 6. We also show the velocity field and line width maps in Figure 22–27 and Appendix B, these maps have at least five successive pixels with available values. The integrated maps of HCO^+ , HCN , and $\text{HNC } J=1-0$ are presented in the Appendix A, but we do not pay much attention to them because they are optically thick molecular lines.

3.2.1. Distributions among deuterated molecules

We have successfully mapped the $J=1-0$ line emissions of DCO^+ , DNC , DCN , and N_2D^+ towards 10, 11, 9, and 8 sources, respectively. These observations yield rms noise levels of approximately 0.05 K, as derived from line-free channels. In the following, we introduce the spatial distributions for each source, in conjunction with the 1.1mm continuum peak positions obtained from Svoboda et al. (2016).

BGPS2693

The DCO^+ and $\text{DNC } J=1-0$ emissions exhibit distinct morphologies, however, both peaking at the 1.1mm continuum peak position.

BGPS2931

The positions of highest intensity for deuterated molecules are detected to the southeast of the continuum peak, while $\text{DCO}^+ J=1-0$ exhibits more peaks.

BGPS2940

DCO^+ , DNC , DCN , and $\text{N}_2\text{D}^+ J=1-0$ exhibit significantly different morphologies, but their peaks are located near the continuum peak.

BGPS2945

The emissions of DCO^+ and $\text{DNC } J=1-0$ extend in the NE-SW direction with a signal-to-noise level exceeding 10. On the contrary, the clumpy DCN and $\text{N}_2\text{D}^+ J=1-0$ structures, at approximately 5 times the noise level ($\sim 5\sigma_{\text{area}}$), are detected with peaks immediately next to the continuum peak.

BGPS2984

All four lines exhibit peaks near the continuum peak, with an additional common peak to the northeast of the central position. Apart from DCO^+ and $\text{DNC } J=1-0$, DCN and $\text{N}_2\text{D}^+ J=1-0$ exhibit emissions with clumpy morphology, primarily due to limited signal-to-noise levels.

BGPS2986

The integrated maps of these four deuterated molecular lines show rounded morphologies, with peaks located at the 1.1mm continuum peak position.

BGPS3018

Both DCO^+ and $\text{DNC } J=1-0$ emissions exhibit two peaks on opposite sides of the 1.1mm continuum peak position, while several $\sim 3\sigma_{\text{area}}$ DCN clumpy structures are detected.

BGPS3110

DNC and $\text{DCN } J=1-0$ emissions both have peaks near the continuum peak, with $\text{DCN } J=1-0$ revealing more peaks. $\text{N}_2\text{D}^+ J=1-0$ is marginally detected.

BGPS3125

The emissions of DCO^+ , DNC , and $\text{DCN } J=1-0$ display different morphologies. DCO^+ and $\text{DNC } J=1-0$ have peaks at the 1.1 mm continuum peak position, while there is no clear correlation among other peaks.

BGPS3134

The emissions of DCO^+ , DNC , DCN , and $\text{N}_2\text{D}^+ J=1-0$ all extend from the mapping centre to the northwest, with peaks detected surrounding the continuum peak.

BGPS4402

The emissions of DCO^+ , DNC , and $\text{N}_2\text{D}^+ J=1-0$ display completely different morphologies. $\text{DNC } J=1-0$ has a peak at the continuum peak position, while DCO^+ and $\text{N}_2\text{D}^+ J=1-0$ do not.

For most of the sources (9 out of 11), considering one beam size, we have not found clear offsets between the peaks of the deuterated molecular lines and the 1.1mm continuum peaks. Additionally, for spectra averaged from regions with the highest deuterated molecular line intensities, the peak intensities of $\text{DCO}^+ J=1-0$ have a larger median value (0.759 K) compared to those of $\text{DNC } J=1-0$ (0.585 K) and $\text{DCN } J=1-0$ (0.252 K). In Figures 22–24, we observe clear NE-SW, E-W, and S-N oriented velocity gradients for BGPS2986, BGPS3018, and BGPS3134, respectively. Furthermore, in their line width maps, depicted in Figures 25–27, there is an enhancement towards the line peaks.

3.2.2. Distributions of deuterated molecules and ^{13}C -isotopologues

The investigation into deuterated molecules and ^{13}C -isotopologues, which are optically thin, could give clues about the distinctions between deuterated molecules and dense gas tracers. By considering the 1.1mm continuum peak positions, we gain insights into the relationship between these molecules and star formation activities. The ^{13}C lines exhibit rms noise levels of approximately 0.10 K, derived from line-free channels.

DCO⁺ and H¹³CO⁺ J=1-0

We detect DCO^+ and $\text{H}^{13}\text{CO}^+ J=1-0$ peaks in proximity to the 1.1mm continuum peak positions for eight sources, with the exception of BGPS3125 and BGPS4402. Two sources, BGPS2693 and BGPS4402, present distinctive morphologies for DCO^+ and H^{13}CO^+ . Moreover, in terms of the $\text{DCO}^+/\text{H}^{13}\text{CO}^+$ peak intensity ratio, seven out of ten sources display values greater than 1.

DNC and HN¹³C J=1-0

Among the eleven sources examined, seven exhibit DNC and $\text{HN}^{13}\text{C } J=1-0$ peaks close to the continuum peak. For BGPS2945, BGPS2984, BGPS2986, and BGPS3134, there is an absence of noticeable dissimilarity in the morphologies of the DNC and HN^{13}C emissions. However, in five sources, more HN^{13}C peaks are discerned than DNC peaks. In addition, eight out of eleven sources have a $\text{DNC}/\text{HN}^{13}\text{C}$ peak intensity ratio exceeding 1.

DCN and H¹³CN J=1-0

Out of the nine sources in which both DCN and $\text{H}^{13}\text{CN } J=1-0$ emissions were detected, five display DCN and H^{13}CN peaks near the 1.1mm continuum peak positions. Nevertheless, for each source, the morphologies of DCN and $\text{H}^{13}\text{CN } J=1-0$ exhibit striking dissimilarities. In particular, almost half of these sources feature a peak $\text{H}^{13}\text{CN } J=1-0$ intensity surpassing that of $\text{DCN } J=1-0$.

In summary, the majority of detected deuterated molecular line emissions and ^{13}C isotopologue emissions have peaks near the 1.1mm continuum peak positions. The peak intensities of DCN and $\text{H}^{13}\text{CN } J=1-0$ in the deuterated peak regions are comparable, while HCO^+ and HNC display deuterated molecular lines with stronger peak intensities than their ^{13}C isotopologues.

3.3. H44 α detection

Radio recombination lines (RRLs) are the tracers of H II regions, and can help us determine whether H II regions influence the appearance of deuterated molecules. The $\text{H}44\alpha$ line at 76.4 GHz is covered in our OTF observations and is detected in BGPS3110 and BGPS3125. We present $\text{H}44\alpha$ versus deuterated line emission distributions and averaged $\text{H}44\alpha$ spectra in the central regions ($20'' \times 20''$) in Figure 28. For BGPS3110, deuterated line emissions are detected primarily at the edge of $\text{H}44\alpha$ emissions. For BGPS3125, the $\text{H}44\alpha$ emissions are detected in a tiny area (radius of ~ 0.09 pc at a distance of ~ 3.5 kpc), which could be a UCH II region, and the deuterated line emissions are not detected towards this region. Thereby the emissions of the deuterated molecules are generated from the massive Starless Clump Candidates other than enhanced by the H II regions.

3.4. Column Density

In order to investigate the deuterated fraction in the peak regions of the deuterated molecules, we first need to derive their column densities. Assuming local thermodynamic equilibrium (LTE) conditions, and optically thin emission for deuterated molecules and ^{13}C -isotopologues, the column densities of the 1–0 molecular lines can be derived following Mangum & Shirley (2015):

$$N_{\text{tot}} = \left(\frac{3h}{8\pi^3 S \mu^2 R_i} \right) \left(\frac{Q(T_{\text{ex}})}{g_u} \right) \frac{\exp\left(\frac{E_u}{kT_{\text{ex}}}\right)}{\exp\left(\frac{h\nu}{kT_{\text{ex}}}\right) - 1} \times \frac{1}{(J_\nu(T_{\text{ex}}) - J_\nu(T_{\text{bg}}))} \int \frac{T_R dv}{f}, \quad (2)$$

where h is the Planck constant, S is the line strength for linear molecules, μ is the molecular electric dipole moment, the sum of relative intensities $R_i = 1$ for $\Delta J = 1$ transitions, $Q(T_{\text{ex}})$ is the partition function, g_u is the degeneracy of the upper state, E_u is the energy of the upper level energy, k is the Boltzmann constant, T_{ex} is the excitation temperature, ν is the rest frequency of the transition, $\int T_R dv$ is the integrated intensity, f is the filling factor assumed to be 1, $J_\nu(T)$ is the planck function, and $T_{bg} = 2.73$ K is the cosmic microwave background. We adopt the kinetic temperature derived from NH_3 observations in Svoboda et al. (2016) as the excitation temperature. For most sources, the uncertainty of the gas kinetic temperatures is lower than 3%. The spectroscopic parameters are obtained from the CDMS database (Müller et al. 2001, 2005; Endres et al. 2016) and JPL catalogues (Pickett et al. 1998).

The estimated column densities are shown in Table 7, ranging from 10^{11} to 10^{13} cm^{-2} . For H^{13}CN and DCN , the ranges of their column densities are $6.0 \times 10^{11} - 1.2 \times 10^{13}$ cm^{-2} and $9.8 \times 10^{11} - 3.0 \times 10^{12}$ cm^{-2} , respectively. And the medians are 1.1×10^{12} and 1.5×10^{12} cm^{-2} . $N(\text{H}^{13}\text{CO}^+)$ and $N(\text{DCO}^+)$ have ranges of $1.4 \times 10^{12} - 9.3 \times 10^{12}$ cm^{-2} and $1.2 \times 10^{12} - 7.6 \times 10^{12}$ cm^{-2} , respectively. Medians of them are 2.6×10^{12} and 3.8×10^{12} cm^{-2} . $N(\text{HN}^{13}\text{C})$ ranges from 8.6×10^{11} to 6.6×10^{12} cm^{-2} and $N(\text{DNC})$ ranges from 5.5×10^{11} to 3.6×10^{12} cm^{-2} . Their medians are 1.6×10^{12} and 2.2×10^{12} cm^{-2} . Most of the estimated column densities have errors lower than 15%. Although $N(\text{H}^{13}\text{CN})$ of BGPS3110 is the strongest, most of the column densities of H^{13}CN are comparable with the column density of HN^{13}C , and H^{13}CO^+ has the strongest column density. A similar relationship occurs in $N(\text{DCN})$, $N(\text{DNC})$, and $N(\text{DCO}^+)$. The column densities of DNC and HN^{13}C are consistent with the results of studies of massive clumps in the early evolutionary stages of high-mass star formation (e.g., Sakai et al. 2012, 2015) and cold dark cloud cores (e.g., Hirota et al. 2003; Vastel et al. 2016). There are also many works (e.g., Roberts et al. 2002; Roueff et al. 2007; Öberg et al. 2012; Ren et al. 2012; Gerner et al. 2014, 2015; Treviño-Morales et al. 2014; Huang et al. 2017) involving studies of $N(\text{DCN})$, $N(\text{H}^{13}\text{CN})$, $N(\text{DCO}^+)$ and $N(\text{H}^{13}\text{CO}^+)$, our results of column densities conform to those in early phases of massive star formation. In addition, $N(\text{HN}^{13}\text{C})/N(\text{H}^{13}\text{CN})$ has a median value of 1.4, which means that HN^{13}C $J=1-0$ has a higher column density than H^{13}CN $J=1-0$ for most sources.

According to Equation 2, the column density ratios between deuterated molecules and their ^{13}C -isotopologue counterparts can be expressed by integrated intensity ratios: $N(\text{DCO}^+)/N(\text{H}^{13}\text{CO}^+) = \sim 1.06 \times I(\text{DCO}^+)/I(\text{H}^{13}\text{CO}^+)$, $N(\text{DCN})/N(\text{H}^{13}\text{CN}) = \sim 1.31 \times I(\text{DCN})/I(\text{H}^{13}\text{CN})$, and $N(\text{DNC})/N(\text{H}^{13}\text{NC}) = \sim 0.97 \times I(\text{DNC})/I(\text{H}^{13}\text{NC})$. We have listed these integrated intensity ratios and the corresponding column density ratios in Table 8. The integrated intensity ratios for $\text{DCO}^+/\text{H}^{13}\text{CO}^+$ and $\text{DNC}/\text{HN}^{13}\text{C}$ closely mirror the column density ratios.

3.5. Deuterated fraction

The deuterated fraction (D_{frac}) is the column density ratio between a deuterated molecular line and its hydrogenated counterpart. With the derived $^{12}\text{C}/^{13}\text{C}$ ratio, we can estimate the deuterated fraction for the 11 selected sources in the OTF observations from the column density ratio between the deuterated molecular line and its ^{13}C -isotopologue. With the OTF observations, we can obtain the spatial distribution information of the lines and derive a more accurate deuterated fraction. The $^{12}\text{C}/^{13}\text{C}$ ratio is a useful tool for studying the stellar nucleosynthesis and chemical evolution of the Milky Way (Wilson & Rood 1994), and many observations indicate a gradient of $^{12}\text{C}/^{13}\text{C}$ ratios across the Galaxy (e.g., Wilson et al. 1976; Whiteoak & Gardner 1979; Henkel et al. 1980; Milam et al. 2005; Yan et al. 2023). We adopt the $^{12}\text{C}/^{13}\text{C}$ ratios by following the relationship in Milam et al. (2005):

$$^{12}\text{C}/^{13}\text{C} = 6.21D_{\text{GC}} + 18.71 \quad (3)$$

The distance from the Galactic center (D_{gc}) for each source can be estimated from the kinematic distance from Svoboda et al. (2016) and the distance from the sun to the Galactic center of $R_0 = 8.15$ kpc (Reid et al. 2019). The derived $^{12}\text{C}/^{13}\text{C}$ ratios are listed in Table 8. The $^{12}\text{C}/^{13}\text{C}$ ratios for the OTF sources have a range of 34.0 to 62.3.

Based on the $^{12}\text{C}/^{13}\text{C}$ ratios and the $N(\text{DCN})/N(\text{H}^{13}\text{CN})$, $N(\text{DCO}^+)/N(\text{H}^{13}\text{CO}^+)$, and $N(\text{DNC})/N(\text{HN}^{13}\text{C})$ values, we can derive the deuterated fractions (shown in Table 8). $D_{\text{frac}}(\text{HCN})$, $D_{\text{frac}}(\text{HCO}^+)$ and $D_{\text{frac}}(\text{HNC})$ have similar values of 0.004–0.045, 0.011–0.040, and 0.004–0.038, respectively. We show the deuterated fractions $D_{\text{frac}}(\text{HNC})$ versus $D_{\text{frac}}(\text{HCN})$, $D_{\text{frac}}(\text{HNC})$ versus $D_{\text{frac}}(\text{HCO}^+)$, and $D_{\text{frac}}(\text{HCO}^+)$ versus $D_{\text{frac}}(\text{HCN})$ in Figure 29. Both $D_{\text{frac}}(\text{HCN})$ and $D_{\text{frac}}(\text{HCO}^+)$ show increasing trends with $D_{\text{frac}}(\text{HNC})$ grows larger. Overall, although DNC and DCO^+ $J=1-0$ have a higher detection rate than DCN $J=1-0$, the estimated deuterated fractions are comparable.

4. DISCUSSION

4.1. Different detection rates for DCO^+ , DCN , and DNC

In our observations, the emissions of the deuterated molecular lines, DCO⁺, DCN, DNC, and N₂D⁺ $J=1-0$, have peaks at similar positions. But the DCO⁺ $J=1-0$ detection rate is higher than DCN $J=1-0$ in the single-point observations, with detection rates of DCO⁺, DCN, DNC, and N₂D⁺ $J=1-0$ are 45.5%, 11.9%, 50.5%, and 6.9%, respectively. In addition, the DCO⁺ emissions tend to have stronger intensities towards the central regions in the OTF observation, while almost half of the DCN $J=1-0$ emissions show clumpy structures with an intensity of $\sim 3\sigma_{\text{area}}$. The deuterated molecules have been treated as chemical clocks by several observations (e.g., Fuente et al. 2005; Belloche et al. 2006; Fontani et al. 2014; Sakai et al. 2022), and their detection difference is believed to be caused by deuterium chemistry (e.g., Gerner et al. 2015). In our study, different critical densities could be the main reason for the different detection rates.

The critical density of optically thin deuterated species in the absence of a background continuum can be understood through the equation $n_{\text{crit}} \sim A_{jk}/\gamma_{jk}$ (Shirley 2015), where A_{jk} represents the Einstein A coefficient, and γ_{jk} denotes the collision rate. At a temperature of 10 K, the critical densities for DCO⁺, DCN, and DNC in their $J=1-0$ transitions are 3.2×10^4 , 2.6×10^5 , and 8.2×10^4 cm⁻³, respectively, as reported by Feng et al. (2020). DCO⁺ and DCN have comparable A_{jk} values, but the collisional cross section for collisions with H₂ of the ionic molecule DCO⁺ is larger than those of neutral species. As a result, DCO⁺ has a critical density of about 10 times lower than that of DCN. Furthermore, Sarrasin et al. (2010) made a molecular emission model and found that the HNC rate coefficients appear to be larger than the HCN rate coefficients. This also works for DNC and DCN, which makes the critical density of DCN higher than that of DNC. This difference in critical densities would explain these two situations in our OTF observations: (1) The distribution of the DCO⁺ $J=1-0$ emission is more extended than that of the DCN emission at the same rms level, which is suitable for mapping BGPS2931, BGPS2940, BGPS2945, BGPS2984, BGPS2984, BGPS3018, BGPS3125, and BGPS3134. (2) There are detections of DCO⁺ and DNC $J=1-0$, but no detection of DCN, as occurs in BGPS2693 and BGPS4402. For the remaining massive starless clump candidate, BGPS3110, there is no DCO⁺ $J=1-0$ emission detected and the DNC $J=1-0$ emissions are found at the edge of the H44 α emissions. The DCO⁺ $J=1-0$ emission could be dissipated by the nearby HII region.

The reactions of these deuterated molecules could be another possibility to explain the differences between DCO⁺ and DCN. Two main pathways lead to the formation of DCO⁺ and DCN: at a temperature below ~ 30 K, the primary pathway is via H₃⁺ isotopologues; at a temperature of $\sim 30-80$ K, the dominant pathway is via light hydrocarbons (CH₂D⁺ and C₂HD⁺) (Albertsson et al. 2013). DCO⁺ is considered to be formed mainly from the former pathway and would therefore be expected to be abundant below ~ 30 K and be sensitive to freeze-out. DCN is primarily produced from the latter pathway. Therefore, for our sample with a kinetic temperature below 30 K, DCO⁺ is expected to be formed more efficiently than DCN, which then leads to a stronger intensity of DCO⁺ than that of DCN, which is consistent with the results of our OTF observation. For regions with a temperature higher than 30 K, DCN would be formed increasingly and has an intensity higher than the intensity of DCO⁺, which is suitable for the DCN peaks in BPGS2945 and the north-eastern DCN peak in BGPS2984.

Furthermore, the DCN $J=1-0$ line exhibits a tripartite hyperfine structure, consisting of F=1-1, 2-1, and 0-1 transitions. Under the assumption of LTE, the intensity of the central F=2-1 line significantly accounts for approximately 55.6% of the total DCN $J=1-0$ intensity, which would affect the detection of DCN.

Although the chemistry of HCN and HNC is not clear, the [HCN]/[HNC] ratio has been proposed as a potential tool to probe the temperature in massive star-forming regions (e.g., Graninger et al. 2014; Hacar et al. 2020), and the ratio decreases with increasing temperature. Observations found the [HCN]/[HNC] ratio ≤ 1 in starless cores (Tennekes et al. 2006; Hily-Blant et al. 2010) and infrared dark clouds (Liu et al. 2013). The [HCN]/[HNC] ratios of our sources may also have values lower than 1 based on our estimated $N(\text{HN}^{13}\text{C})/N(\text{H}^{13}\text{CN})$ ratios. Considering the estimated $D_{\text{frac}}(\text{HCN})$ values are found to be similar to the $D_{\text{frac}}(\text{HNC})$ values in Section 3.5, it is anticipated that the DCN emissions will exhibit a lower intensity compared to the DNC emissions, leading to a higher DNC detection rate.

In single-point observation, we also find difference in detection rates between $J=1-0$ and $J=2-1$ rotational lines, with detection rates for DCO⁺ and DCN $J=2-1$ of 19.8% and 9.9%. Our deuterated line survey is performed towards the continuum peak positions from Svoboda et al. (2016), which may not be the peak positions of deuterated lines (see Section 3.2). In addition, the beam sizes of the deuterated 2-1 rotational lines ($\sim 17''$) are smaller than those of the 1-0 rotational lines ($\sim 34''$), which may lead to the sources with DCO⁺ and DCN $J=1-0$ lines detection but no $J=2-1$ lines detection.

4.2. Deuterated fraction in SCCs

Our estimated values of deuterated fractions are similar to the values towards low-mass starless cores (e.g., Tafalla et al. 2006; Miettinen et al. 2011) or massive clumps (e.g., Gerner et al. 2015; Feng et al. 2019) in infrared dark clouds, indicating that our sources are at an early evolutionary phase. Sakai et al. (2012) found DNC/HNC ratio decreases when the star-forming region evolves, and our $D_{\text{frac}}(\text{HNC})$ have a comparable average value (0.020) with that of their MSX and *Spitzer*-dark sources (0.016), which also reveals that our sources are at similar evolutionary stages to theirs. In addition, the detection rate of DCN in Gerner et al. (2015) is much lower than those of DNC and DCO^+ , but the maximum value of $D_{\text{frac}}(\text{HCN})$ is similar to those of $D_{\text{frac}}(\text{HCO}^+)$ and $D_{\text{frac}}(\text{HNC})$. A similar situation can be found in our OTF mapping, which could be explained by different excitation conditions for deuterated molecular lines (see details in Section 4.1). Recently, there have been several studies of deuteration at high angular resolution towards protoplanetary disks (e.g., Huang et al. 2017; Salinas et al. 2017; Cataldi et al. 2021). Although the angular resolution ($\sim 0.3''\text{--}0.9''$) is much higher than ours, we have similar deuterated fraction values. In our study, we derive similar deuterated fractions for HCN, HCO^+ , and HNC, more studies on deuterated molecules are needed to prove that the deuterated fractions are chemical clocks.

5. SUMMARY

We first performed single-point observations towards 101 starless clump candidates using the IRAM 30-m telescope, aiming to search for deuterated molecular lines. And then, OTF observations are conducted targeting 11 selected sources. Our results are summarized below.

1. Our single-point observations unveil notable detections, including 46 DCO^+ $J=1-0$, 12 DCN $J=1-0$, 51 DNC $J=1-0$, 7 N_2D^+ $J=1-0$, 20 DCO^+ $J=2-1$, and 10 DCN $J=2-1$ detections. The SCCs with and without detections of deuterated molecules exhibit similar median values for 1.1 mm intensity, mass, and distance. However, SCCs with deuterated molecule detections display lower median kinetic temperatures and narrower median H_2CO ($1_{(0,1)}-0_{(0,0)}$) FWHM values compared to those without such detections.

2. In the OTF observation, nine out of 11 sources are detected with peaks of deuterated molecules near the 1.1mm continuum peak positions. Within the regions containing deuterated molecule peaks, the intensities of DCO^+ $J=1-0$ are stronger than those of DCN and DNC $J=1-0$. Additionally, we find clear velocity gradients in three sources. Moreover, most of the emissions of deuterated molecules and ^{13}C -isotopologues also exhibit peak positions close to those of the 1.1mm continuum peaks. DCN and H^{13}CN $J=1-0$ display similar peak intensities in the peak regions, while DCO^+ and DNC $J=1-0$ have higher peak intensities than H^{13}CO^+ and HN^{13}C $J=1-0$.

3. From the OTF observations, we estimate the column density of the deuterated species and ^{13}C -isotopologues for the 11 selected sources within the deuterated peak regions. The estimated column density ranges are $9.8 \times 10^{11} - 3.0 \times 10^{12} \text{ cm}^{-2}$ for DCN, $1.2 \times 10^{12} - 7.6 \times 10^{12} \text{ cm}^{-2}$ for DCO^+ , and $5.5 \times 10^{11} - 3.6 \times 10^{12} \text{ cm}^{-2}$ for DNC. We derive similar deuterated abundances of 0.004–0.045, 0.011–0.040, and 0.004–0.038 for $D_{\text{frac}}(\text{HCN})$, $D_{\text{frac}}(\text{HCO}^+)$, and $D_{\text{frac}}(\text{HNC})$, respectively, despite the different detection rates for DCN, DCO^+ , and DNC $J=1-0$.

4. The detection differences among deuterated species of dense gas tracers are likely attributed to their different critical densities and formation pathways.

We thank the anonymous referees for their comments and suggestions, which have improved this work. This work is supported by National Key R&D Program of China No. 2022YFA1603100, No. 2017YFA0402604, and the National Natural Science Foundation of China (NSFC) grants U1731237 and 11590781. K.Q. acknowledges the science research grant from the China Manned Space Project. K.Y. acknowledges the supports from China Postdoctoral Science Foundation No. 2021M701669. This work is based on observations carried out under project number 131-18 with the IRAM 30m telescope. IRAM is supported by INSU/CNRS (France), MPG (Germany) and IGN (Spain).

REFERENCES

- | | |
|---|---|
| Albertsson, T., Semenov, D. A., Vasyunin, A. I., et al. 2013, <i>ApJS</i> , 207, 27. doi:10.1088/0067-0049/207/2/27 | Bergman, P., Parise, B., Liseau, R., et al. 2011, <i>A&A</i> , 527, A39. doi:10.1051/0004-6361/201015012 |
| Belloche, A., Parise, B., van der Tak, F. F. S., et al. 2006, <i>A&A</i> , 454, L51. doi:10.1051/0004-6361:20065306 | Bizzocchi, L., Caselli, P., Spezzano, S., et al. 2014, <i>A&A</i> , 569, A27. doi:10.1051/0004-6361/201423858 |

- Bolatto, A. D., Warren, S. R., Leroy, A. K., et al. 2013, *Nature*, 499, 450. doi:10.1038/nature12351
- Busquet, G., Palau, A., Estalella, R., et al. 2010, *A&A*, 517, L6. doi:10.1051/0004-6361/201014866
- Calahan, J. K., Shirley, Y. L., Svoboda, B. E., et al. 2018, *ApJ*, 862, 63. doi:10.3847/1538-4357/aabfea
- Caselli, P., van der Tak, F. F. S., Ceccarelli, C., et al. 2003, *A&A*, 403, L37. doi:10.1051/0004-6361:20030526
- Caselli, P., Walmsley, C. M., Tafalla, M., et al. 1999, *ApJL*, 523, L165. doi:10.1086/312280
- Caselli, P., Walmsley, C. M., Zucconi, A., et al. 2002, *ApJ*, 565, 331. doi:10.1086/324301
- Cataldi, G., Yamato, Y., Aikawa, Y., et al. 2021, *ApJS*, 257, 10. doi:10.3847/1538-4365/ac143d
- Crapsi, A., Caselli, P., Walmsley, C. M., et al. 2005, *ApJ*, 619, 379. doi:10.1086/426472
- Crapsi, A., Caselli, P., Walmsley, M. C., et al. 2007, *A&A*, 470, 221. doi:10.1051/0004-6361:20077613
- Endres, C. P., Schlemmer, S., Schilke, P., et al. 2016, *Journal of Molecular Spectroscopy*, 327, 95. doi:10.1016/j.jms.2016.03.005
- Feng, S., Caselli, P., Wang, K., et al. 2019, *ApJ*, 883, 202. doi:10.3847/1538-4357/ab3a42
- Feng, S., Li, D., Caselli, P., et al. 2020, *ApJ*, 901, 145. doi:10.3847/1538-4357/abada3
- Fontani, F., Busquet, G., Palau, A., et al. 2015, *A&A*, 575, A87. doi:10.1051/0004-6361/201424753
- Fontani, F., Caselli, P., Crapsi, A., et al. 2006, *A&A*, 460, 709. doi:10.1051/0004-6361:20066105
- Fontani, F., Sakai, T., Furuya, K., et al. 2014, *MNRAS*, 440, 448. doi:10.1093/mnras/stu298
- Fontani, F., Zhang, Q., Caselli, P., et al. 2009, *A&A*, 499, 233. doi:10.1051/0004-6361/200911617
- Fontani, F., Palau, A., Caselli, P., et al. 2011, *A&A*, 529, L7. doi:10.1051/0004-6361/201116631
- Friesen, R. K., Di Francesco, J., Myers, P. C., et al. 2010, *ApJ*, 718, 666. doi:10.1088/0004-637X/718/2/666
- Fuente, A., Rizzo, J. R., Caselli, P., et al. 2005, *A&A*, 433, 535. doi:10.1051/0004-6361:20041914
- Galloway-Sprietsma, M., Shirley, Y. L., Di Francesco, J., et al. 2022, *MNRAS*, 515, 5219. doi:10.1093/mnras/stac2084
- Gerner, T., Beuther, H., Semenov, D., et al. 2014, *A&A*, 563, A97. doi:10.1051/0004-6361/201322541
- Gerner, T., Shirley, Y. L., Beuther, H., et al. 2015, *A&A*, 579, A80. doi:10.1051/0004-6361/201423989
- Giannetti, A., Bovino, S., Caselli, P., et al. 2019, *A&A*, 621, L7. doi:10.1051/0004-6361/201834602
- Giers, K., Spezzano, S., Caselli, P., et al. 2023, *A&A*, 676, A78. doi:10.1051/0004-6361/202346433
- Graninger, D. M., Herbst, E., Öberg, K. I., et al. 2014, *ApJ*, 787, 74. doi:10.1088/0004-637X/787/1/74
- Hacar, A., Bosman, A. D., & van Dishoeck, E. F. 2020, *A&A*, 635, A4. doi:10.1051/0004-6361/201936516
- Henkel, C., Walmsley, C. M., & Wilson, T. L. 1980, *A&A*, 82, 41
- Hily-Blant, P., Walmsley, M., Pineau Des Forêts, G., et al. 2010, *A&A*, 513, A41. doi:10.1051/0004-6361/200913200
- Hirota, T., Ikeda, M., & Yamamoto, S. 2003, *ApJ*, 594, 859. doi:10.1086/376970
- Huang, J., Öberg, K. I., Qi, C., et al. 2017, *ApJ*, 835, 231. doi:10.3847/1538-4357/835/2/231
- Leurini, S., Rolfs, R., Thorwirth, S., et al. 2006, *A&A*, 454, L47. doi:10.1051/0004-6361:20065555
- Li, S., Sanhueza, P., Lu, X., et al. 2022, *ApJ*, 939, 102. doi:10.3847/1538-4357/ac94d4
- Li, S., Sanhueza, P., Zhang, Q., et al. 2023, *ApJ*, 949, 109. doi:10.3847/1538-4357/acc58f
- Li, Y., Wang, J., Li, J., et al. 2022, *MNRAS*, 512, 4934. doi:10.1093/mnras/stab3186
- Liu, X.-L., Wang, J.-J., & Xu, J.-L. 2013, *MNRAS*, 431, 27. doi:10.1093/mnras/stt063
- Mangum, J. G. & Shirley, Y. L. 2015, *PASP*, 127, 266. doi:10.1086/680323
- McKee, C. F. & Tan, J. C. 2003, *ApJ*, 585, 850. doi:10.1086/346149
- Miettinen, O., Hennemann, M., & Linz, H. 2011, *A&A*, 534, A134. doi:10.1051/0004-6361/201117187
- Milam, S. N., Savage, C., Brewster, M. A., et al. 2005, *ApJ*, 634, 1126. doi:10.1086/497123
- Millar, T. J., Bennett, A., & Herbst, E. 1989, *ApJ*, 340, 906. doi:10.1086/167444
- Morii, K., Sanhueza, P., Nakamura, F., et al. 2023, *ApJ*, 950, 148. doi:10.3847/1538-4357/accea
- Motte, F., Bontemps, S., & Louvet, F. 2018, *ARA&A*, 56, 41. doi:10.1146/annurev-astro-091916-055235
- Müller, H. S. P., Schlöder, F., Stutzki, J., et al. 2005, *Journal of Molecular Structure*, 742, 215. doi:10.1016/j.molstruc.2005.01.027
- Müller, H. S. P., Thorwirth, S., Roth, D. A., et al. 2001, *A&A*, 370, L49. doi:10.1051/0004-6361:20010367
- Öberg, K. I., Qi, C., Wilner, D. J., et al. 2012, *ApJ*, 749, 162. doi:10.1088/0004-637X/749/2/162
- Padoan, P., Pan, L., Juvela, M., et al. 2020, *ApJ*, 900, 82. doi:10.3847/1538-4357/abaa47
- Pickett, H. M., Poynter, R. L., Cohen, E. A., et al. 1998, *JQSRT*, 60, 883. doi:10.1016/S0022-4073(98)00091-0
- Pillai, T., Caselli, P., Kauffmann, J., et al. 2012, *ApJ*, 751, 135. doi:10.1088/0004-637X/751/2/135

- Pillai, T., Kauffmann, J., Wyrowski, F., et al. 2011, *A&A*, 530, A118. doi:10.1051/0004-6361/201015899
- Pillai, T., Wyrowski, F., Hatchell, J., et al. 2007, *A&A*, 467, 207. doi:10.1051/0004-6361:20065682
- Redaelli, E., Bovino, S., Sanhueza, P., et al. 2022, *ApJ*, 936, 169. doi:10.3847/1538-4357/ac85b4
- Reid, M. J., Menten, K. M., Brunthaler, A., et al. 2019, *ApJ*, 885, 131. doi:10.3847/1538-4357/ab4a11
- Ren, Z., Wu, Y., Zhu, M., et al. 2012, *MNRAS*, 422, 1098. doi:10.1111/j.1365-2966.2012.20683.x
- Roberts, H., Fuller, G. A., Millar, T. J., et al. 2002, *A&A*, 381, 1026. doi:10.1051/0004-6361:20011596
- Roberts, H. & Millar, T. J. 2000, *A&A*, 361, 388
- Roueff, E., Gerin, M., Lis, D. C., et al. 2013, *Journal of Physical Chemistry A*, 117, 9959. doi:10.1021/jp400119a
- Roueff, E., Parise, B., & Herbst, E. 2007, *A&A*, 464, 245. doi:10.1051/0004-6361:20066531
- Sakai, T., Sakai, N., Furuya, K., et al. 2012, *ApJ*, 747, 140. doi:10.1088/0004-637X/747/2/140
- Sakai, T., Sakai, N., Furuya, K., et al. 2015, *ApJ*, 803, 70. doi:10.1088/0004-637X/803/2/70
- Sakai, T., Sanhueza, P., Furuya, K., et al. 2022, *ApJ*, 925, 144. doi:10.3847/1538-4357/ac3d2e
- Salinas, V. N., Hogerheijde, M. R., Mathews, G. S., et al. 2017, *A&A*, 606, A125. doi:10.1051/0004-6361/201731223
- Sanhueza, P., Contreras, Y., Wu, B., et al. 2019, *ApJ*, 886, 102. doi:10.3847/1538-4357/ab45e9
- Sarrasin, E., Abdallah, D. B., Wernli, M., et al. 2010, *MNRAS*, 404, 518. doi:10.1111/j.1365-2966.2010.16312.x
- Schilke, P. 2015, *EAS Publications Series*, 75-76, 227. doi:10.1051/eas/1575046
- Schilke, P., Walmsley, C. M., Pineau Des Forets, G., et al. 1992, *A&A*, 256, 595
- Schöier, F. L., van der Tak, F. F. S., van Dishoeck, E. F., et al. 2005, *A&A*, 432, 369. doi:10.1051/0004-6361:20041729
- Shirley, Y. L. 2015, *PASP*, 127, 299. doi:10.1086/680342
- Smith, R. J., Longmore, S., & Bonnell, I. 2009, *MNRAS*, 400, 1775. doi:10.1111/j.1365-2966.2009.15621.x
- Svoboda, B. E., Shirley, Y. L., Battersby, C., et al. 2016, *ApJ*, 822, 59. doi:10.3847/0004-637X/822/2/59
- Tafalla, M., Santiago-García, J., Myers, P. C., et al. 2006, *A&A*, 455, 577. doi:10.1051/0004-6361:20065311
- Tennekes, P. P., Harju, J., Juvela, M., et al. 2006, *A&A*, 456, 1037. doi:10.1051/0004-6361:20040294
- Tiné, S., Roueff, E., Falgarone, E., et al. 2000, *A&A*, 356, 1039
- Treviño-Morales, S. P., Pilleri, P., Fuente, A., et al. 2014, *A&A*, 569, A19. doi:10.1051/0004-6361/201423407
- Turner, B. E. 2001, *ApJS*, 136, 579. doi:10.1086/322536
- van Gelder, M. L., Jaspers, J., Nazari, P., et al. 2022, *A&A*, 667, A136. doi:10.1051/0004-6361/202244471
- Vastel, C., Ceccarelli, C., Lefloch, B., et al. 2016, *A&A*, 591, L2. doi:10.1051/0004-6361/201628427
- Whiteoak, J. B. & Gardner, F. F. 1979, *MNRAS*, 188, 445. doi:10.1093/mnras/188.3.445
- Wienen, M., Wyrowski, F., Walmsley, C. M., et al. 2021, *A&A*, 649, A21. doi:10.1051/0004-6361/201731208
- Willacy, K. 2007, *ApJ*, 660, 441. doi:10.1086/512796
- Wilson, T. L., Bieging, J., Downes, D., et al. 1976, *A&A*, 51, 303
- Wilson, T. L. & Rood, R. 1994, *ARA&A*, 32, 191. doi:10.1146/annurev.aa.32.090194.001203
- Yan, Y. T., Henkel, C., Kobayashi, C., et al. 2023, *A&A*, 670, A98. doi:10.1051/0004-6361/202244584
- Zahorecz, S., Jimenez-Serra, I., Testi, L., et al. 2021, *A&A*, 653, A45. doi:10.1051/0004-6361/201937012

Table 1. Physical parameters of the MSSCs and detection of the deuterated lines.

Source	R.A.	Decl.	$S_{1.1\text{mm}}$	Mass	Distance	NH_3		Detection						
	(J2000)	(J2000)				ν_{LSR}	T_{Kin}	$J=1-0$			$J=2-1$			
	(hh:mm:ss)	(dd:mm:ss)						DCO^+	DCN	DNC	N_2D^+	DCO^+	DCN	
	(1)	(2)				(3)	(4)	(5)	(6)	(7)	(8)	(9)	(10)	(11)
BGPS2427	18:09:33.88	-20:47:00.76	1.458	360.3	4.670	30.656	12.556							
BGPS2430	18:08:49.41	-20:40:23.82	2.700	336.7	5.013	21.269	12.264							
BGPS2432	18:09:44.59	-20:47:10.21	1.042	239.6	4.369	31.075	11.957							
BGPS2437	18:10:19.41	-20:50:27.45	2.465	1081	4.437	1.868	17.324							
BGPS2533	18:10:30.29	-20:14:44.20	0.755	212.2	4.975	31.835	12.267				✓			
BGPS2564	18:10:06.08	-18:46:05.64	0.227	43.03	3.013	29.572	11.758	✓		✓			✓	
BGPS2693	18:11:13.56	-17:44:54.85	0.387	20.71	2.103	19.134	12.440	✓		✓			✓	
BGPS2710	18:13:49.04	-17:59:33.25	2.948	573.8	1.200	34.594	13.976	✓		✓			✓	
BGPS2724	18:14:13.61	-17:59:52.02	1.010	112.5	1.185	36.251	19.897							
BGPS2732	18:14:26.85	-17:58:50.93	0.318	18.97	1.191	37.474	26.836							
BGPS2742	18:14:29.10	-17:57:21.83	0.510	53.37	1.183	36.011	21.974							
BGPS2762	18:11:39.52	-17:32:09.40	1.376	51.88	3.304	17.849	21.549	✓		✓			✓	
BGPS2931	18:17:27.51	-17:06:08.42	0.539	16.25	3.285	22.771	11.711	✓	✓	✓			✓	✓
BGPS2940	18:17:17.15	-17:01:07.47	3.492	69.98	3.366	20.035	17.795	✓	✓	✓		✓	✓	✓
BGPS2945	18:17:27.35	-17:00:23.66	1.316	47.59	1.178	22.683	11.666	✓	✓	✓	✓		✓	✓
BGPS2949	18:17:33.74	-16:59:34.94	0.901	27.35	1.279	22.520	11.548	✓		✓			✓	
BGPS2970	18:17:05.08	-16:43:28.66	2.076	483.6	3.568	40.010	13.606	✓		✓			✓	
BGPS2971	18:16:48.12	-16:41:08.91	1.054	217.7	1.815	36.545	15.689							
BGPS2976	18:17:07.84	-16:41:14.59	0.493	98.07	1.830	39.630	13.792	✓		✓			✓	
BGPS2984	18:18:18.23	-16:44:52.26	0.787	36.16	1.855	18.422	11.486	✓	✓	✓			✓	
BGPS2986	18:18:29.68	-16:44:50.69	1.092	37.08	2.014	19.966	11.634	✓	✓	✓	✓		✓	✓
BGPS3018	18:19:13.88	-16:35:16.47	1.671	12.60	6.522	18.958	13.472	✓	✓	✓	✓		✓	
BGPS3030	18:19:19.68	-16:31:39.82	1.929	97.79	1.784	19.006	17.197	✓	✓	✓	✓		✓	✓
BGPS3110	18:20:16.27	-16:08:51.13	9.667	107.2	2.005	17.687	25.166		✓	✓				✓
BGPS3114	18:20:31.50	-16:08:37.80	64.756	4820	1.848	23.525								
BGPS3117	18:20:06.68	-16:04:45.75	3.166	84.77	2.001	18.574	33.383							
BGPS3118	18:20:16.17	-16:05:50.72	8.842	171.3	2.001	17.210	23.681			✓				✓
BGPS3125	18:20:06.11	-16:01:58.02	2.180	95.55	3.466	21.531	21.251	✓	✓	✓			✓	✓
BGPS3128	18:20:35.27	-16:04:53.81	3.765	135.1	4.170	19.751	23.170							
BGPS3129	18:20:12.99	-16:00:24.13	0.463	23.49	4.289	19.716	17.865			✓				
BGPS3134	18:19:52.72	-15:56:01.56	3.168	217.9	4.083	20.465	15.919	✓	✓	✓	✓		✓	✓
BGPS3139	18:20:34.24	-15:58:14.00	3.046	184.9	5.408	21.798	17.232		✓	✓				✓
BGPS3151	18:20:23.19	-15:39:31.96	2.323	631.7	3.379	39.401	12.337	✓		✓				
BGPS3220	18:24:57.03	-13:20:32.39	1.927	298.1	3.874	46.130	18.524							
BGPS3243	18:25:32.74	-13:01:31.05	0.554	274.8	4.597	68.468	11.712	✓					✓	
BGPS3247	18:25:14.45	-12:54:16.74	0.796	185.2	4.447	45.168	13.037	✓		✓			✓	
BGPS3276	18:26:24.92	-12:49:30.07	1.054	266.9	3.379	19.647	17.192							
BGPS3300	18:26:28.42	-12:37:03.98	0.601	174.7	11.668	64.147	15.401			✓				
BGPS3302	18:27:15.23	-12:42:56.45	5.207	1251	11.785	66.372	18.642	✓		✓			✓	
BGPS3306	18:23:34.02	-12:13:52.79	0.202	64.24	4.777	57.108	12.078	✓		✓				
BGPS3312	18:25:44.52	-12:28:34.11	0.232	32.50	5.271	47.302	17.876							
BGPS3315	18:25:33.24	-12:26:50.63	8.630	1194	4.793	44.313	19.335							
BGPS3344	18:26:40.00	-12:25:15.81	5.458	1631	4.314	65.694	16.138			✓				
BGPS3442	18:28:13.51	-11:40:44.94	0.835	244.4	3.442	65.752	12.545							
BGPS3444	18:28:27.26	-11:41:33.99	0.291	113.9	3.297	69.686	13.059							
BGPS3475	18:28:28.28	-11:06:44.16	0.718	1367	3.426	75.858	17.594							
BGPS3484	18:29:15.74	-10:58:28.73	0.549	958.7	3.484	56.352	18.470							
BGPS3487	18:29:22.77	-10:58:01.69	1.009	1017	3.490	54.597	29.321							
BGPS3534	18:30:33.45	-10:24:19.00	0.242	48.64	3.225	65.057	22.391							
BGPS3604	18:30:43.92	-09:34:42.15	0.780	228.6	11.010	51.515	11.828	✓		✓				
BGPS3606	18:29:41.95	-09:24:49.10	0.286	83.93	4.214	49.555	10.312	✓						
BGPS3608	18:31:54.82	-09:39:05.03	0.396	125.5	4.081	63.774	13.703							
BGPS3627	18:31:42.32	-09:24:29.17	1.702	827.0	4.169	81.302	12.486							
BGPS3656	18:32:49.54	-09:21:29.26	0.383	185.1	3.906	77.254	12.005							
BGPS3686	18:34:14.58	-09:18:35.84	2.332	830.5	2.939	77.284	14.695	✓						
BGPS3705	18:34:32.69	-09:14:09.40	1.302	408.5	3.116	61.578	12.945	✓						
BGPS3710	18:34:20.55	-09:10:01.94	1.033	355.4	2.505	74.682	14.465							
BGPS3716	18:34:24.15	-09:08:03.60	1.492	396.4	3.146	75.869	16.811							
BGPS3736	18:33:28.22	-08:55:04.36	0.296	122.3	5.031	65.388	13.057			✓				

Table 1 continued on next page

Table 1 (*continued*)

Source	R.A.	Decl.	$S_{1.1\text{mm}}$	Mass	Distance	NH ₃		Detection								
	(J2000)	(J2000)				ν_{LSR}	T_{Kin}	$J=1-0$			$J=2-1$					
	(hh:mm:ss)	(dd:mm:ss)						(Jy)	(M_{\odot})	(kpc)	(km s^{-1})	(K)	DCO ⁺	DCN	DNC	N ₂ D ⁺
	(1)	(2)				(3)	(4)	(5)	(6)	(7)	(8)	(9)	(10)	(11)	(12)	(13)
BGPS3822	18:33:32.06	-08:32:26.27	1.205	417.4	3.370	54.549	11.728	✓		✓						
BGPS3833	18:33:36.50	-08:30:50.70	0.576	166.4	4.493	55.589	11.965			✓						
BGPS3892	18:35:59.74	-08:38:56.48	1.738	751.2	5.300	64.464	11.286			✓						
BGPS3922	18:33:40.98	-08:14:55.30	0.431	218.2	9.876	89.219	12.324									
BGPS3924	18:34:51.17	-08:23:40.02	0.174	102.1	5.782	81.292	11.797				✓					
BGPS3982	18:34:30.79	-08:02:07.36	0.668	176.2	11.582	53.937	12.997				✓					
BGPS4029	18:35:54.40	-07:59:44.60	1.344	707.4	3.539	81.519	11.874	✓		✓						
BGPS4082	18:35:10.07	-07:39:43.55	0.582	355.6	5.084	99.517	13.707	✓		✓			✓			
BGPS4085	18:33:57.05	-07:29:31.43	0.613	1100	5.087	96.624	14.983									
BGPS4095	18:35:04.00	-07:36:06.46	1.502	1078	5.353	112.989	13.631									
BGPS4119	18:36:29.65	-07:42:06.09	0.771	1802	5.577	55.331	15.357	✓								
BGPS4135	18:37:44.06	-07:48:15.35	0.683	166.6	3.572	59.627	14.581	✓								
BGPS4140	18:36:49.66	-07:40:36.83	0.559	279.7	3.617	95.999	15.282				✓					
BGPS4145	18:36:52.95	-07:39:49.20	0.815	391.9	4.985	96.532	14.236									
BGPS4191	18:37:04.58	-07:33:12.26	0.738	421.1	5.123	97.507	13.219	✓			✓					
BGPS4230	18:35:50.85	-07:12:23.58	1.463	774.2	5.034	107.435	16.582				✓					
BGPS4294	18:38:51.58	-06:55:36.52	0.999	217.0	5.688	56.174	15.271				✓					
BGPS4297	18:38:56.37	-06:55:08.44	0.445	67.98	4.973	58.647	19.937									
BGPS4346	18:38:49.58	-06:31:27.06	0.308	56.42	5.823	92.586	27.280									
BGPS4347	18:38:42.93	-06:30:27.83	0.901	402.6	5.295	93.469	15.717	✓			✓					
BGPS4354	18:38:51.42	-06:29:15.38	0.761	421.5	5.840	93.974	12.947	✓			✓					
BGPS4356	18:37:29.48	-06:18:12.13	4.821	2676	4.453	109.935	15.780				✓					
BGPS4375	18:39:10.19	-06:21:15.90	0.287	170.4	3.793	93.072	11.790									
BGPS4396	18:38:34.74	-05:56:43.97	1.687	1537	4.266	112.729	12.362				✓					
BGPS4402	18:39:28.64	-05:57:58.57	0.576	330.5	4.285	99.214	13.125	✓			✓					
BGPS4422	18:38:47.88	-05:36:16.38	0.406	240.4	3.917	110.707	13.177				✓					
BGPS4472	18:41:17.32	-05:09:56.83	0.601	105.9	3.216	46.876	14.288	✓			✓					
BGPS4732	18:44:23.40	-04:02:01.21	6.010	3668	3.782	88.323	12.378	✓			✓					
BGPS4827	18:44:42.45	-03:44:21.63	3.758	1326	4.928	86.095	15.926	✓			✓					
BGPS4841	18:42:15.65	-03:22:26.19	1.050	603.0	4.266	83.981	12.030	✓			✓					
BGPS4902	18:46:11.36	-03:42:55.73	0.834	389.2	4.656	84.140	13.527	✓			✓					
BGPS4953	18:45:51.82	-03:26:24.16	0.489	293.8	5.502	90.783	12.690	✓			✓					
BGPS4962	18:45:59.61	-03:25:14.53	0.791	497.7	6.092	88.308	12.537	✓			✓					
BGPS4967	18:43:27.80	-03:05:14.94	0.515	252.0	3.681	80.309	12.161	✓			✓					
BGPS5021	18:44:37.07	-02:55:04.40	1.138	672.7	5.181	80.052	12.107	✓			✓		✓			
BGPS5064	18:45:48.44	-02:44:31.65	4.001	1940	5.210	100.721	15.803	✓			✓					
BGPS5089	18:48:49.88	-02:59:47.86	1.164	402.2	6.534	85.200	15.078	✓								
BGPS5090	18:46:35.81	-02:42:30.19	0.195	142.3	5.181	96.295	11.350									
BGPS5114	18:50:23.54	-03:01:31.58	2.841	651.4	3.681	65.815	14.120									
BGPS5166	18:47:54.26	-02:26:07.11	0.943	525.7	6.092	102.730	15.422									
BGPS5183	18:47:00.29	-02:16:38.63	0.401	429.7	6.534	113.776	12.273									
BGPS5243	18:47:54.70	-02:11:10.72	0.616	425.9	5.210	95.890	12.693	✓								

NOTE—Columns list the (1) source ID; (2)–(3) the coordinates of the SCC sample; (4)–(6) 1.1 mm intensity, mass and distance for each SCC obtained from Svoboda et al. (2016); (7)–(8) LSR velocity and kinetic temperature derived from NH₃ observations in Svoboda et al. (2016), we obtain the peak velocity of HCO⁺ $J=1-0$ in Calahan et al. (2018) for BGPS 3114 with no NH₃ detection; (9)–(14) detection of the deuterated lines.

Table 2. Observational parameters.

Molecules	ν (GHz)	E_u (K)	n_{crit} (cm^{-3})	ΔV (km s^{-1})	F_{eff}	B_{eff}	Observation
(1)	(2)	(3)	(4)	(5)	(6)	(7)	(8)
$\text{DCO}^+ J=1-0$	72.039312	3.5	3.2E+4	0.813	98%	79%	1,2
$\text{DCN } J=1-0$	72.414927	3.5	2.6E+5	0.807	98%	79%	1,2
$\text{H}_2\text{CO } 1_{(0,1)}-1_{(0,0)}$	72.837951	3.5	4.5E+4	0.804	98%	79%	1
$\text{DNC } 1-0$	76.305697	3.7	8.2E+4	0.766	98%	79%	1,2
$\text{N}_2\text{D}^+ J=1-0$	77.109632	3.7	5.9E+4	0.758	98%	79%	1,2
$\text{H}^{13}\text{CN } J=1-0$	86.340176	4.1	4.3E+5	0.678	98%	79%	2
$\text{H}^{13}\text{CO}^+ J=1-0$	86.754288	4.2	6.2E+4	0.674	98%	79%	2
$\text{HN}^{13}\text{C } 1-0$	87.090735	4.2	9.6E+4	0.672	98%	79%	2
$\text{HCN } J=1-0$	88.631847	4.3	4.7E+5	0.660	98%	79%	2
$\text{HCO}^+ 1-0$	89.188526	4.3	7.0E+4	0.656	98%	79%	2
$\text{HNC } 1-0$	90.663564	4.4	1.4E+5	0.645	98%	79%	2
$\text{N}_2\text{H}^+ J=1-0$	93.173777	4.5	6.1E+4	0.628	98%	79%	2
$\text{DCO}^+ J=2-1$	144.077285	10.4	5.3E+5	0.406	98%	78%	1,2
$\text{DCN } J=2-1$	144.828002	10.4	3.9E+6	0.404	98%	78%	1,2
$\text{DNC } 2-1$	152.609739	11.0	1.2E+6	0.383	98%	78%	2
$\text{N}_2\text{D}^+ J=2-1$	154.217084	11.1	5.2E+5	0.379	98%	78%	2

Note – Column 1: molecular lines; Column 2: the rest frequency obtained from the CDMS database (Müller et al. 2001, 2005; Endres et al. 2016); Column 3: the upper level energy; Column 4: critical densities at $T_K = 10$ K. For DCO^+ , DCN , DNC , and $\text{N}_2\text{D}^+ J=2-1$, values are calculated from the Einstein A - and C -coefficients from the LAMDA database (Schöier et al. 2005) and the CDMS database, and we assume that the deuterated lines have the same C -coefficients as their hydrogenated counterparts; for the rest molecular lines, values are obtained from Feng et al. (2020); Column 5: the velocity resolution corresponding to 0.195 MHz frequency resolution; Column 6: the forward efficiency; Column 7: the beam efficiency; Column 8: observational references: 1 (single-point observation), 2 (OTF mode observation).

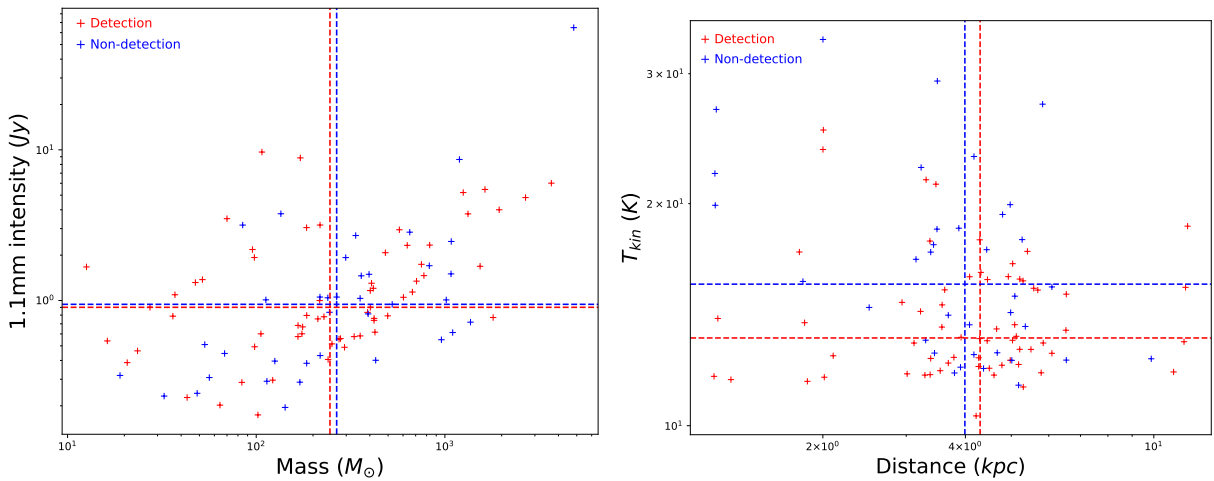


Figure 1. 1.1mm intensities versus masses (left panel) and kinetic temperatures obtained from NH_3 observations versus distances (right panel) for SCCs with and without deuterated molecule detections. The dashed lines represent the median values.

Table 4. Single-point observational parameters of DCO^+ , $\text{DCN } J=2-1$ and $\text{N}_2\text{D}^+ J=1-0$ detections.

Source	$\text{N}_2\text{D}^+ J=1-0$				$\text{DCO}^+ J=2-1$				$\text{DCN } J=2-1$			
	T_{mb} (K)	$\int T_{\text{mb}} dv$ (K km s $^{-1}$)	V_{LSR} (km s $^{-1}$)	FWHM (km s $^{-1}$)	T_{mb} (K)	$\int T_{\text{mb}} dv$ (K km s $^{-1}$)	V_{LSR} (km s $^{-1}$)	FWHM (km s $^{-1}$)	T_{mb} (K)	$\int T_{\text{mb}} dv$ (K km s $^{-1}$)	V_{LSR} (km s $^{-1}$)	FWHM (km s $^{-1}$)
BGPS2564					0.223	0.23±0.05	29.4±0.1	1.0±0.3				
BGPS2693					1.054	0.76±0.05	19.1±0.1	0.7±0.1				
BGPS2710					0.215	0.34±0.05	34.5±0.1	1.5±0.2				
BGPS2762					0.698	0.77±0.03	17.5±0.1	1.0±0.1				
BGPS2931					1.209	0.91±0.03	22.7±0.1	0.7±0.1	0.244	0.14±0.02	22.6±0.1	0.6±0.2
BGPS2940	0.151	0.31±0.07	20.0±0.2	2.0±0.3	1.816	2.64±0.05	19.9±0.1	1.4±0.1	0.281	0.51±0.06	19.9±0.1	1.7±0.2
BGPS2945	0.092	0.30±0.04	23.2±0.1	3.1±0.3	1.308	1.26±0.03	22.7±0.1	0.9±0.1	0.245	0.19±0.04	22.6±0.1	0.7±0.1
BGPS2949					0.376	0.39±0.03	22.5±0.1	1.0±0.1				
BGPS2970					0.108	0.21±0.03	40.0±0.1	1.9±0.2				
BGPS2976					0.320	0.45±0.04	39.7±0.1	1.3±0.1				
BGPS2984					1.006	0.70±0.03	18.4±0.1	0.6±0.1				
BGPS2986	0.323	0.68±0.12	20.3±0.2	2.0±0.4	1.397	1.76±0.03	20.1±0.1	1.2±0.1	0.238	0.25±0.05	19.9±0.1	1.0±0.2
BGPS3018	0.108	0.22±0.06	19.1±0.3	1.9±0.1	0.864	0.89±0.04	18.9±0.1	1.0±0.1				
BGPS3030					0.410	0.35±0.05	19.1±0.1	0.8±0.2	0.232	0.15±0.03	18.9±0.1	0.6±0.1
BGPS3110									0.248	0.39±0.08	17.7±0.1	1.5±0.2
BGPS3118									0.228	0.23±0.04	17.6±0.1	1.0±0.2
BGPS3125					0.548	0.42±0.04	21.5±0.1	0.7±0.1	0.506	0.42±0.04	21.2±0.1	0.8±0.1
BGPS3134	0.212	0.70±0.12	21.1±0.3	3.0±0.3	1.155	1.09±0.08	21.1±0.1	0.9±0.1	0.430	0.35±0.05	21.0±0.1	0.8±0.1
BGPS3139									0.390	0.28±0.05	19.8±0.1	0.7±0.1
BGPS3243					0.277	0.37±0.11	68.5±0.1	1.3±0.2				
BGPS3247					0.442	0.33±0.04	45.1±0.1	0.7±0.1				
BGPS3302					0.180	0.17±0.04	66.2±0.1	0.9±0.2				
BGPS3924	0.139	0.21±0.06	80.9±0.2	1.5±0.3								
BGPS4082					0.248	0.41±0.08	99.6±0.1	1.6±0.2				
BGPS5021	0.100	0.11±0.05	80.2±0.3	1.4±0.3								

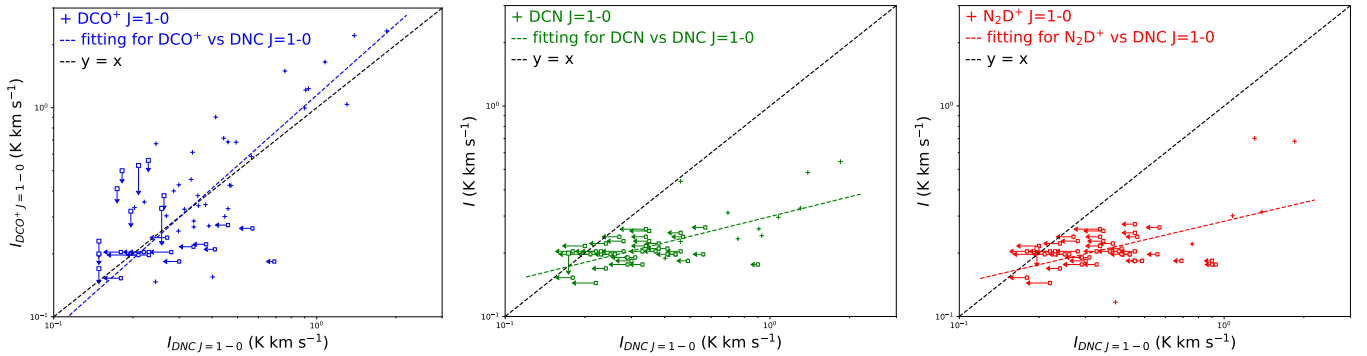
**Figure 2.** The integrated intensities of DCO^+ (left), DCN (middle), and N_2D^+ (right) $J=1-0$ in relation to $\text{DNC } J=1-0$. The colorful dashed lines represent the fitting results. The black dashed lines represent $y = x$.

Table 5. Single-point observational parameters of $\text{H}_2\text{CO}(1_{(0,1)}-0_{(0,0)})$ detections.

Source	$\text{H}_2\text{CO}(1_{(0,1)}-0_{(0,0)})$					Source	$\text{H}_2\text{CO}(1_{(0,1)}-0_{(0,0)})$				
	T_{mb} (K)	$\int T_{\text{mb}} dv$ (K km s $^{-1}$)	V_{LSR} (km s $^{-1}$)	FWHM (km s $^{-1}$)	D-isotopes detection		T_{mb} (K)	$\int T_{\text{mb}} dv$ (K km s $^{-1}$)	V_{LSR} (km s $^{-1}$)	FWHM (km s $^{-1}$)	D-isotopes detection
BGPS2564	0.499	0.42±0.08	29.4±0.1	0.8±0.1	Y	BGPS3656	0.320	0.27±0.05	77.2±0.1	0.8±0.2	
BGPS2693	0.964	1.03±0.06	19.1±0.1	1.0±0.1	Y	BGPS3686	0.390	1.22±0.11	77.2±0.1	2.9±0.3	Y
BGPS2710	0.575	1.26±0.07	34.6±0.1	2.2±0.2	Y	BGPS3710	0.435	1.89±0.14	74.5±0.2	4.1±0.4	Y
BGPS2724	0.826	3.02±0.11	35.9±0.1	3.5±0.1		BGPS3716	0.436	1.45±0.09	75.0±0.1	3.1±0.3	
BGPS2732	0.461	1.79±0.14	36.8±0.1	3.6±0.3			0.266	0.99±0.09	78.3±0.1	3.5±0.3	
	0.147	0.12±0.07	39.4±0.2	0.8±0.1		BGPS3736	0.438	0.93±0.07	65.5±0.1	2.0±0.2	Y
BGPS2742	0.421	1.81±0.09	35.9±0.1	4.1±0.3			0.146	0.31±0.07	68.2±0.2	2.0±0.5	
BGPS2762	1.366	2.96±0.08	18.1±0.1	2.0±0.1	Y	BGPS3822	0.568	1.25±0.12	54.5±0.1	2.1±0.2	Y
BGPS2931	0.716	1.43±0.07	22.9±0.1	1.9±0.2	Y	BGPS3833	0.239	0.47±0.13	56.3±0.3	1.9±0.3	Y
BGPS2940	3.308	11.4±0.10	20.0±0.1	3.2±0.1	Y	BGPS3892	0.253	0.47±0.10	63.3±0.3	1.7±0.2	Y
BGPS2945	0.382	1.20±0.10	19.5±0.1	2.9±0.3	Y		0.367	0.58±0.18	65.3±0.2	1.5±0.3	
	1.143	1.85±0.08	22.7±0.1	1.5±0.1		BGPS3922	0.310	0.35±0.07	89.4±0.1	1.1±0.2	
BGPS2949	0.581	2.39±0.17	20.8±0.1	3.9±0.3	Y	BGPS3982	0.339	0.88±0.12	54.0±0.2	2.5±0.3	Y
	0.899	0.76±0.10	22.7±0.1	0.8±0.1		BGPS4029	0.481	1.71±0.13	81.5±0.1	3.4±0.3	Y
BGPS2970	0.665	1.69±0.13	40.2±0.1	2.4±0.2		BGPS4082	0.610	1.59±0.14	99.5±0.1	2.4±0.3	Y
BGPS2971	0.340	1.16±0.18	36.8±0.2	3.2±0.4		BGPS4085	0.302	0.84±0.10	96.6±0.2	2.6±0.3	
	0.267	0.55±0.17	40.4±0.2	1.9±0.3		BGPS4095	0.128	0.27±0.17	109.5±0.4	1.9±0.3	
BGPS2976	0.532	1.16±0.09	39.6±0.1	2.1±0.2	Y		0.331	0.95±0.16	112.5±0.2	2.6±0.4	
BGPS2984	0.846	1.12±0.06	18.6±0.1	1.2±0.1	Y	BGPS4135	0.361	0.60±0.07	58.3±0.1	1.6±0.2	Y
BGPS2986	1.332	2.19±0.07	20.1±0.1	1.5±0.1	Y		0.159	0.26±0.07	61.7±0.3	1.6±0.2	
BGPS3018	0.930	1.52±0.07	19.0±0.1	1.5±0.1	Y	BGPS4140	0.499	0.90±0.08	95.8±0.1	1.7±0.2	Y
BGPS3030	0.769	1.21±0.11	19.1±0.1	1.5±0.1	Y	BGPS4145	0.278	0.81±0.12	96.4±0.2	2.8±0.3	
BGPS3110	2.552	9.54±0.10	17.2±0.1	3.5±0.1	Y	BGPS4191	0.563	1.47±0.10	97.2±0.1	2.4±0.2	Y
BGPS3114	0.405	1.62±0.10	22.6±0.1	3.8±0.2		BGPS4230	0.786	1.99±0.08	107.7±0.1	2.4±0.1	Y
BGPS3117	1.280	3.12±0.08	18.7±0.1	2.3±0.1		BGPS4294	0.417	1.58±0.11	56.3±0.1	3.6±0.3	Y
BGPS3118	1.941	5.13±0.15	16.8±0.1	2.5±0.1	Y	BGPS4297	0.560	1.88±0.11	58.2±0.1	3.2±0.2	
BGPS3125	0.275	0.60±0.11	18.5±0.2	2.1±0.3	Y	BGPS4346	0.567	2.81±0.16	92.5±0.1	4.7±0.2	
	0.793	1.65±0.11	21.4±0.1	2.0±0.1			0.139	0.66±0.14	97.0±0.3	4.5±0.4	
BGPS3128	1.190	3.78±0.11	18.4±0.1	3.0±0.1		BGPS4347	0.905	3.36±0.14	93.5±0.1	3.5±0.1	Y
BGPS3129	1.054	1.83±0.12	19.5±0.1	1.6±0.1	Y	BGPS4354	0.410	1.88±0.10	93.4±0.1	4.3±0.3	Y
BGPS3134	1.766	3.50±0.13	20.9±0.1	1.9±0.1	Y	BGPS4356	0.691	1.81±0.15	109.9±0.1	2.5±0.3	Y
BGPS3139	2.819	4.55±0.14	20.1±0.1	1.5±0.1	Y		0.361	0.90±0.15	113.0±0.2	2.3±0.3	
BGPS3151	0.659	1.71±0.16	39.6±0.1	2.4±0.2	Y	BGPS4375	0.446	0.89±0.09	93.1±0.1	1.9±0.2	
BGPS3220	0.654	3.33±0.18	46.4±0.1	4.8±0.3		BGPS4396	0.339	1.04±0.07	96.9±0.1	2.9±0.2	Y
	0.205	0.36±0.07	50.9±0.2	1.7±0.2			0.320	1.07±0.08	112.8±0.1	3.2±0.2	
BGPS3243	0.546	1.01±0.08	68.2±0.1	1.7±0.1	Y	BGPS4402	0.339	1.10±0.08	99.3±0.1	3.1±0.3	Y
BGPS3247	0.760	1.45±0.10	45.0±0.1	1.8±0.2	Y		0.178	0.31±0.07	102.5±0.2	1.7±0.2	
BGPS3276	0.598	1.70±0.10	66.9±0.1	2.7±0.2		BGPS4422	0.397	0.92±0.08	110.6±0.1	2.2±0.2	Y
BGPS3300	0.332	0.94±0.10	64.6±0.3	2.7±0.2	Y	BGPS4472	0.537	2.37±0.10	46.9±0.1	4.1±0.3	Y
	0.231	0.58±0.07	66.4±0.3	2.4±0.3		BGPS4732	0.460	0.98±0.05	88.4±0.1	2.0±0.1	Y
BGPS3302	0.656	3.20±0.10	66.8±0.1	4.6±0.2	Y	BGPS4827	0.753	1.67±0.09	86.3±0.1	2.1±0.1	Y
BGPS3306	0.463	0.73±0.06	57.0±0.1	1.5±0.1	Y	BGPS4841	0.467	1.13±0.08	83.5±0.1	2.3±0.2	Y
BGPS3312	0.397	0.55±0.07	47.0±0.1	1.3±0.2		BGPS4902	0.209	0.58±0.09	80.2±0.2	2.6±0.1	Y
BGPS3315	0.234	0.40±0.11	42.8±0.2	1.6±0.2			0.893	3.16±0.10	84.3±0.1	3.3±0.1	
	0.572	1.93±0.15	47.2±0.1	3.2±0.3		BGPS4953	0.435	1.16±0.08	90.8±0.1	2.5±0.2	Y
BGPS3344	0.284	0.78±0.12	65.6±0.2	2.6±0.3	Y	BGPS4962	0.319	0.82±0.09	88.6±0.1	2.4±0.2	Y
BGPS3442	0.219	0.50±0.08	65.7±0.2	2.1±0.3		BGPS4967	0.432	0.81±0.06	80.5±0.1	1.8±0.2	Y
BGPS3475	0.237	0.39±0.10	75.1±0.2	1.6±0.2		BGPS5021	0.464	1.74±0.09	80.0±0.1	3.5±0.2	Y
	0.241	0.73±0.12	77.6±0.3	2.9±0.3		BGPS5064	0.684	1.75±0.10	100.7±0.1	2.4±0.2	Y
BGPS3484	0.331	0.95±0.08	56.0±0.1	2.7±0.2		BGPS5089	0.585	1.33±0.05	85.3±0.1	2.1±0.1	Y
BGPS3487	0.203	0.33±0.12	53.3±0.3	1.5±0.3		BGPS5090	0.277	0.76±0.10	96.3±0.2	2.6±0.3	
	0.332	0.99±0.16	56.0±0.2	2.8±0.3		BGPS5114	0.467	1.37±0.13	65.9±0.2	2.8±0.2	
BGPS3604	0.723	1.64±0.09	51.5±0.1	2.1±0.1	Y	BGPS5166	0.649	1.27±0.10	102.7±0.1	1.8±0.2	
BGPS3606	0.193	0.28±0.08	49.5±0.2	1.4±0.2	Y	BGPS5183	0.214	0.50±0.10	113.9±0.2	2.2±0.3	
BGPS3608	0.245	0.90±0.13	64.4±0.2	3.5±0.3		BGPS5243	0.478	1.15±0.11	95.9±0.1	2.3±0.3	Y
BGPS3627	0.119	0.26±0.11	81.1±0.3	2.1±0.3							
	0.151	0.41±0.12	84.0±0.3	2.5±0.3							

Table 6. OTF observational parameters of DCO⁺, H¹³CO⁺, DNC, HN¹³C, DCN, and H¹³CN $J=1-0$ for the 11 sources.

Source	Molecular species	T _{mb} (K)	$\int T_{\text{mb}} dv$ (K km s ⁻¹)	V _{LSR} (km s ⁻¹)	FWHM (km s ⁻¹)	Centre	Source	Molecular species	T _{mb} (K)	$\int T_{\text{mb}} dv$ (K km s ⁻¹)	V _{LSR} (km s ⁻¹)	FWHM (km s ⁻¹)	Centre
BGPS2693	H ¹³ CO ⁺ $J=1-0$	0.532	0.43±0.06	19.1±0.1	0.8±0.2	[2'', 2'']	BGPS2693	H ¹³ CO ⁺ $J=1-0$	0.768	0.79±0.05	22.7±0.1	1.0±0.1	[10'', -35'']
	DCO ⁺ $J=1-0$	0.671	0.58±0.06	19.0±0.1	0.8±0.2			DCO ⁺ $J=1-0$	1.135	1.42±0.06	22.7±0.1	1.2±0.1	
BGPS2940	HN ¹³ C $J=1-0$	0.456	0.41±0.06	19.0±0.1	0.9±0.1	[0'', 3'']	BGPS2945	HN ¹³ C $J=1-0$	0.505	0.64±0.05	22.6±0.1	1.2±0.1	[17'', -33'']
	DNC $J=1-0$	0.685	0.65±0.07	19.0±0.1	0.9±0.1			DNC $J=1-0$	0.759	1.26±0.06	22.8±0.1	1.6±0.1	
	H ¹³ CO ⁺ $J=1-0$	0.821	2.00±0.08	19.9±0.1	2.3±0.1	[-10'', 2'']		H ¹³ CO ⁺ $J=1-0$	0.596	0.61±0.04	22.6±0.1	1.0±0.1	[-12'', 0'']
	DCO ⁺ $J=1-0$	0.985	1.92±0.05	20.0±0.1	1.8±0.1			DCO ⁺ $J=1-0$	0.847	0.86±0.03	22.6±0.1	1.0±0.1	
BGPS2984	H ¹³ CN $J=1-0$	0.387	1.47±0.22	20.2±0.2	3.6±0.3	[-9'', 6'']	BGPS2986	H ¹³ CN $J=1-0$	0.240	0.22±0.06	22.9±0.2	0.9±0.2	[-14'', -12'']
	DCN $J=1-0$	0.255	0.51±0.07	20.1±0.1	1.9±0.3			DCN $J=1-0$	0.290	0.32±0.06	22.7±0.1	1.0±0.1	
BGPS2984	HN ¹³ C $J=1-0$	0.457	1.02±0.08	19.7±0.1	2.1±0.2	[-11'', 4'']	BGPS2986	HN ¹³ C $J=1-0$	0.653	0.63±0.05	22.5±0.1	0.9±0.1	[-9'', -3'']
	DNC $J=1-0$	0.475	1.00±0.04	20.1±0.1	2.0±0.1			DNC $J=1-0$	0.739	1.05±0.04	22.7±0.1	1.3±0.1	
	H ¹³ CO ⁺ $J=1-0$	0.909	0.81±0.04	18.5±0.1	0.8±0.1	[-2'', 2'']		H ¹³ CO ⁺ $J=1-0$	0.994	1.33±0.06	19.9±0.1	1.3±0.1	[-7'', 1'']
	DCO ⁺ $J=1-0$	1.176	1.27±0.05	18.4±0.1	1.0±0.1			DCO ⁺ $J=1-0$	1.409	1.86±0.05	20.0±0.1	1.2±0.1	
BGPS3018	H ¹³ CN $J=1-0$	0.195	0.29±0.05	18.6±0.1	1.4±0.1	[-5'', 7'']	BGPS3110	H ¹³ CN $J=1-0$	0.262	0.40±0.08	20.1±0.1	1.5±0.2	[4'', 8'']
	DCN $J=1-0$	0.252	0.28±0.07	18.4±0.1	1.1±0.2			DCN $J=1-0$	0.314	0.41±0.06	20.1±0.1	1.2±0.2	
	HN ¹³ C $J=1-0$	0.570	0.58±0.06	18.1±0.1	1.0±0.1	[-5'', 9'']		HN ¹³ C $J=1-0$	0.742	1.01±0.06	19.7±0.1	1.3±0.1	[-5'', 6'']
	DNC $J=1-0$	0.752	0.92±0.04	18.4±0.1	1.2±0.1			DNC $J=1-0$	1.000	1.48±0.03	20.0±0.1	1.4±0.1	
BGPS3125	H ¹³ CO ⁺ $J=1-0$	0.464	0.67±0.08	19.1±0.1	1.4±0.1	[4'', 10'']	BGPS3134	H ¹³ CO ⁺ $J=1-0$	0.535	1.93±0.11	17.0±0.1	3.4±0.2	[-16'', 6'']
	DCO ⁺ $J=1-0$	0.651	0.86±0.06	19.1±0.1	1.3±0.1			DCO ⁺ $J=1-0$	0.431	0.83±0.05	20.9±0.1	1.8±0.1	
	H ¹³ CN $J=1-0$	0.156	0.34±0.07	19.6±0.2	2.1±0.3	[-28'', -34'']		H ¹³ CN $J=1-0$	0.629	2.07±0.16	17.4±0.1	3.1±0.2	[-7'', -2'']
	DCN $J=1-0$	0.237	0.20±0.06	19.1±0.1	0.8±0.1			DCN $J=1-0$	0.172	0.40±0.07	17.4±0.2	2.2±0.3	
BGPS3125	HN ¹³ C $J=1-0$	0.227	0.41±0.09	18.7±0.2	1.7±0.3	[-5'', -10'']	BGPS3134	HN ¹³ C $J=1-0$	0.590	1.63±0.13	16.8±0.1	2.6±0.2	[-11'', 5'']
	DNC $J=1-0$	0.271	0.54±0.05	19.0±0.1	1.9±0.2			DNC $J=1-0$	0.147	0.36±0.06	17.7±0.1	2.3±0.2	
	H ¹³ CO ⁺ $J=1-0$	0.901	0.64±0.05	21.5±0.1	0.7±0.2	[-9'', 3'']		H ¹³ CO ⁺ $J=1-0$	1.097	1.68±0.06	21.1±0.1	1.4±0.1	[-8'', 6'']
	DCO ⁺ $J=1-0$	0.120	0.31±0.08	21.8±0.2	2.4±0.4			DCO ⁺ $J=1-0$	0.431	0.83±0.05	20.9±0.1	1.8±0.1	
BGPS4402	H ¹³ CN $J=1-0$	0.174	0.19±0.06	21.8±0.1	1.0±0.3	[-10'', 24'']	BGPS3134	H ¹³ CN $J=1-0$	0.301	0.26±0.06	20.6±0.1	0.7±0.1	[0'', 13'']
	DCN $J=1-0$	0.085	0.20±0.04	21.6±0.3	2.2±0.3			DCN $J=1-0$	0.229	0.41±0.08	20.7±0.2	2.0±0.3	
	HN ¹³ C $J=1-0$	0.344	0.24±0.04	21.2±0.1	0.7±0.2	[-2'', 4'']		HN ¹³ C $J=1-0$	0.425	0.89±0.06	20.7±0.1	2.0±0.1	[-3'', 6'']
	DNC $J=1-0$	0.226	0.20±0.03	21.6±0.1	0.8±0.2			DNC $J=1-0$	0.585	1.12±0.05	20.7±0.1	1.8±0.1	
BGPS4402	H ¹³ CO ⁺ $J=1-0$	0.304	0.62±0.07	99.3±0.1	1.9±0.2	[-12'', -16'']	BGPS3134	H ¹³ CO ⁺ $J=1-0$	0.431	0.83±0.05	20.9±0.1	1.8±0.1	
	DCO ⁺ $J=1-0$	0.249	0.36±0.05	99.3±0.1	1.4±0.2			DCO ⁺ $J=1-0$	0.431	0.83±0.05	20.9±0.1	1.8±0.1	
	H ¹³ CN $J=1-0$	0.153	0.26±0.06	99.7±0.2	1.6±0.2	[-4'', 2'']		H ¹³ CN $J=1-0$	0.301	0.26±0.06	20.6±0.1	0.7±0.1	[0'', 13'']
	DCN $J=1-0$	0.129	0.21±0.02	99.2±0.2	1.5±0.2			DCN $J=1-0$	0.229	0.41±0.08	20.7±0.2	2.0±0.3	
BGPS4402	HN ¹³ C $J=1-0$	0.282	0.46±0.07	99.1±0.1	1.6±0.2	[10'', -18'']	BGPS3134	HN ¹³ C $J=1-0$	0.425	0.89±0.06	20.7±0.1	2.0±0.1	[-3'', 6'']
	DCN $J=1-0$	0.129	0.21±0.02	99.2±0.2	1.5±0.2			DCN $J=1-0$	0.585	1.12±0.05	20.7±0.1	1.8±0.1	

Table 7. Estimated column densities of optically thin molecular $J=1-0$ lines in the 11 sources from the OTF observations.

Source	T_{Kin} (K)	$N(\text{H}^{13}\text{CN})$ ($\times 10^{12} \text{ cm}^{-2}$)	$N(\text{DCN})$ ($\times 10^{12} \text{ cm}^{-2}$)	$N(\text{H}^{13}\text{CO}^+)$ ($\times 10^{12} \text{ cm}^{-2}$)	$N(\text{DCO}^+)$ ($\times 10^{12} \text{ cm}^{-2}$)	$N(\text{HN}^{13}\text{C})$ ($\times 10^{12} \text{ cm}^{-2}$)	$N(\text{DNC})$ ($\times 10^{12} \text{ cm}^{-2}$)
BGPS2693	12.440	1.4 ± 0.2	1.9 ± 0.2	1.1 ± 0.2	1.7 ± 0.2
BGPS2931	11.711	0.60 ± 0.15	1.1 ± 0.3	2.6 ± 0.2	4.9 ± 0.2	1.6 ± 0.1	3.1 ± 0.2
BGPS2940	17.795	6.5 ± 0.8	2.9 ± 0.4	7.5 ± 0.3	7.6 ± 0.2	3.3 ± 0.2	3.2 ± 0.1
BGPS2945	11.666	0.77 ± 0.18	1.5 ± 0.2	3.0 ± 0.2	4.9 ± 0.2	1.6 ± 0.1	2.6 ± 0.1
BGPS2984	11.486	1.0 ± 0.2	1.3 ± 0.3	2.6 ± 0.1	4.4 ± 0.2	1.5 ± 0.2	2.2 ± 0.1
BGPS2986	11.634	1.5 ± 0.2	1.9 ± 0.3	4.1 ± 0.2	6.2 ± 0.2	2.6 ± 0.2	3.6 ± 0.1
BGPS3018	13.472	1.3 ± 0.3	0.98 ± 0.21	2.1 ± 0.3	2.8 ± 0.2	1.1 ± 0.3	1.4 ± 0.1
BGPS3110	25.166	12 ± 0.9	3.0 ± 0.5	9.3 ± 0.6	...	6.6 ± 0.5	1.5 ± 0.3
BGPS3125	21.251	0.95 ± 0.22	1.3 ± 0.3	2.5 ± 0.2	1.3 ± 0.3	0.86 ± 0.13	0.71 ± 0.11
BGPS3134	15.919	1.1 ± 0.2	2.2 ± 0.4	5.9 ± 0.2	3.1 ± 0.2	2.6 ± 0.2	3.3 ± 0.1
BGPS4402	13.125	0.97 ± 0.13	...	1.9 ± 0.2	1.2 ± 0.2	1.2 ± 0.2	0.55 ± 0.06

Table 8. Estimated integrated intensity ratio, column density ratio and deuterated fraction from the OTF observations.

Source	Distance (kpc)	D_{gc} (kpc)	$^{12}\text{C}/^{13}\text{C}$	$\frac{I(\text{DCN})}{I(\text{H}^{13}\text{CN})}$	$\frac{N(\text{DCN})}{N(\text{H}^{13}\text{CN})}$	$\frac{I(\text{DCO}^+)}{I(\text{H}^{13}\text{CO}^+)}$	$\frac{N(\text{DCO}^+)}{N(\text{H}^{13}\text{CO}^+)}$	$\frac{I(\text{DNC})}{I(\text{HN}^{13}\text{C})}$	$\frac{N(\text{DNC})}{N(\text{HN}^{13}\text{C})}$	$D_{\text{frac}}(\text{HCN})$	$D_{\text{frac}}(\text{HCO}^+)$	$D_{\text{frac}}(\text{HNC})$
BGPS2693	2.103	6.115	56.684	1.33±0.09	1.39±0.09	1.58±0.11	1.54±0.10	...	0.025±0.002	0.027±0.002
BGPS2931	3.285	5.024	49.909	2.07±0.10	1.89±0.20	1.80±0.06	1.88±0.07	1.95±0.06	1.91±0.05	0.038±0.006	0.038±0.002	0.038±0.002
BGPS2940	3.366	4.950	49.450	0.34±0.03	0.45±0.04	0.96±0.05	1.02±0.05	0.98±0.05	0.98±0.05	0.009±0.001	0.021±0.001	0.020±0.001
BGPS2945	1.178	7.013	62.261	1.45±0.03	1.87±0.06	1.53±0.12	1.58±0.13	1.66±0.06	1.61±0.06	0.030±0.001	0.024±0.002	0.026±0.001
BGPS2984	1.855	6.369	58.261	0.97±0.08	1.24±0.12	1.57±0.12	1.65±0.14	1.58±0.04	1.54±0.04	0.021±0.001	0.029±0.002	0.026±0.001
BGPS2986	2.014	6.219	57.330	1.02±0.07	1.32±0.09	1.40±0.12	1.46±0.12	1.46±0.12	1.42±0.12	0.023±0.002	0.026±0.002	0.025±0.002
BGPS3018	6.522	2.462	33.999	0.60±0.07	0.76±0.09	1.28±0.10	1.34±0.10	1.33±0.11	1.28±0.11	0.022±0.002	0.040±0.003	0.038±0.002
BGPS3110	2.005	6.236	57.436	0.20±0.04	0.25±0.05	0.22±0.03	0.22±0.03	0.004±0.001	...	0.004±0.001
BGPS3125	3.466	4.889	49.071	1.05±0.10	1.38±0.11	0.48±0.05	0.53±0.05	0.95±0.08	0.83±0.07	0.028±0.002	0.011±0.001	0.017±0.001
BGPS3134	4.083	4.344	45.686	2.28±0.10	2.05±0.11	0.49±0.03	0.52±0.04	1.26±0.11	1.25±0.11	0.045±0.005	0.011±0.001	0.027±0.002
BGPS4402	4.285	4.706	47.934	0.59±0.06	0.61±0.07	0.45±0.07	0.44±0.06	...	0.014±0.002	0.009±0.001

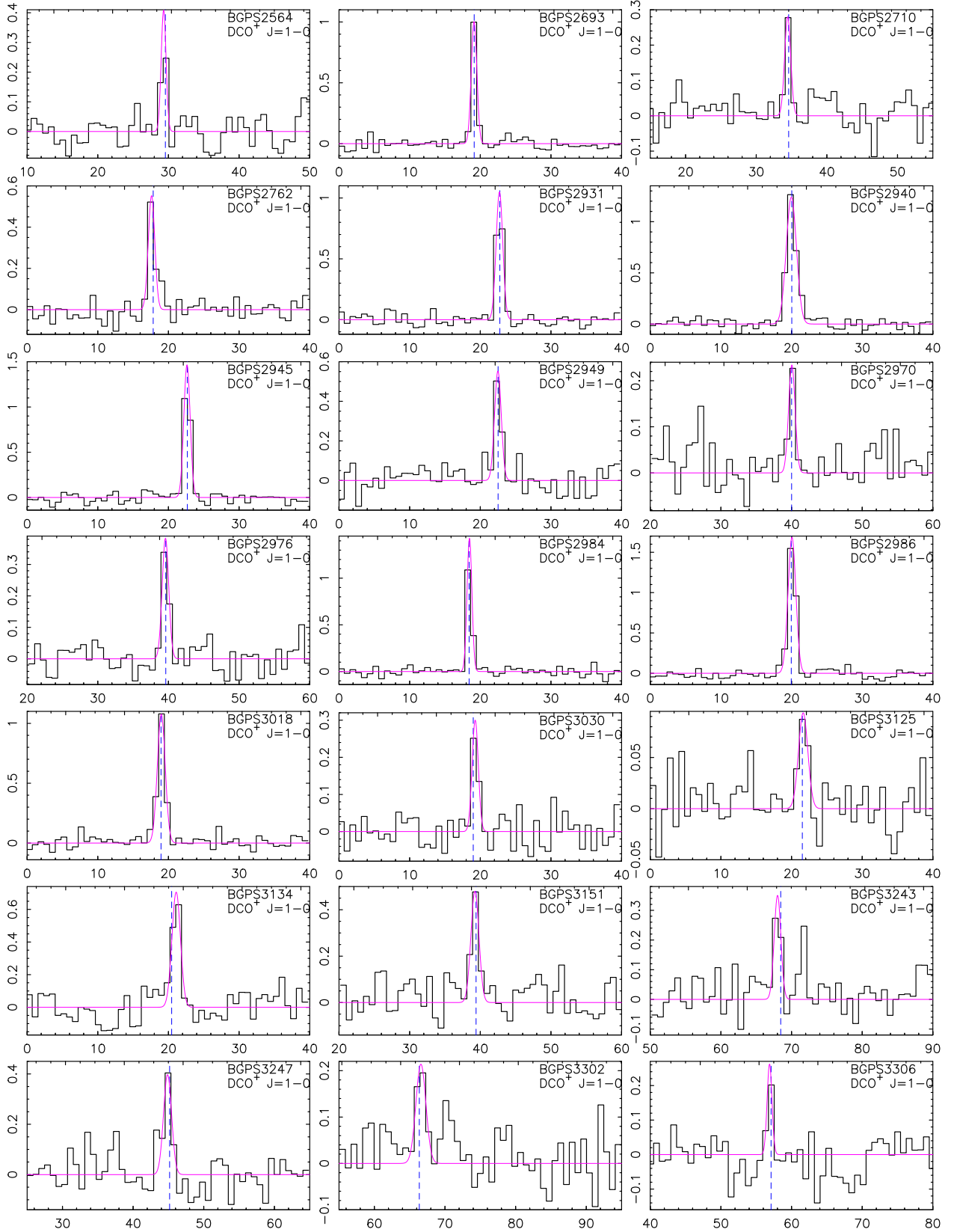


Figure 3. Line profiles of the 46 $\text{DCO}^+ J=1-0$ detected clumps. The Gaussian fitting result for each spectrum is shown in magenta. The blue dashed vertical line represents the LSR velocity of NH_3 for each SCC derived from [Svoboda et al. \(2016\)](#). The x-axis is velocity in km s^{-1} , and the y-axis is T_{mb} in kelvin.

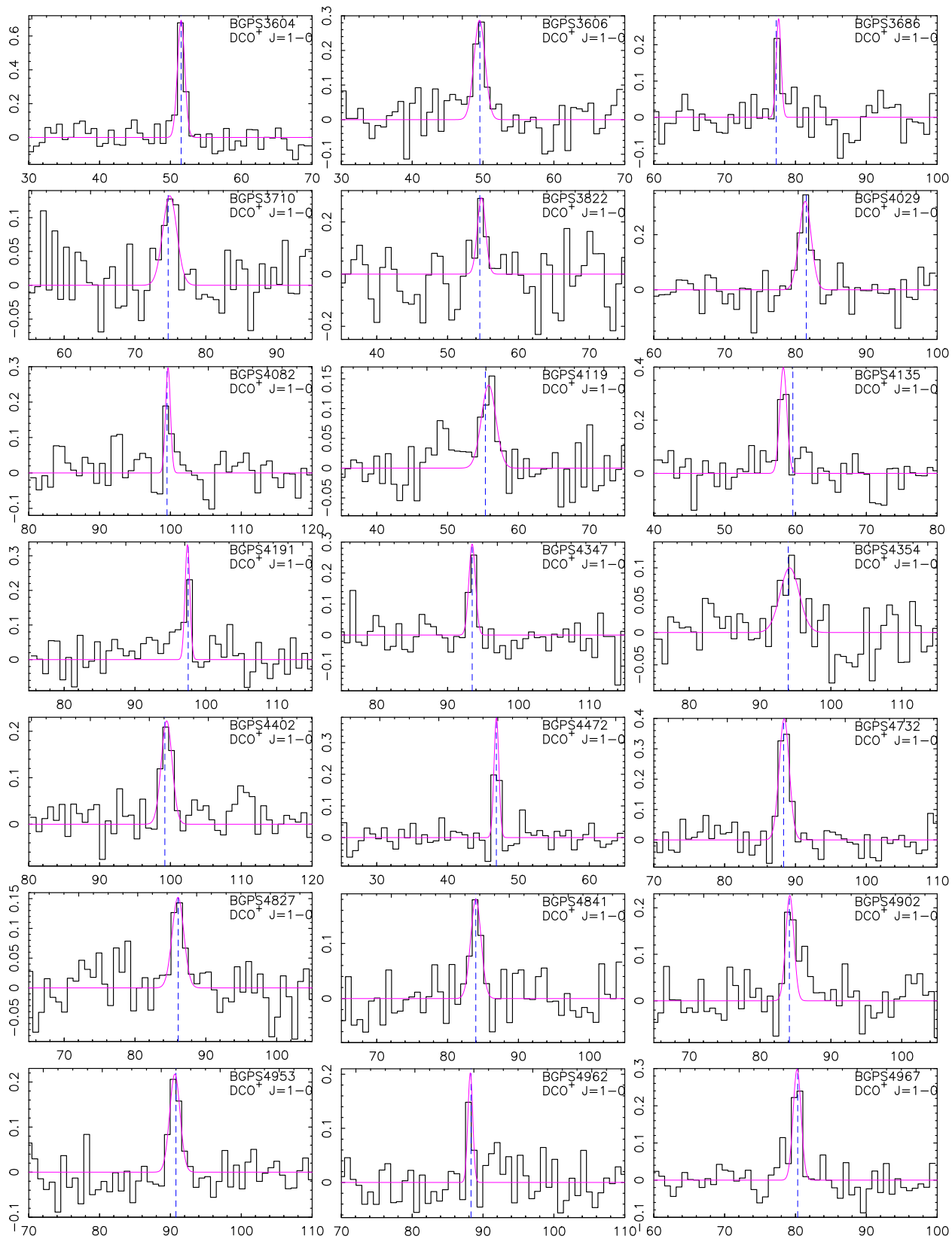


Figure 3. Continued.

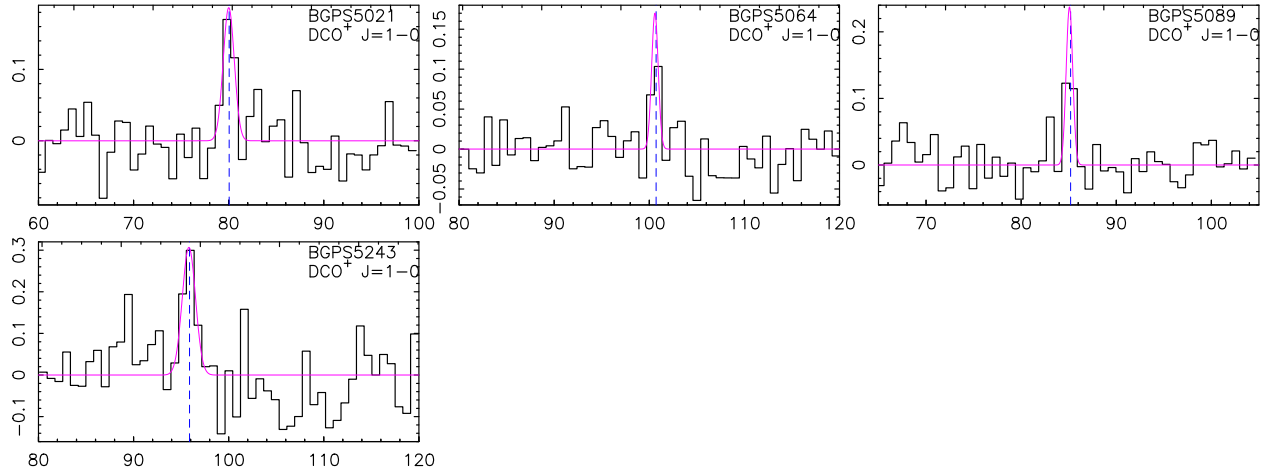


Figure 3. Continued.

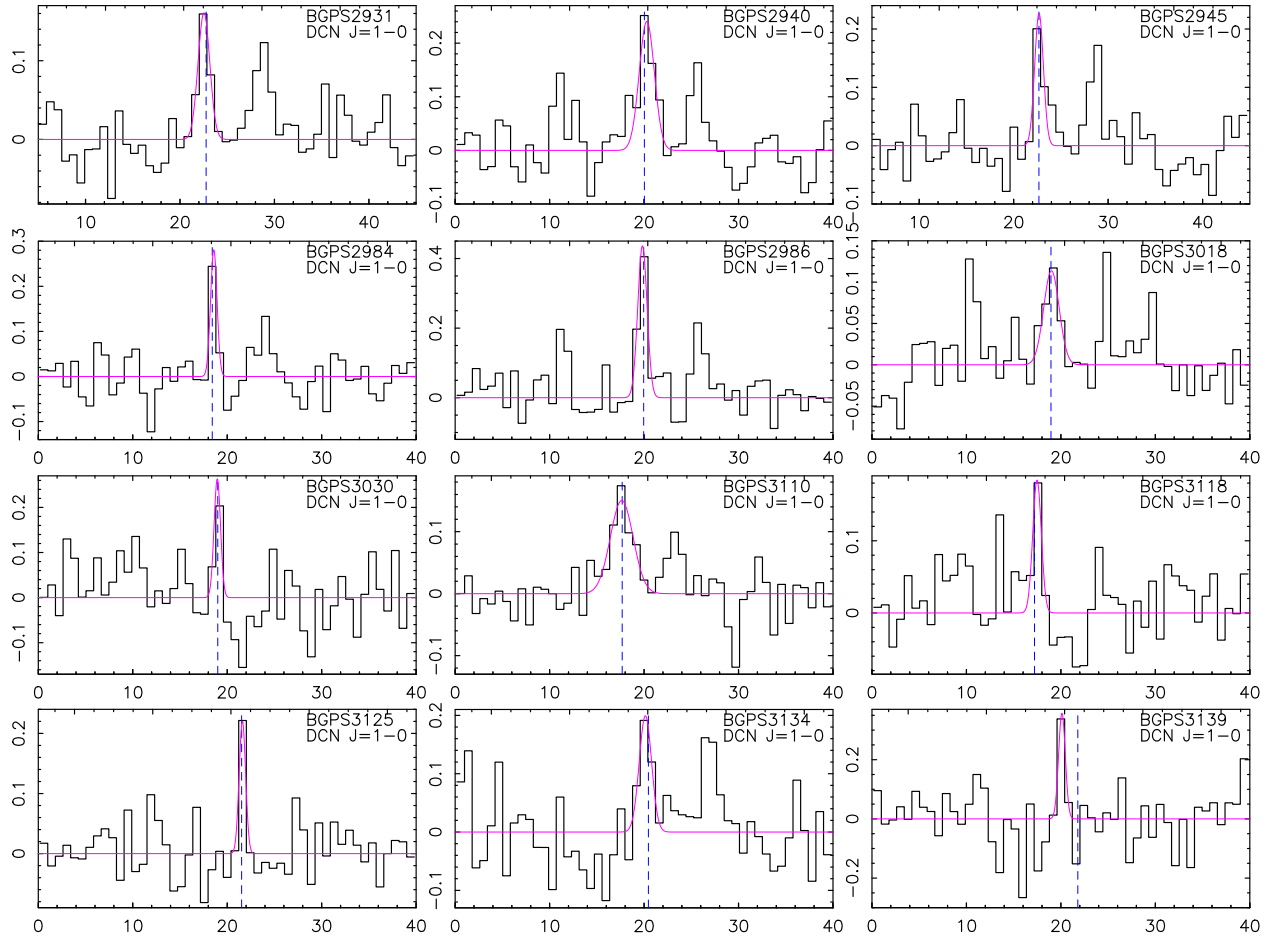


Figure 4. Line profiles of the 12 $\text{DCN } J=1-0$ detected clumps. The Gaussian fitting result for each spectrum is shown in magenta. The blue dashed vertical line represents the LSR velocity of NH_3 for each SCC derived from Svoboda et al. (2016). The x-axis is velocity in km s^{-1} , and the y-axis is T_{mb} in kelvin.

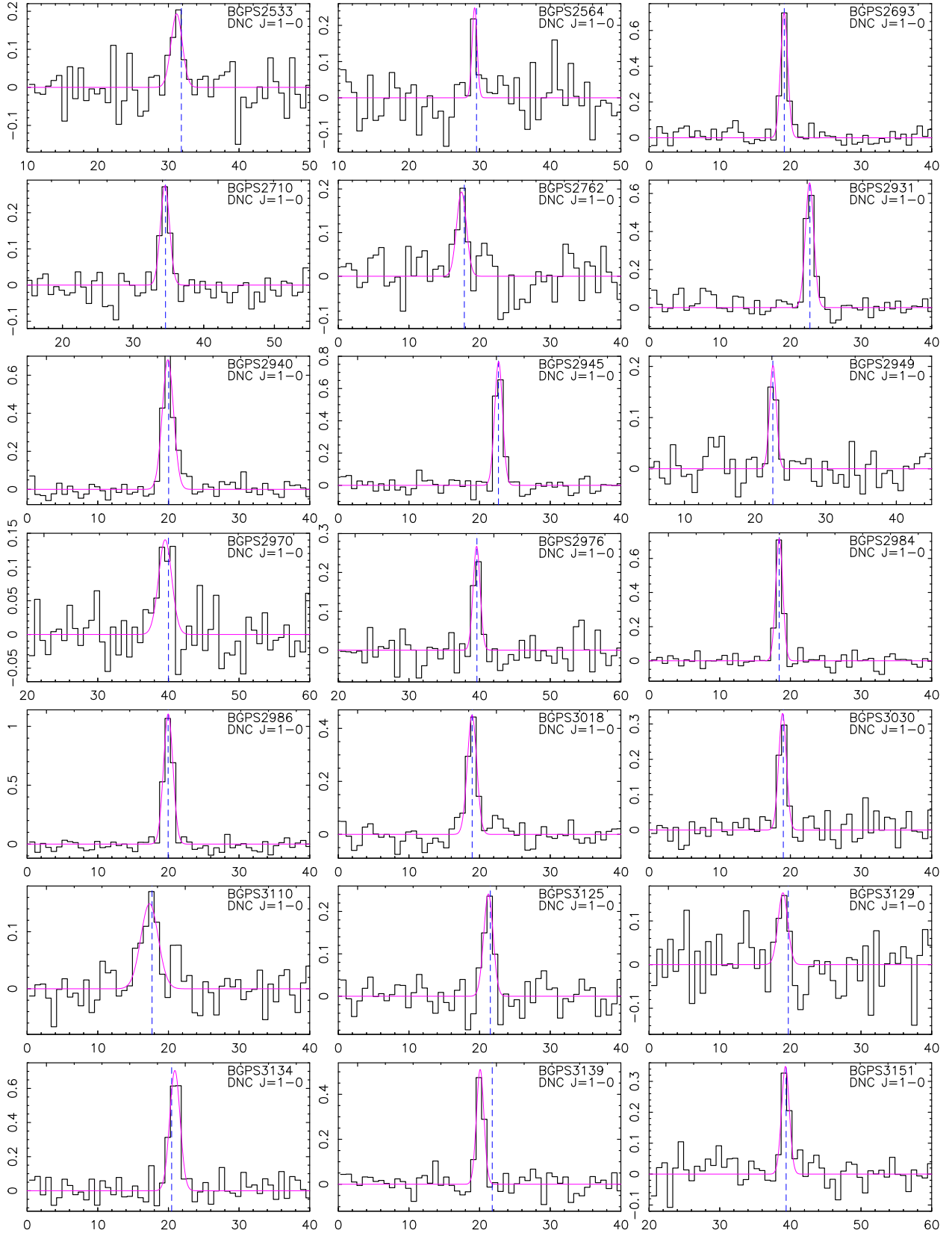


Figure 5. Line profiles of the 51 DNC $J=1-0$ detected clumps. The Gaussian fitting result for each spectrum is shown in magenta. The blue dashed vertical line represents the LSR velocity of NH_3 for each SCC derived from [Svoboda et al. \(2016\)](#). The x-axis is velocity in km s^{-1} , and the y-axis is T_{mb} in kelvin.

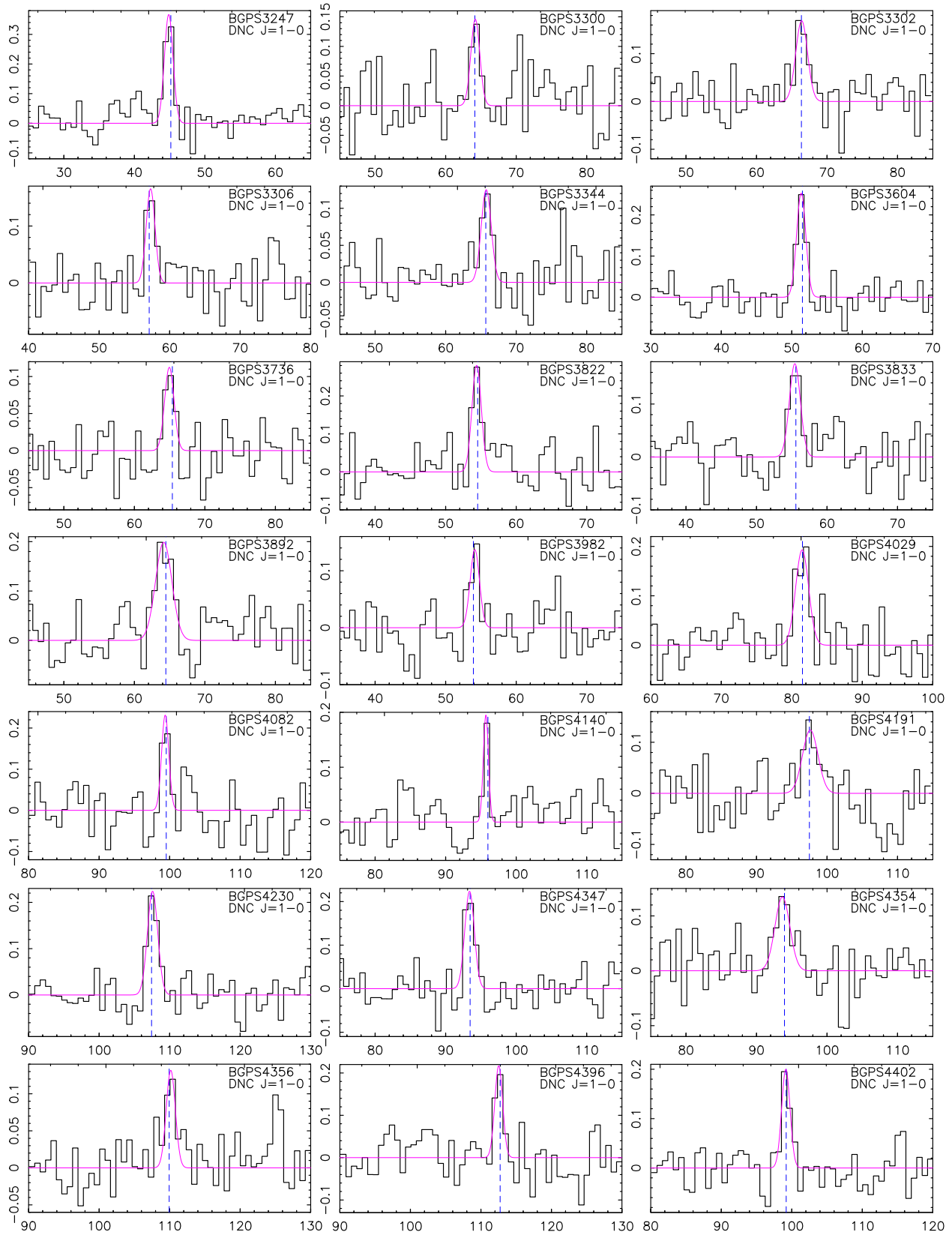


Figure 5. Continued.

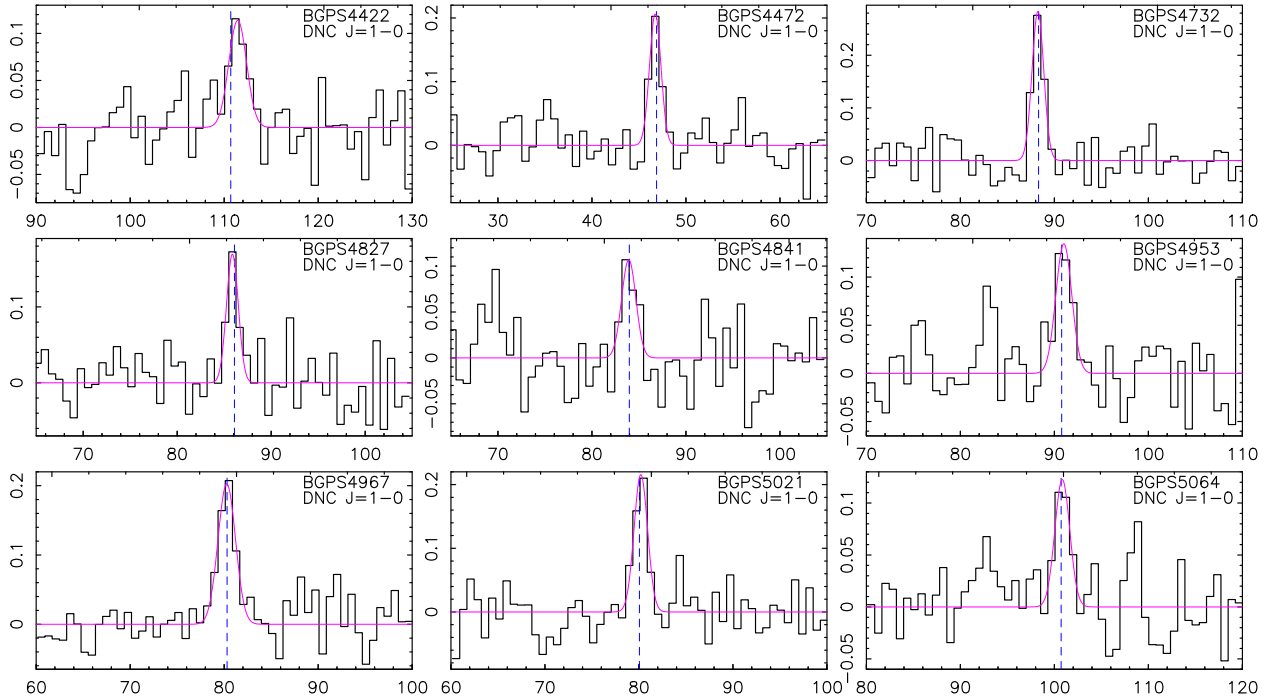


Figure 5. Continued.

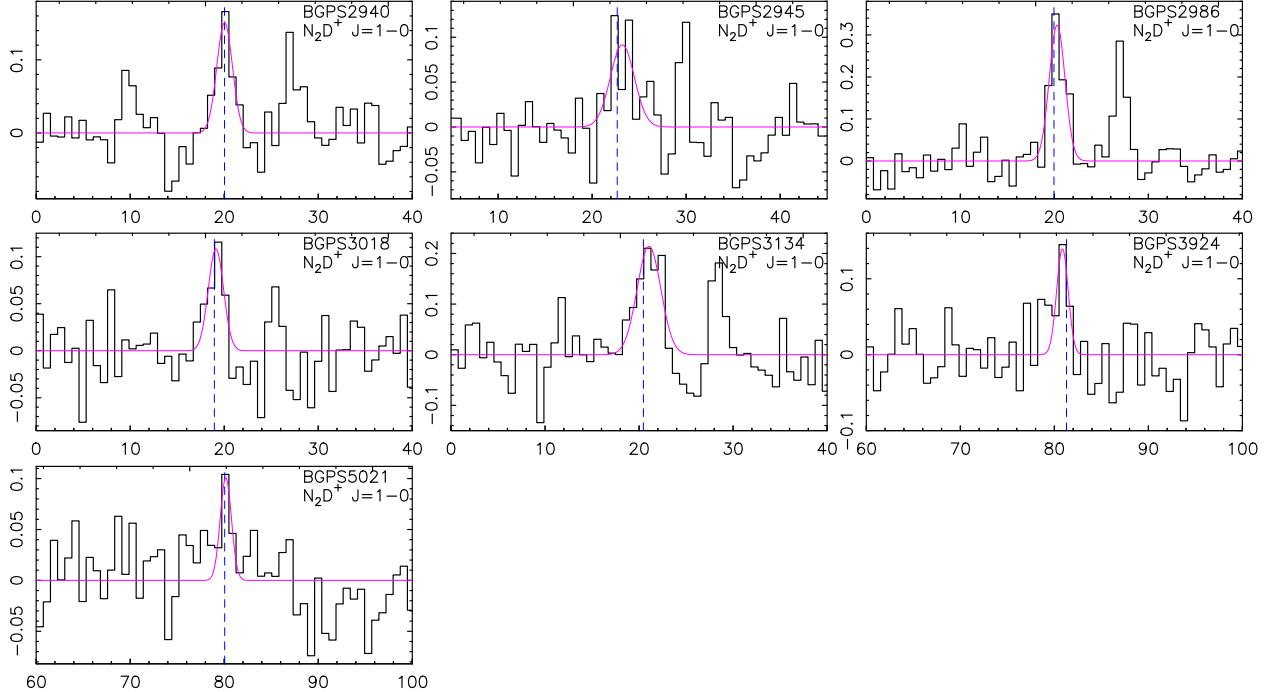


Figure 6. Line profiles of the 7 N_2D^+ $J=1-0$ detected clumps. The Gaussian fitting result for each spectrum is shown in magenta. The blue dashed vertical line represents the LSR velocity of NH_3 for each SCC derived from [Svoboda et al. \(2016\)](#). The x-axis is velocity in km s^{-1} , and the y-axis is T_{mb} in kelvin.

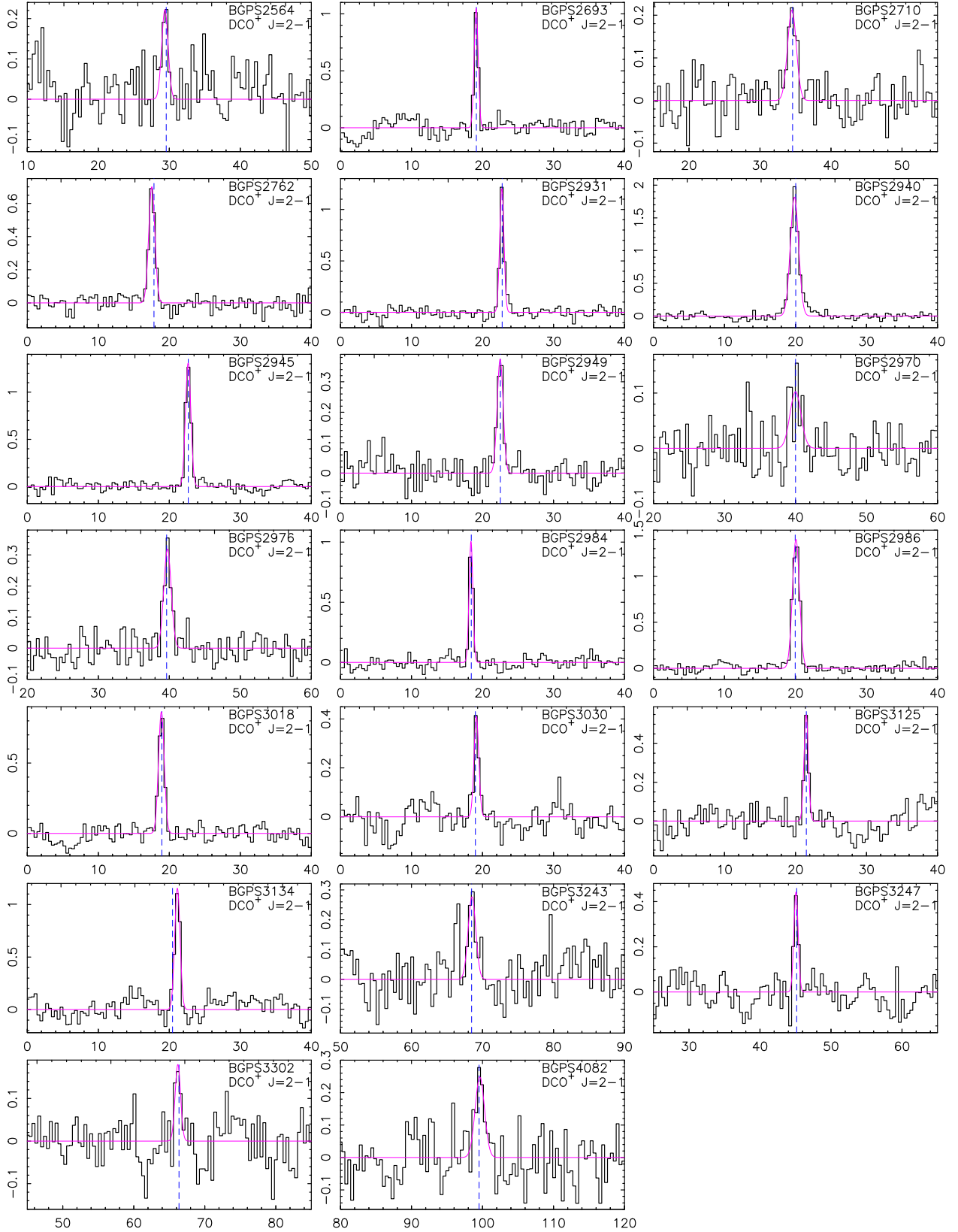


Figure 7. Line profiles of the 20 DCO^+ $J=2-1$ detected clumps. The Gaussian fitting result for each spectrum is shown in magenta. The blue dashed vertical line represents the LSR velocity of NH_3 for each SCC derived from Svoboda et al. (2016). The x-axis is velocity in km s^{-1} , and the y-axis is T_{mb} in kelvin.

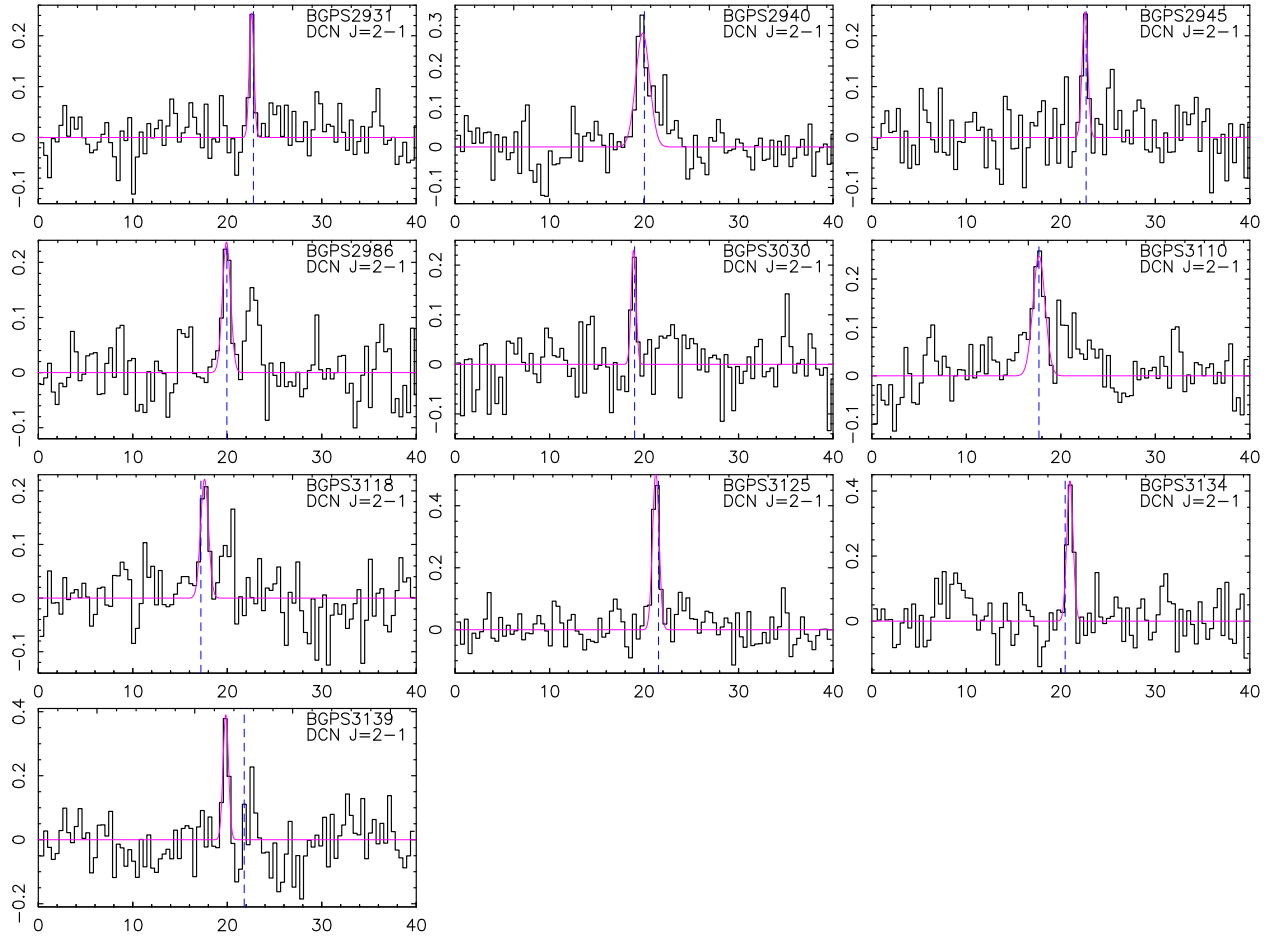


Figure 8. Line profiles of the 10 DCN $J=2-1$ detected clumps. The Gaussian fitting result for each spectrum is shown in magenta. The blue dashed vertical line represents the LSR velocity of NH_3 for each SCC derived from Svoboda et al. (2016). The x-axis is velocity in km s^{-1} , and the y-axis is T_{mb} in kelvin.

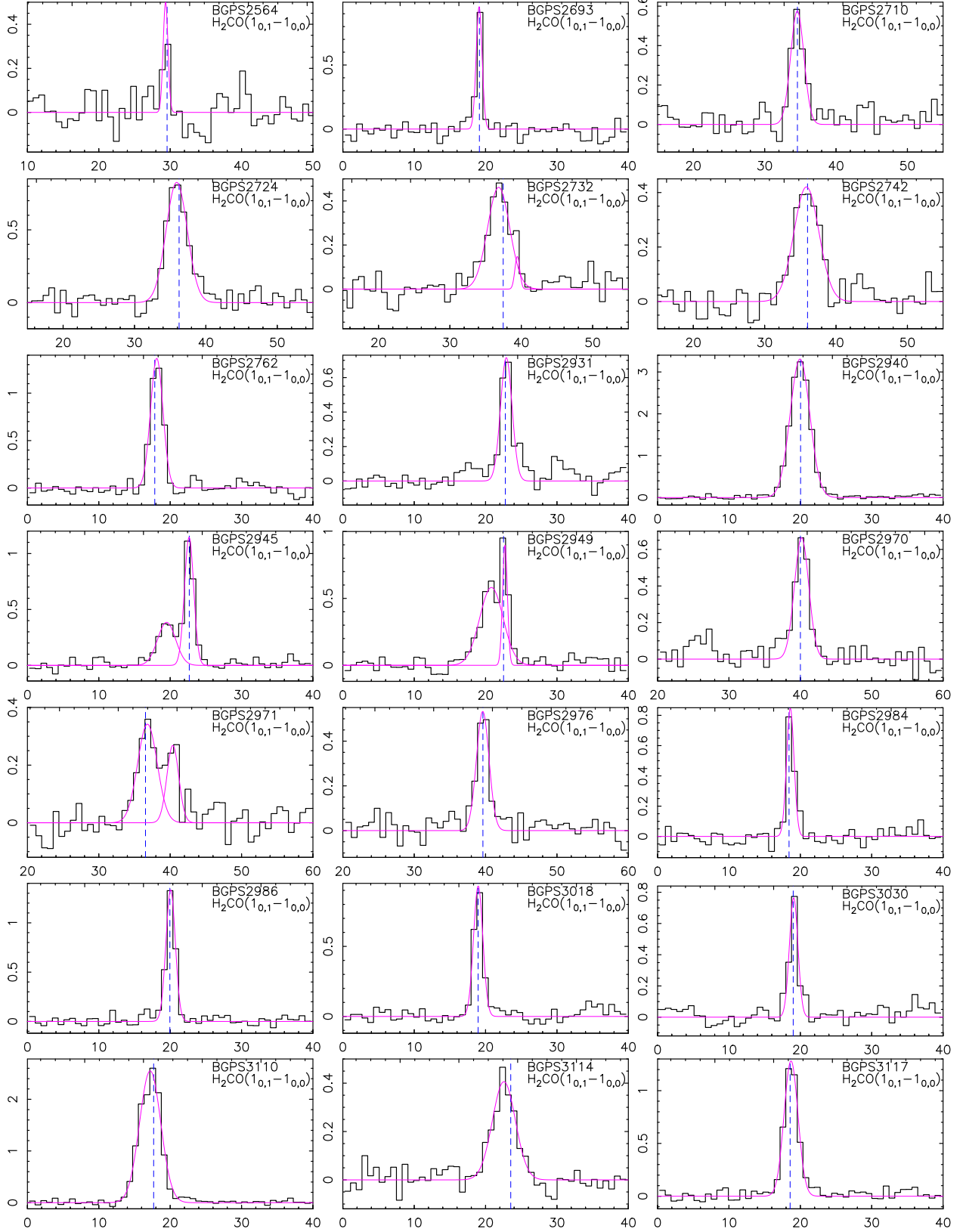


Figure 9. Line profiles of the 91 $\text{H}_2\text{CO}(1_{0,1}-0_{0,0})$ detected clumps. The Gaussian fitting result for each spectrum is shown in magenta. The blue dashed vertical line represents the LSR velocity of NH_3 for each MSCC derived from [Svoboda et al. \(2016\)](#). The x-axis is velocity in km s^{-1} , and the y-axis is T_{mb} in kelvin.

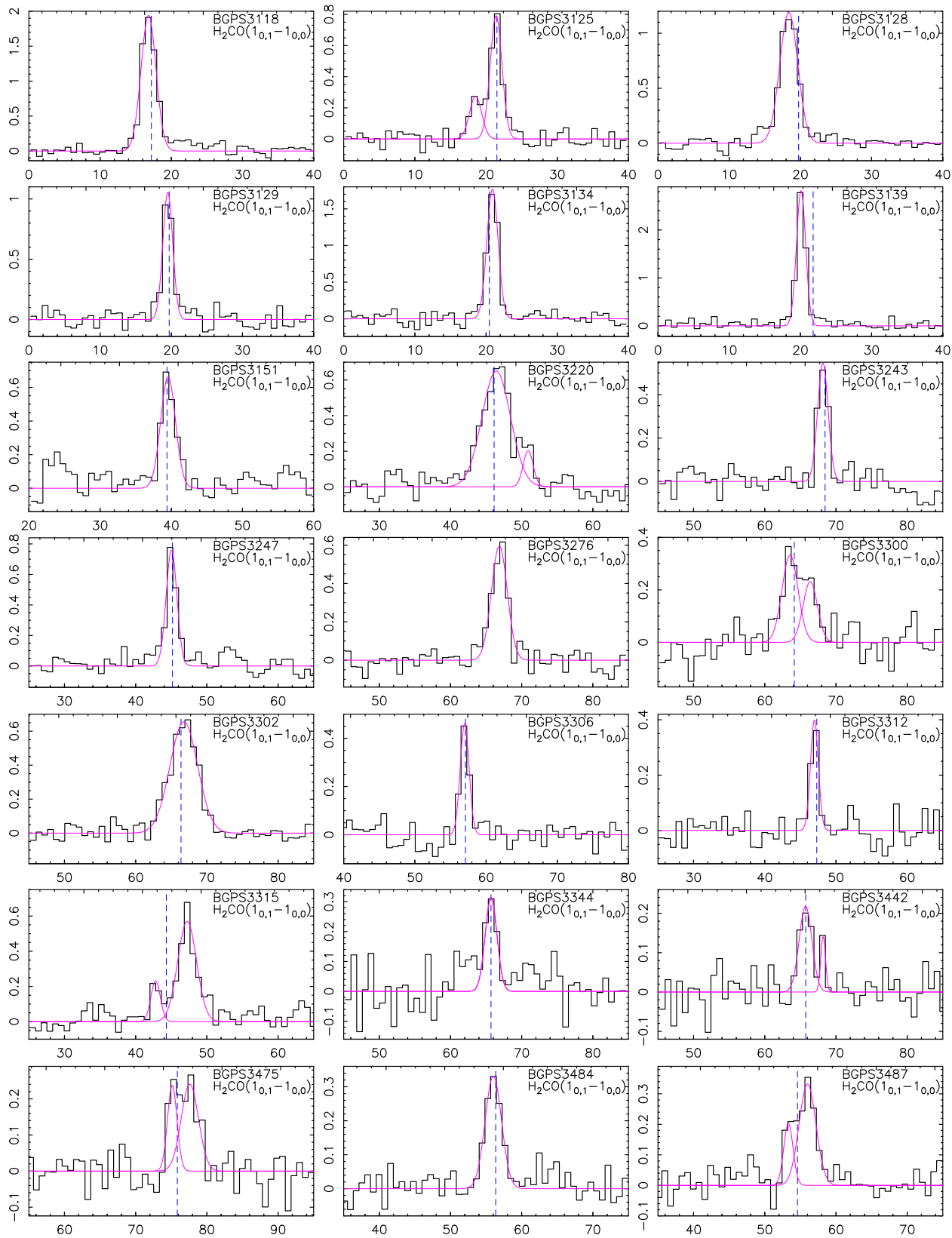


Figure 9. Continued.

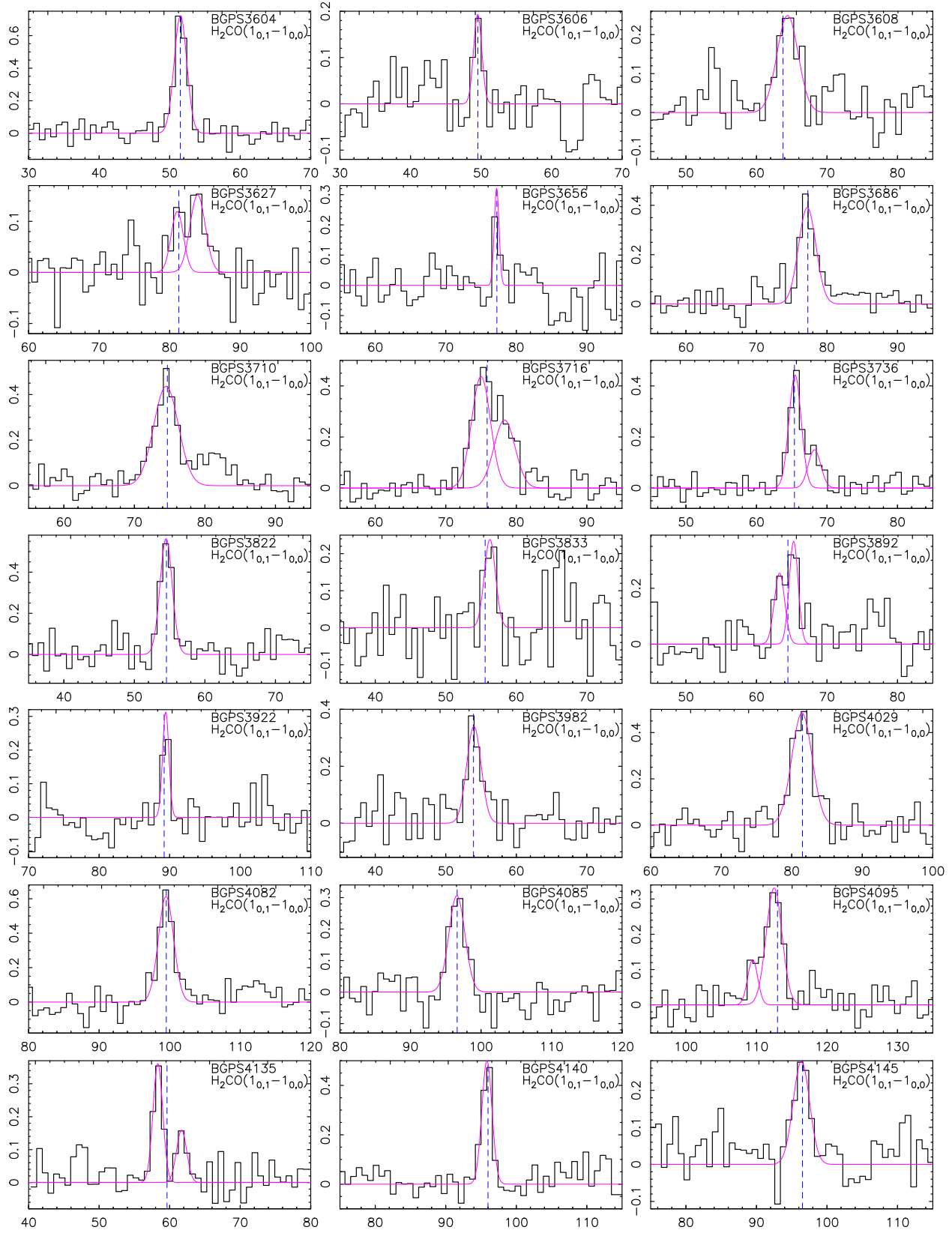


Figure 9. Continued.

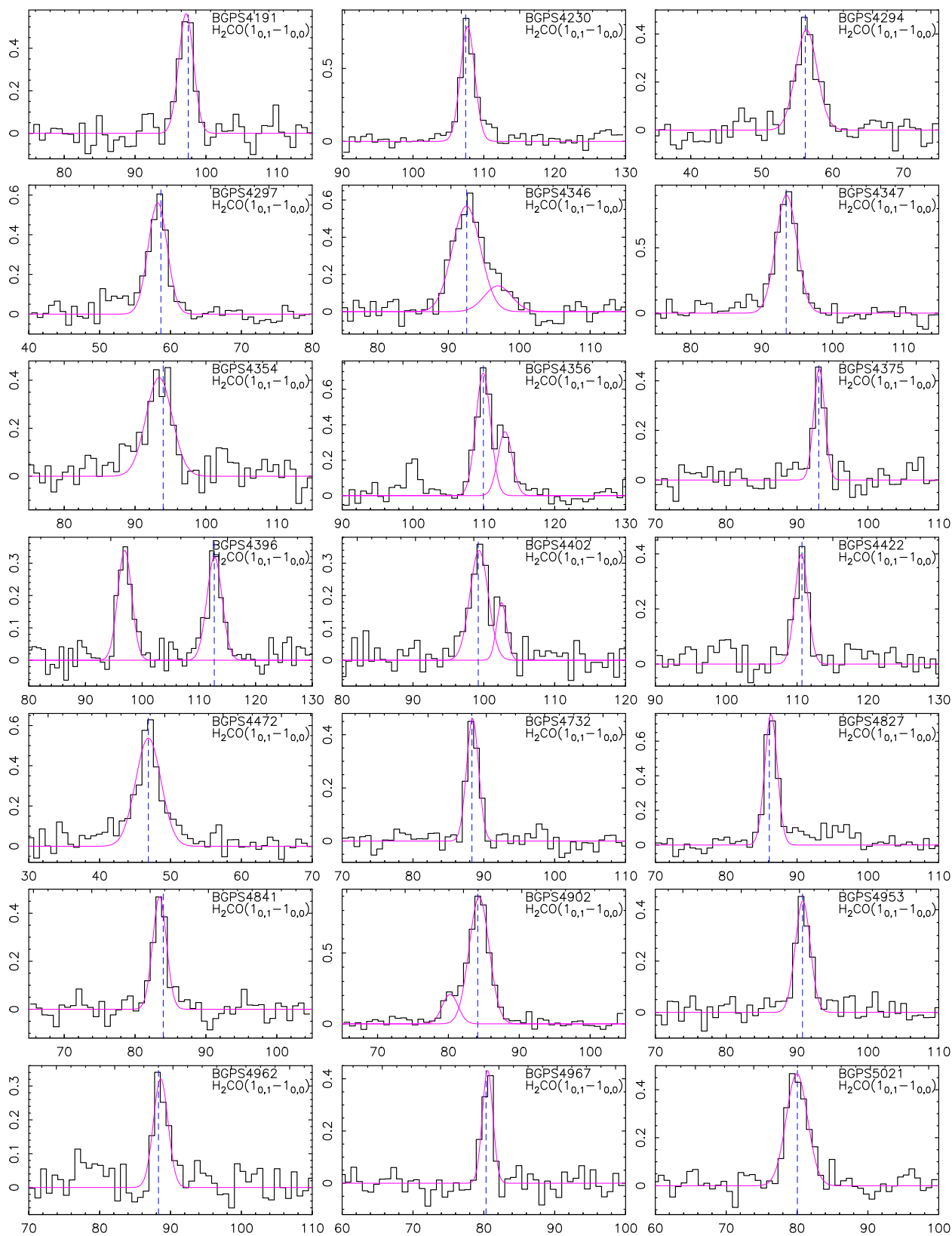
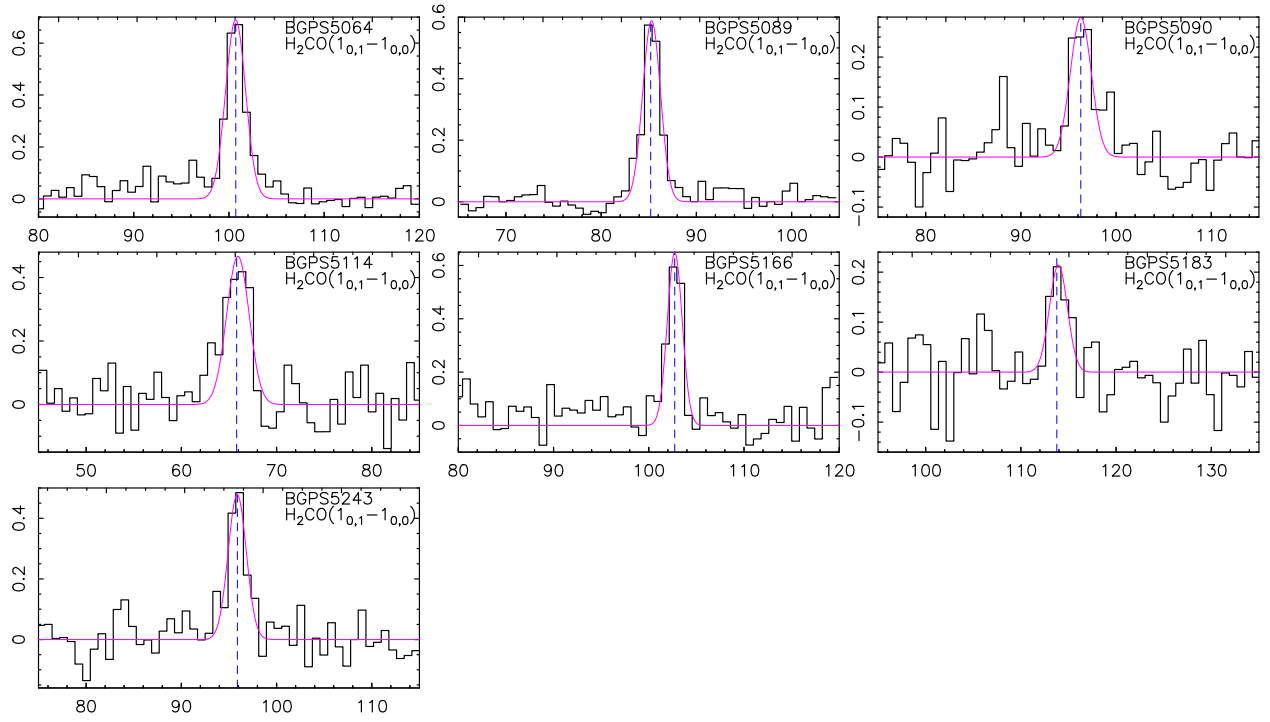


Figure 9. Continued.

**Figure 9.** Continued.

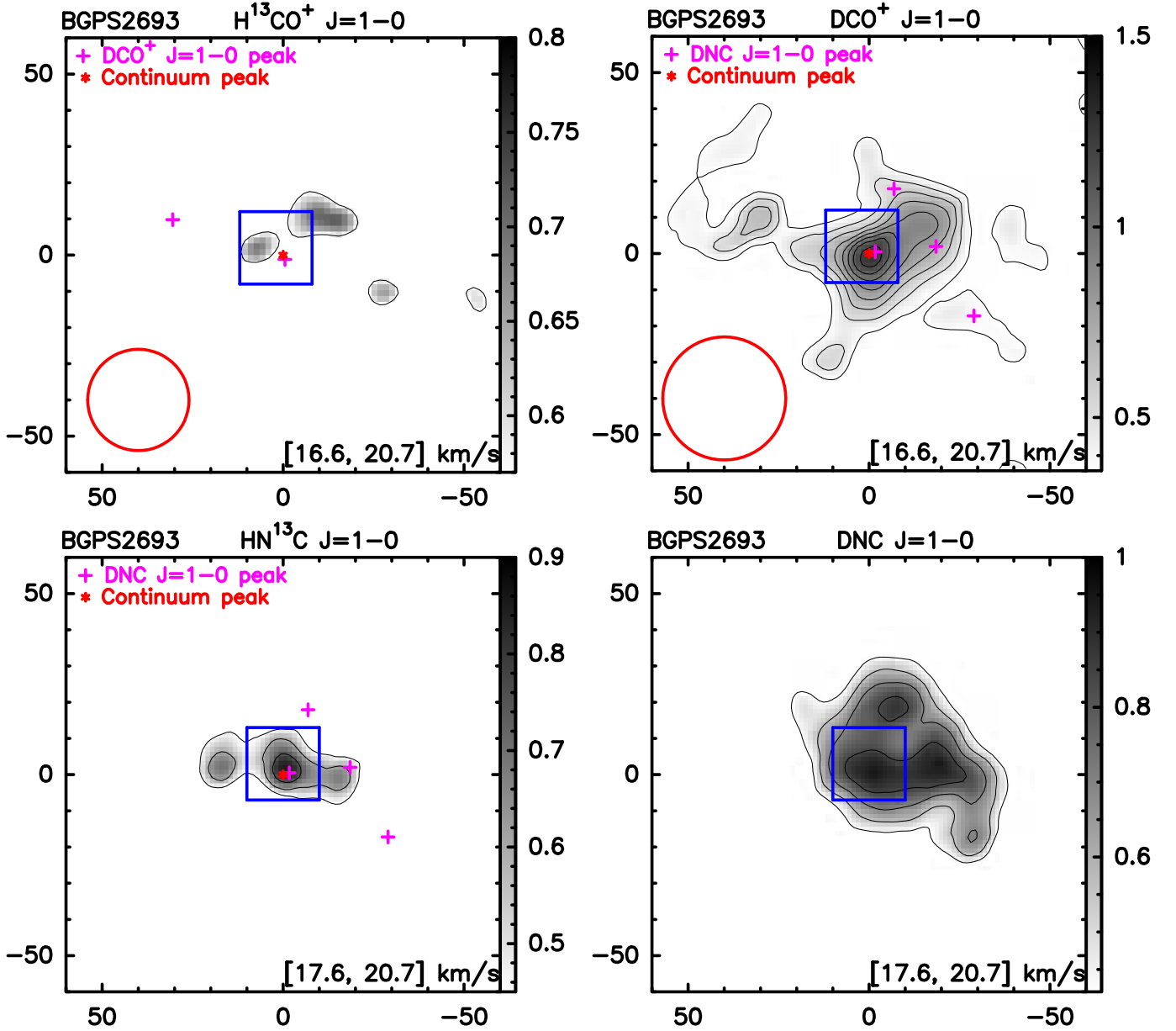


Figure 10. The velocity integrated maps of deuterated and ^{13}C -isotopic molecular lines for BGPS2693. The integrated velocity range, shown at the right-bottom corner, is derived after combining the Gaussian fitting line widths for each pair of deuterated molecular line and ^{13}C -isotopologue. For H^{13}CO^+ , DCO^+ , HN^{13}C , and $\text{DNC } J=1-0$, the contours start from 3σ in steps of 1σ , with $\sigma = 0.19, 0.12, 0.15,$ and 0.14 K km s $^{-1}$, respectively. The crosses represent peaks in the velocity integrated maps of different molecular lines and the red star represents the 1.1mm continuum peak obtained from Svoboda et al. (2016). The beam sizes for H^{13}CO^+ and $\text{DCO}^+ J=1-0$ of $\sim 28''$ and $\sim 34''$ are shown as red circles at the bottom-left corners in their integrated intensity maps. The averaged spectra for column density estimation are derived in the regions enclosed by blue squares.

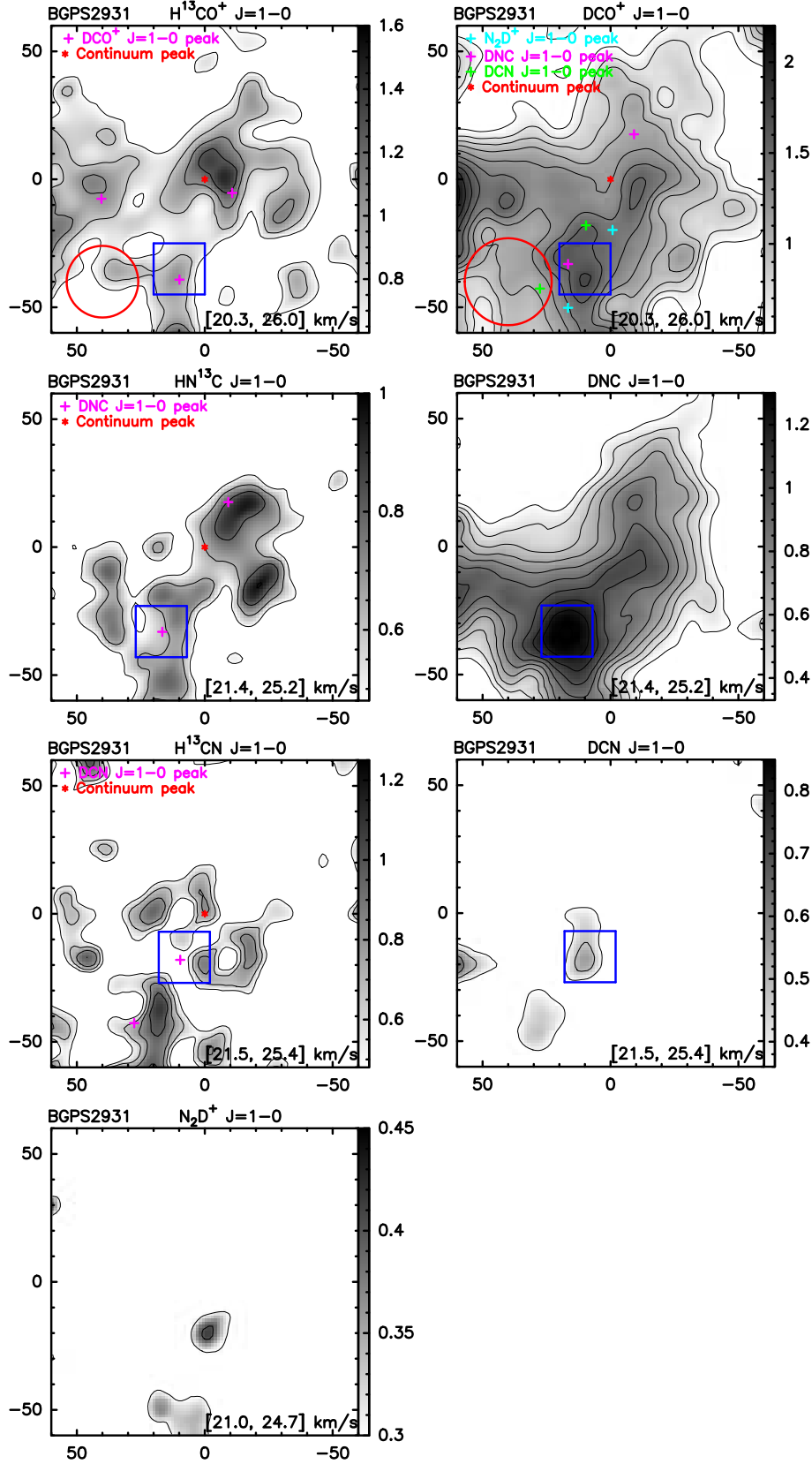


Figure 11. The velocity integrated maps of deuterated and ^{13}C -isotopic molecular lines for BGPS2931. The integrated velocity range, shown at the right-bottom corner, is derived after combining the Gaussian fitting line widths for each pair of deuterated molecular line and ^{13}C -isotopologue. For H^{13}CO^+ , DCO^+ , HN^{13}C , DNC , H^{13}CN , DCN , and N_2D^+ $J=1-0$, the contours start from 3σ in steps of 1σ , with $\sigma = 0.21, 0.18, 0.16, 0.11, 0.16, 0.12,$ and 0.10 K km s^{-1} , respectively. The crosses represent peaks in the velocity integrated maps of different molecular lines and the red star represents the 1.1mm continuum peak obtained from Svoboda et al. (2016). The beam sizes for H^{13}CO^+ and DCO^+ $J=1-0$ of $\sim 28''$ and $\sim 34''$ are shown as red circles at the bottom-left corners in their integrated intensity maps. The averaged spectra for column density estimation are derived in the regions enclosed by blue squares.

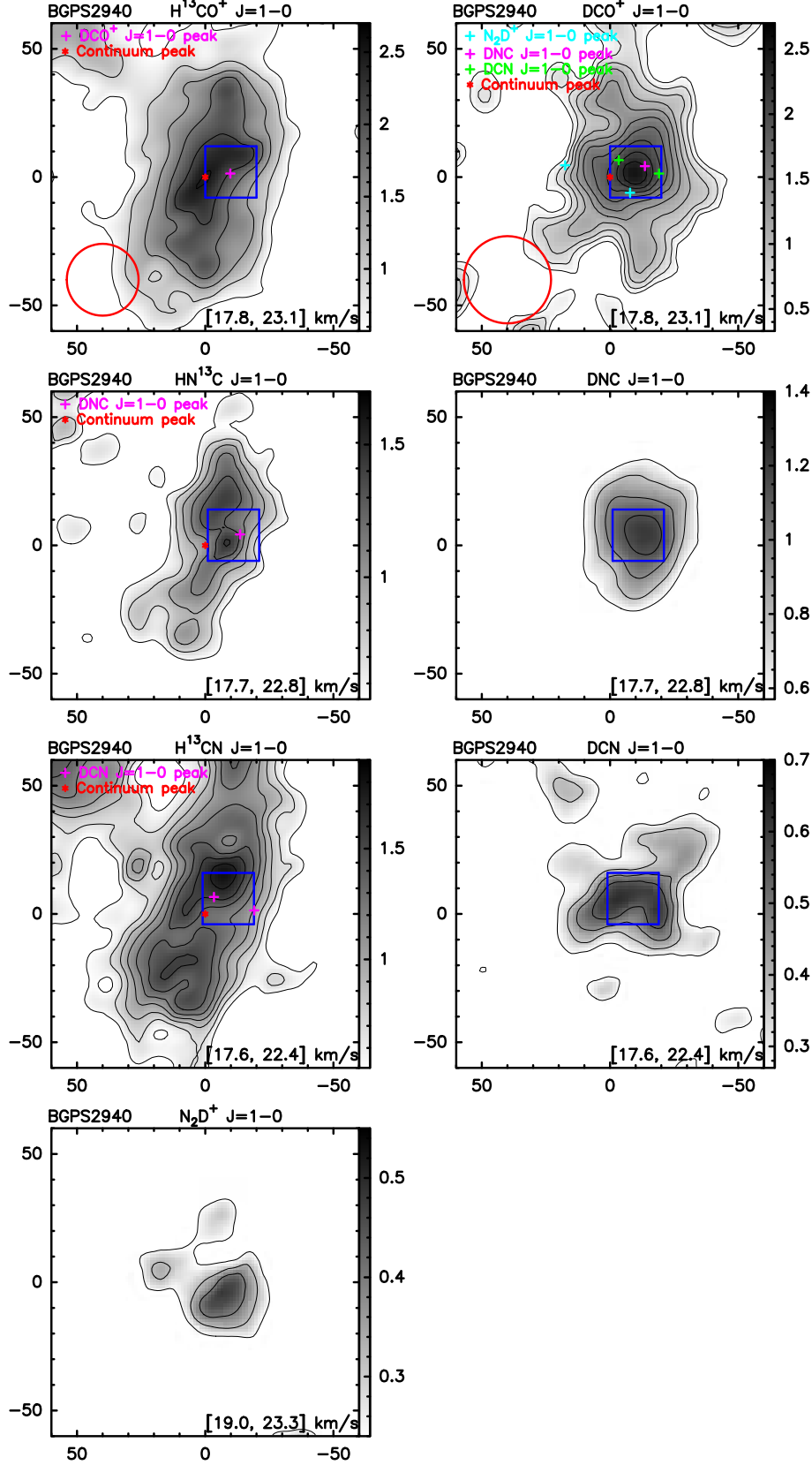


Figure 12. The velocity integrated maps of deuterated and ^{13}C -isotopic molecular lines for BGPS2940. The integrated velocity range, shown at the right-bottom corner, is derived after combining the Gaussian fitting line widths for each pair of deuterated molecular line and ^{13}C -isotopologue. For H^{13}CO^+ and DCO^+ $J=1-0$, the contours start from 3σ in steps of 2σ , with $\sigma = 0.19$ and 0.11 K km s^{-1} , respectively. For HN^{13}C , DNC , H^{13}CN , DCN , and N_2D^+ $J=1-0$, the contours start from 3σ in steps of 1σ , with $\sigma = 0.18, 0.19, 0.17, 0.09,$ and 0.08 K km s^{-1} , respectively. The crosses represent peaks in the velocity integrated maps of different molecular lines and the red star represents the 1.1mm continuum peak obtained from Svoboda et al. (2016). The beam sizes for H^{13}CO^+ and DCO^+ $J=1-0$ of $\sim 28''$ and $\sim 34''$ are shown as red circles at the bottom-left corners in their integrated intensity maps. The averaged spectra for column density estimation are derived in the regions enclosed by blue squares.

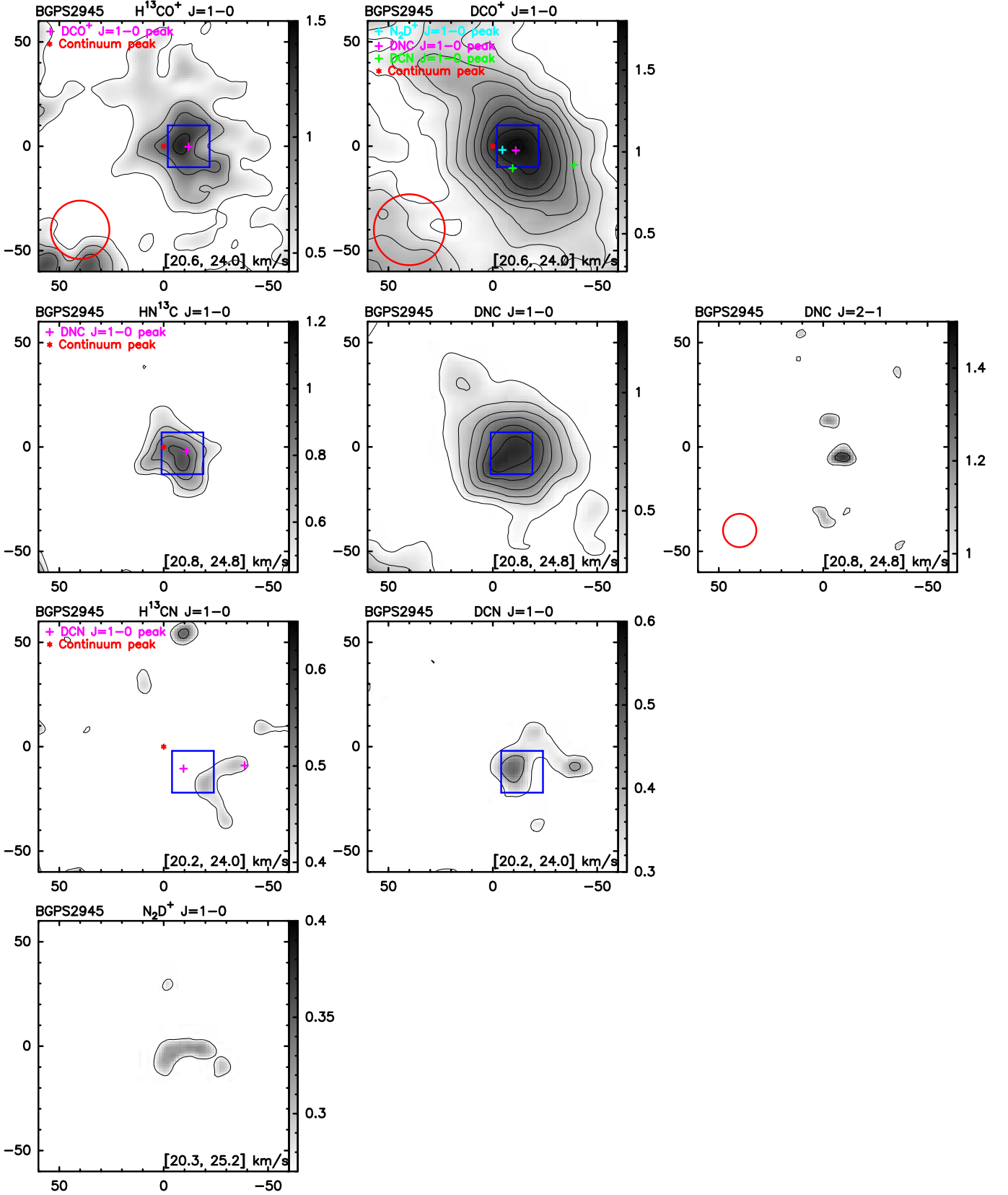


Figure 13. The velocity integrated maps of deuterated and ^{13}C -isotopic molecular lines for BGPS2945. The integrated velocity range, shown at the right-bottom corner, is derived after combining the Gaussian fitting line widths for each pair of deuterated molecular line and ^{13}C -isotopologue. For H^{13}CO^+ , DCO^+ , and $\text{DNC } J=1-0$, the contours start from 3σ in steps of 2σ , with $\sigma = 0.14$, 0.09 , and 0.08 K km s^{-1} , respectively. For HN^{13}C , H^{13}CN , DCN , $\text{N}_2\text{D}^+ J=1-0$, and $\text{DNC } J=2-1$, the contours start from 3σ in steps of 1σ , with $\sigma = 0.15$, 0.13 , 0.10 , 0.09 , and 0.32 K km s^{-1} , respectively. The crosses represent peaks in the velocity integrated maps of different molecular lines and the red star represents the 1.1mm continuum peak obtained from Svoboda et al. (2016). The beam sizes for H^{13}CO^+ , $\text{DCO}^+ J=1-0$ and $\text{DNC } J=2-1$ of $\sim 28''$, $\sim 34''$, and $\sim 16''$ are shown as red circles at the bottom-left corners in their integrated intensity maps. The averaged spectra for column density estimation are derived in the regions enclosed by blue squares.

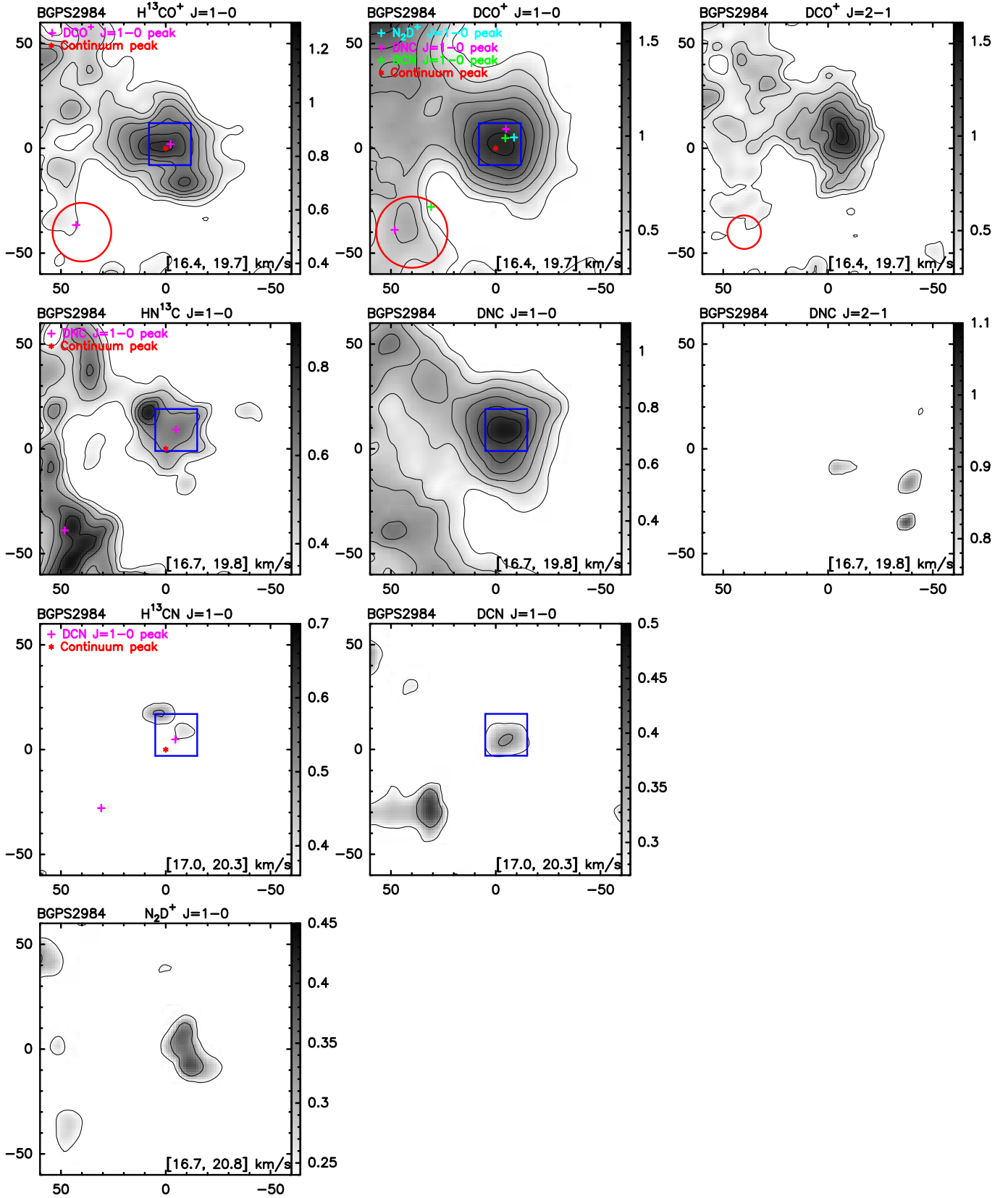


Figure 14. The velocity integrated maps of deuterated and ^{13}C -isotopic molecular lines for BGPS2984. The integrated velocity range, shown at the right-bottom corner, is derived after combining the Gaussian fitting line widths for each pair of deuterated molecular line and ^{13}C -isotopologue. For H^{13}CO^+ , DCO^+ , $\text{DNC } J=1-0$ and $\text{DCO}^+ J=2-1$, the contours start from 3σ in steps of 2σ , with $\sigma = 0.12, 0.09, 0.07$, and 0.09 K km s^{-1} , respectively. For HN^{13}C , H^{13}CN , DCN , $\text{N}_2\text{D}^+ J=1-0$, and $\text{DNC } J=2-1$, the contours start from 3σ in steps of 1σ , with $\sigma = 0.11, 0.12, 0.09, 0.08$, and 0.25 K km s^{-1} , respectively. The crosses represent peaks in the velocity integrated maps of different molecular lines and the red star represents the 1.1mm continuum peak obtained from Svoboda et al. (2016). The beam sizes for H^{13}CO^+ , $\text{DCO}^+ J=1-0$ and $\text{DCO}^+ J=2-1$ of $\sim 28''$, $\sim 34''$, and $\sim 16''$ are shown as red circles at the bottom-left corners in their integrated intensity maps. The averaged spectra for column density estimation are derived in the regions enclosed by blue squares.

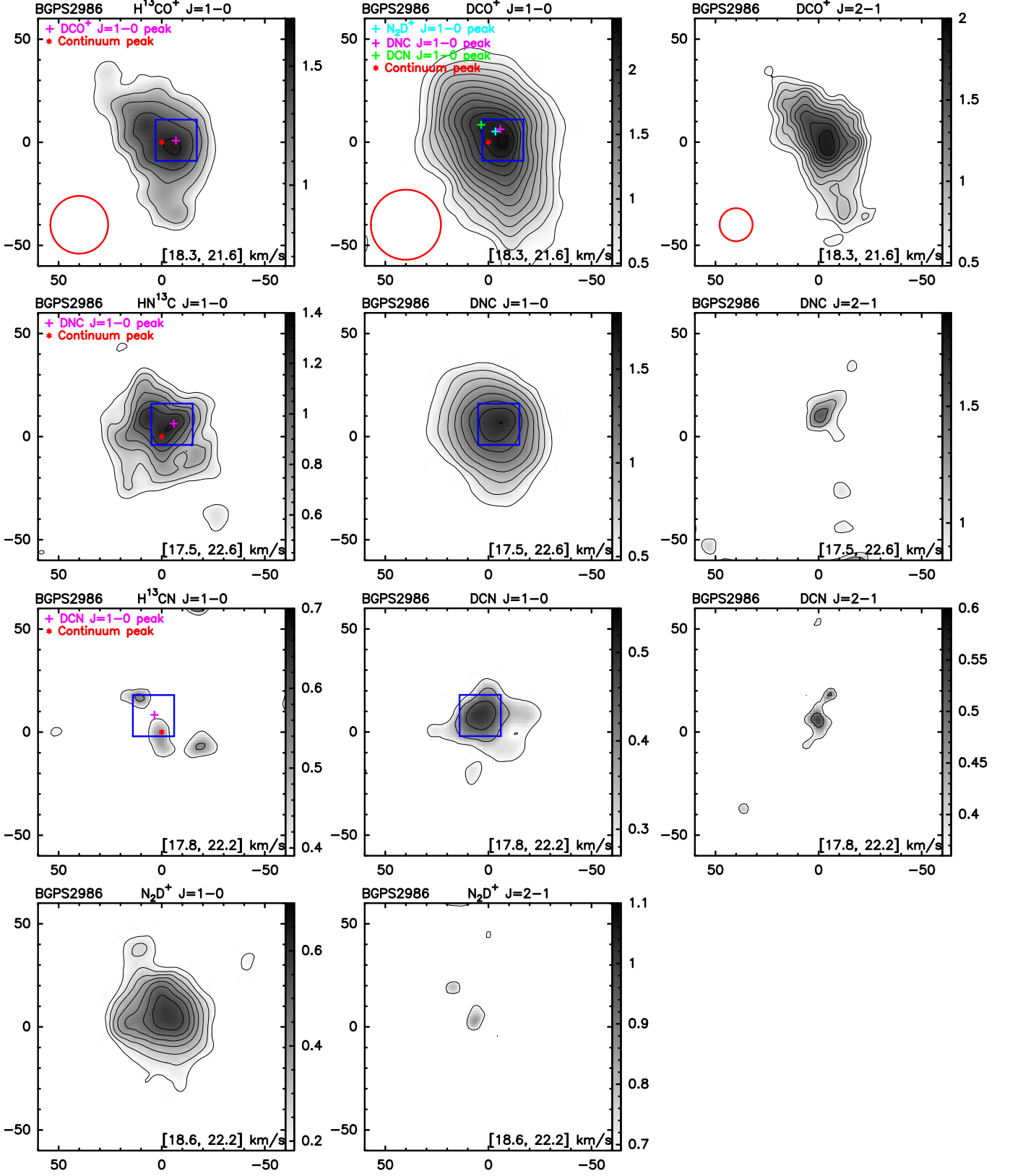


Figure 15. The velocity integrated maps of deuterated and ^{13}C -isotopic molecular lines for BGPS2986. The integrated velocity range, shown at the right-bottom corner, is derived after combining the Gaussian fitting line widths for each pair of deuterated molecular line and ^{13}C -isotopologue. For H^{13}CO^+ , DCO^+ , $\text{DNC } J=1-0$ and $\text{DCO}^+ J=2-1$, the contours start from 6σ in steps of 2σ , with $\sigma = 0.11, 0.08, 0.08$, and 0.08 K km s^{-1} , respectively. For HN^{13}C , H^{13}CN , DCN , $\text{N}_2\text{D}^+ J=1-0$, and DNC , DCN , $\text{N}_2\text{D}^+ J=2-1$, the contours start from 3σ in steps of 1σ , with $\sigma = 0.14, 0.13, 0.09, 0.06, 0.28, 0.09$, and 0.23 K km s^{-1} , respectively. The crosses represent peaks in the velocity integrated maps of different molecular lines and the red star represents the 1.1mm continuum peak obtained from Svoboda et al. (2016). The beam sizes for H^{13}CO^+ , $\text{DCO}^+ J=1-0$ and $\text{DCO}^+ J=2-1$ of $\sim 28''$, $\sim 34''$, and $\sim 16''$ are shown as red circles at the bottom-left corners in their integrated intensity maps. The averaged spectra for column density estimation are derived in the regions enclosed by blue squares.

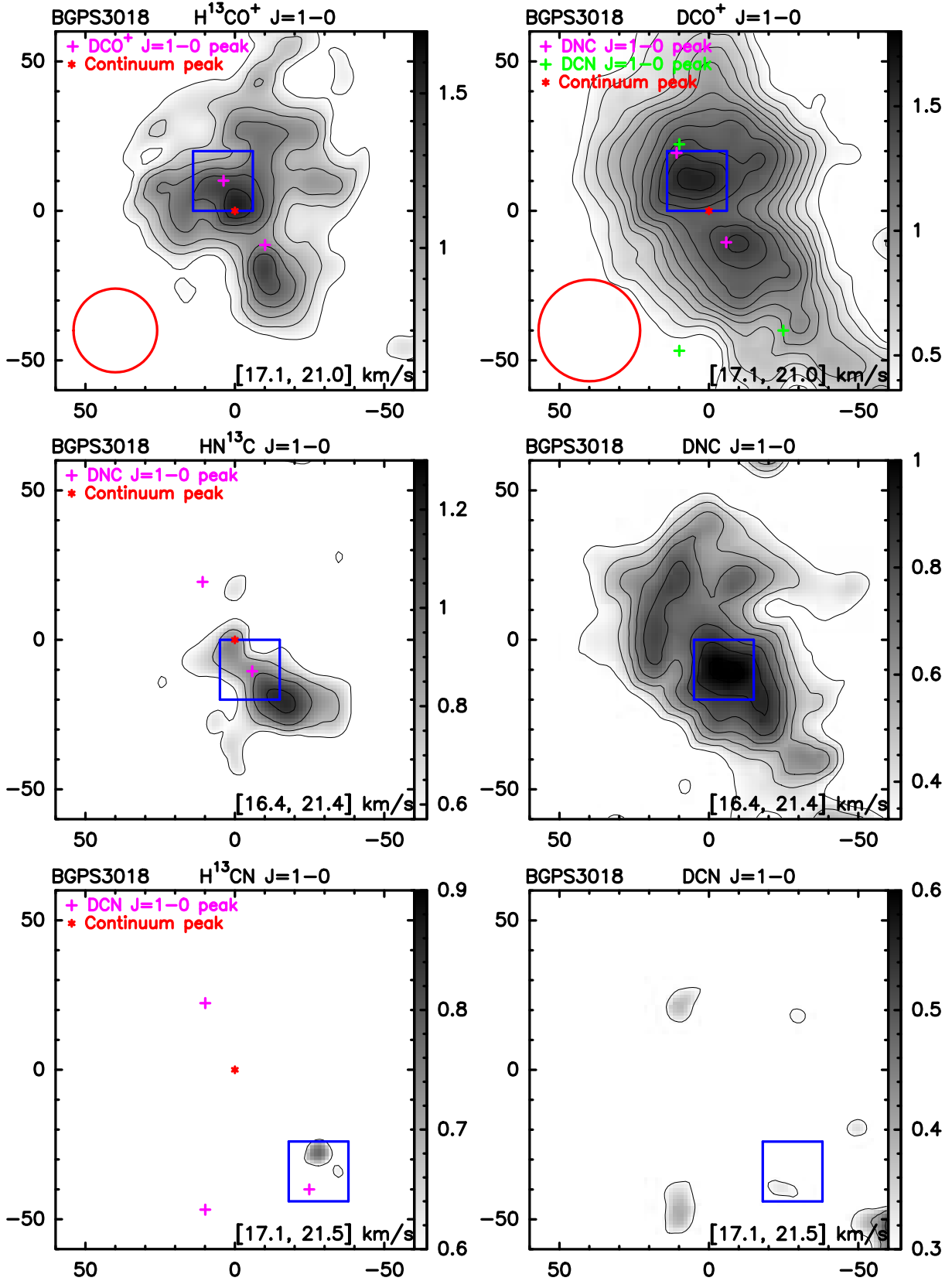


Figure 16. The velocity integrated maps of deuterated and ^{13}C -isotopic molecular lines for BGPS3018. The integrated velocity range, shown at the right-bottom corner, is derived after combining the Gaussian fitting line widths for each pair of deuterated molecular line and ^{13}C -isotopologue. For H^{13}CO^+ , DCO^+ , HN^{13}C , DNC , H^{13}CN , and $\text{DCN} J=1-0$, the contours start from 3σ in steps of 1σ , with $\sigma = 0.18, 0.12, 0.19, 0.11, 0.19$, and 0.10 K km s^{-1} , respectively. The crosses represent peaks in the velocity integrated maps of different molecular lines and the red star represents the 1.1mm continuum peak obtained from Svoboda et al. (2016). The beam sizes for H^{13}CO^+ and $\text{DCO}^+ J=1-0$ of $\sim 28''$ and $\sim 34''$ are shown as red circles at the bottom-left corners in their integrated intensity maps. The averaged spectra for column density estimation are derived in the regions enclosed by blue squares.

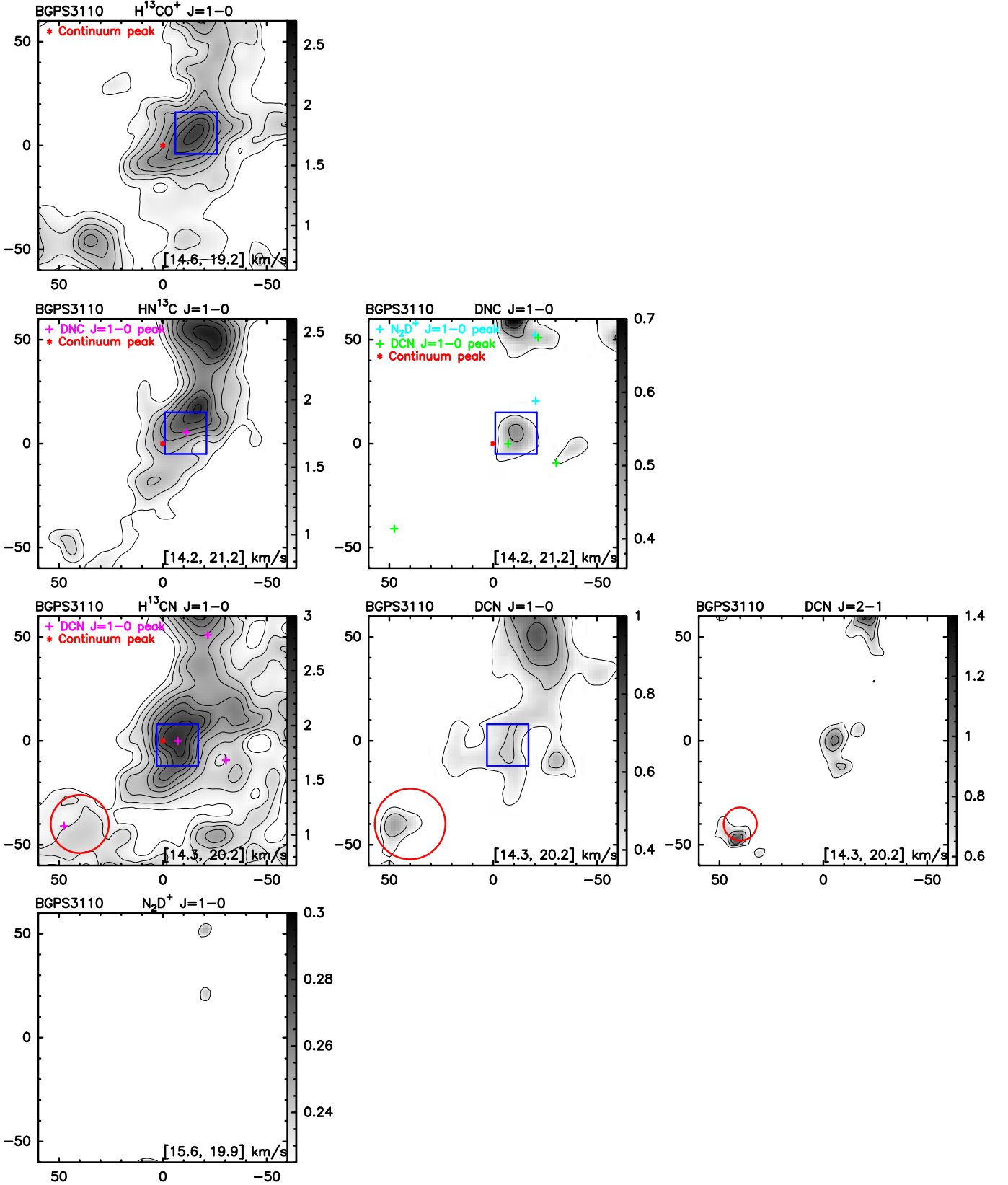


Figure 17. The velocity integrated maps of deuterated and ^{13}C -isotopic molecular lines for BGPS3110. The integrated velocity range, shown at the right-bottom corner, is derived after combining the Gaussian fitting line widths for each pair of deuterated molecular line and ^{13}C -isotopologue. For H^{13}CO^+ , HN^{13}C , DNC , H^{13}CN , DCN , N_2D^+ $J=1-0$, and $\text{DCN } J=2-1$, the contours start from 3σ in steps of 1σ , with $\sigma = 0.21, 0.25, 0.12, 0.24, 0.12, 0.08$, and 0.19 K km s^{-1} , respectively. The crosses represent peaks in the velocity integrated maps of different molecular lines and the red star represents the 1.1mm continuum peak obtained from Svoboda et al. (2016). The beam sizes for H^{13}CN , $\text{DCN } J=1-0$ and $\text{DCN } J=2-1$ of $\sim 28''$, $\sim 34''$, and $\sim 16''$ are shown as red circles at the bottom-left corners in their integrated intensity maps. The averaged spectra for column density estimation are derived in the regions enclosed by blue squares.

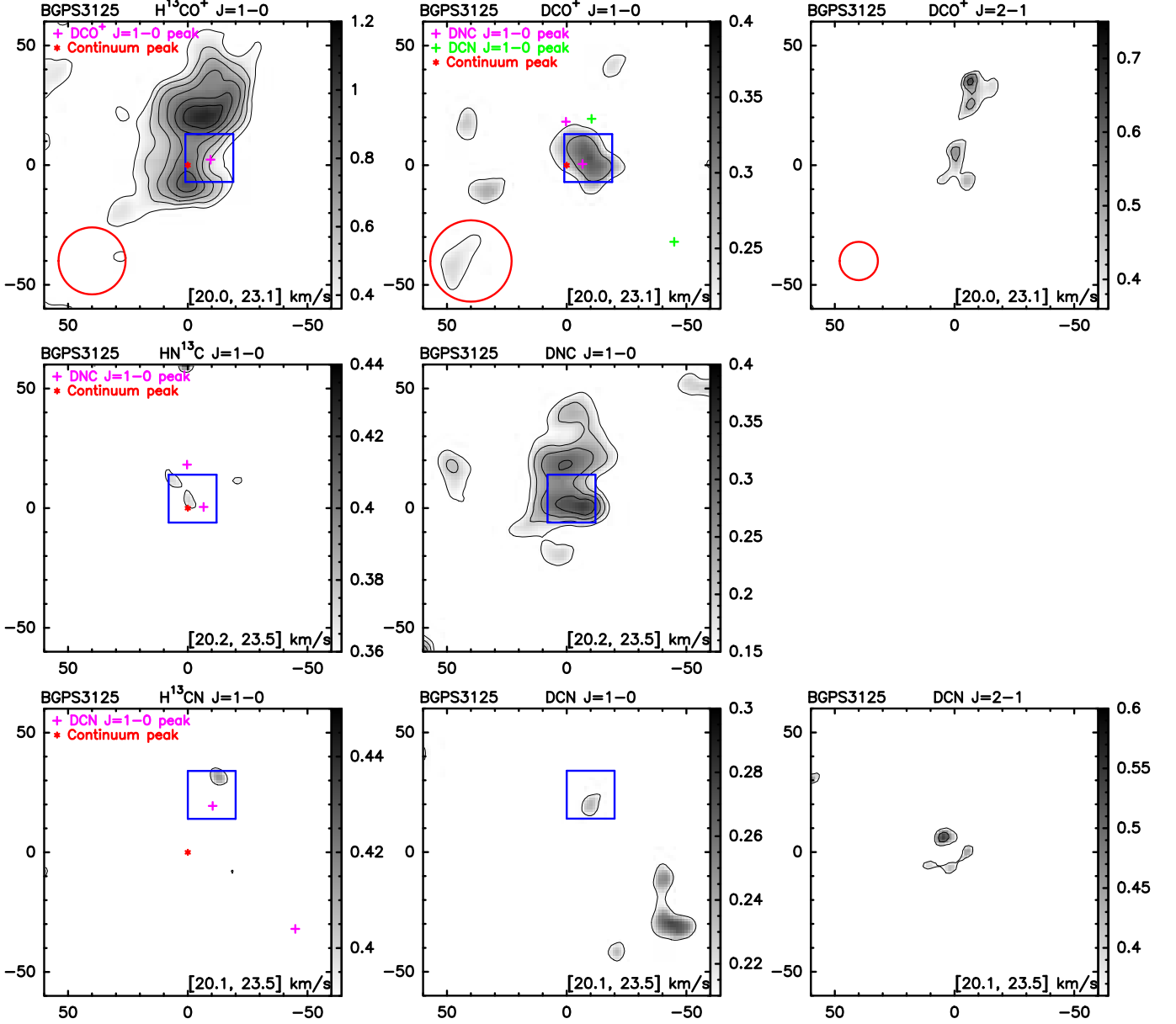


Figure 18. The velocity integrated maps of deuterated and ^{13}C -isotopic molecular lines for BGPS3125. The integrated velocity range, shown at the right-bottom corner, is derived after combining the Gaussian fitting line widths for each pair of deuterated molecular line and ^{13}C -isotopologue. For H^{13}CO^+ , DCO^+ , HN^{13}C , DNC , H^{13}CN , $\text{DCN } J=1-0$, and DCO^+ , $\text{DCN } J=2-1$, the contours start from 3σ in steps of 1σ , with $\sigma = 0.12, 0.07, 0.12, 0.05, 0.13, 0.08, 0.11$, and 0.12 K km s^{-1} , respectively. The crosses represent peaks in the velocity integrated maps of different molecular lines and the red star represents the 1.1mm continuum peak obtained from Svoboda et al. (2016). The beam sizes for H^{13}CO^+ , $\text{DCO}^+ J=1-0$ and $\text{DCO}^+ J=2-1$ of $\sim 28''$, $\sim 34''$, and $\sim 16''$ are shown as red circles at the bottom-left corners in their integrated intensity maps. The averaged spectra for column density estimation are derived in the regions enclosed by blue squares.

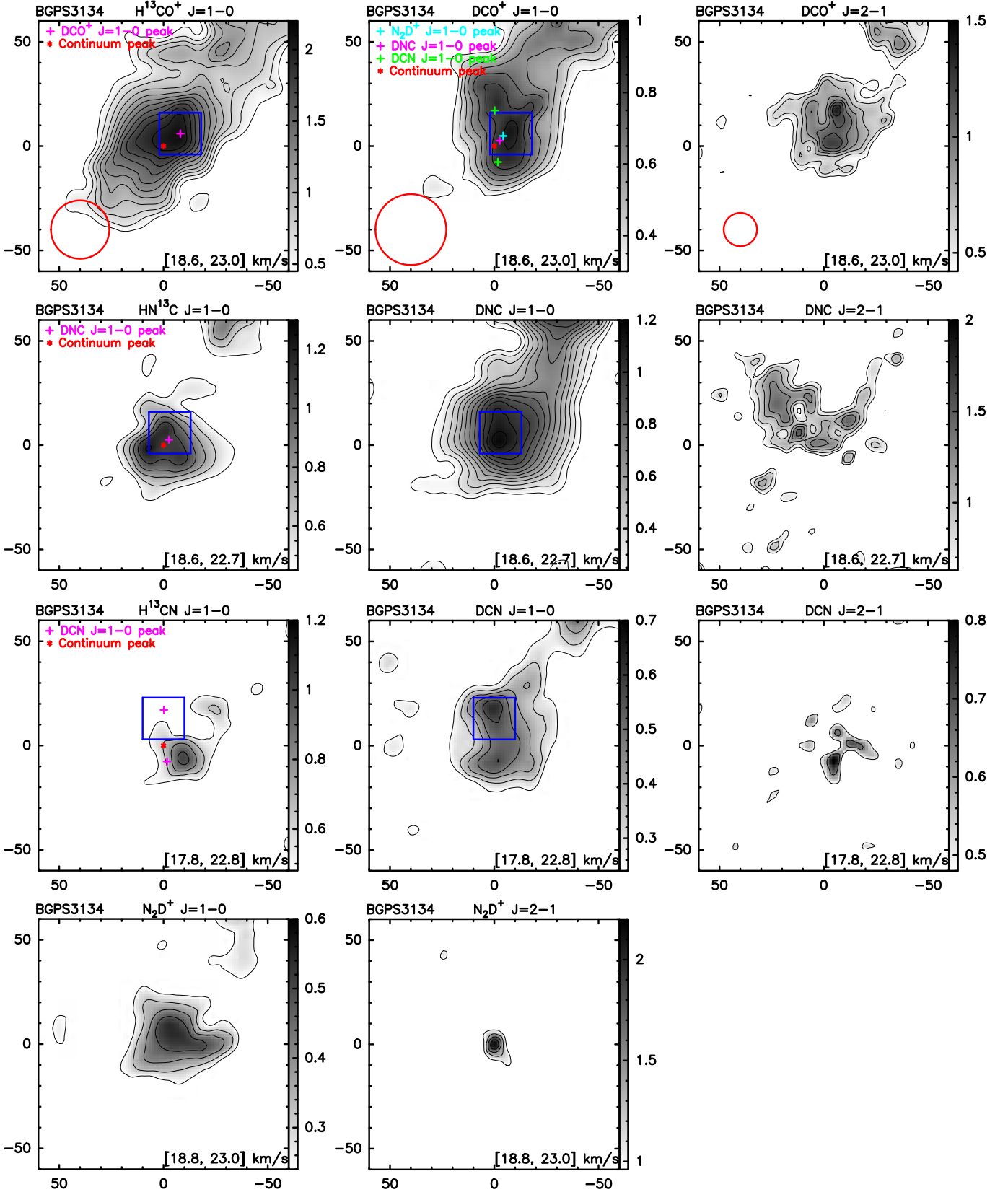


Figure 19. The velocity integrated maps of deuterated and ^{13}C -isotopic molecular lines for BGPS3134. The integrated velocity range, shown at the right-bottom corner, is derived after combining the Gaussian fitting line widths for each pair of deuterated molecular line and ^{13}C -isotopologue. For H^{13}CO^+ , DCO^+ , HN^{13}C , DNC , H^{13}CN , DCN , N_2D^+ $J=1-0$, and DCO^+ , DNC , DCN , N_2D^+ $J=2-1$, the contours start from 3σ in steps of 1σ , with $\sigma = 0.15, 0.10, 0.15, 0.08, 0.16, 0.08, 0.14, 0.21, 0.16$, and 0.32 K km s^{-1} , respectively. The crosses represent peaks in the velocity integrated maps of different molecular lines and the red star represents the 1.1mm continuum peak obtained from Svoboda et al. (2016). The beam sizes for H^{13}CO^+ , DCO^+ $J=1-0$ and DCO^+ $J=2-1$ of $\sim 28''$, $\sim 34''$, and $\sim 16''$ are shown as red circles at the bottom-left corners in their integrated intensity maps. The averaged spectra for column density estimation are derived in the regions enclosed by blue squares.

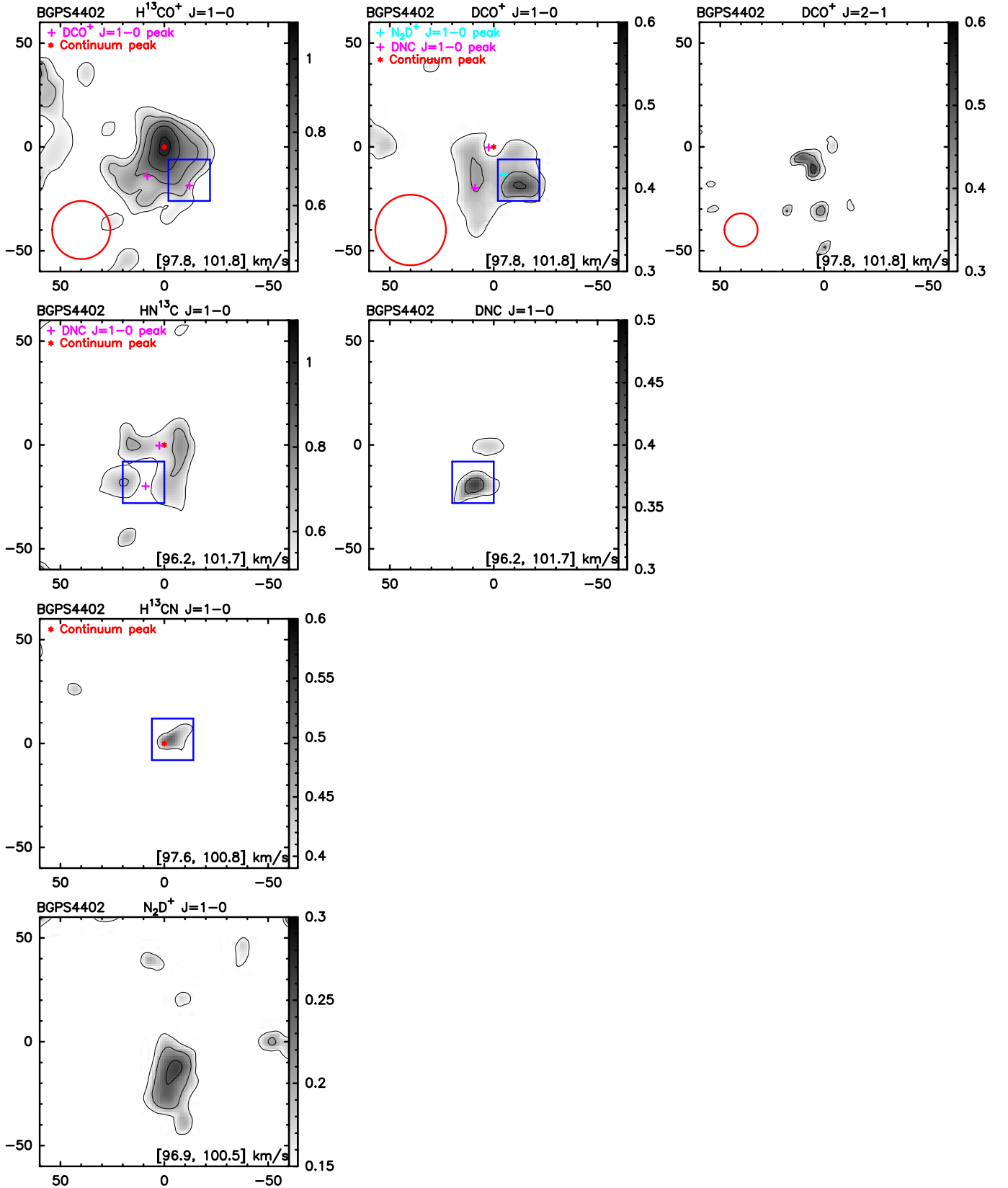


Figure 20. The velocity integrated maps of deuterated and ^{13}C -isotopic molecular lines for BGPS4402. The integrated velocity range, shown at the right-bottom corner, is derived after combining the Gaussian fitting line widths for each pair of deuterated molecular line and ^{13}C -isotopologue. For H^{13}CO^+ , DCO^+ , HN^{13}C , DNC , H^{13}CN , N_2D^+ $J=1-0$, and DCO^+ $J=2-1$, the contours start from 3σ in steps of 1σ , with $\sigma = 0.14, 0.10, 0.17, 0.10, 0.13, 0.05$, and 0.05 K km s^{-1} , respectively. The crosses represent peaks in the velocity integrated maps of different molecular lines and the red star represents the 1.1mm continuum peak obtained from Svoboda et al. (2016). The beam sizes for H^{13}CO^+ , DCO^+ $J=1-0$ and DCO^+ $J=2-1$ of $\sim 28''$, $\sim 34''$, and $\sim 16''$ are shown as red circles at the bottom-left corners in their integrated intensity maps. The averaged spectra for column density estimation are derived in the regions enclosed by blue squares.

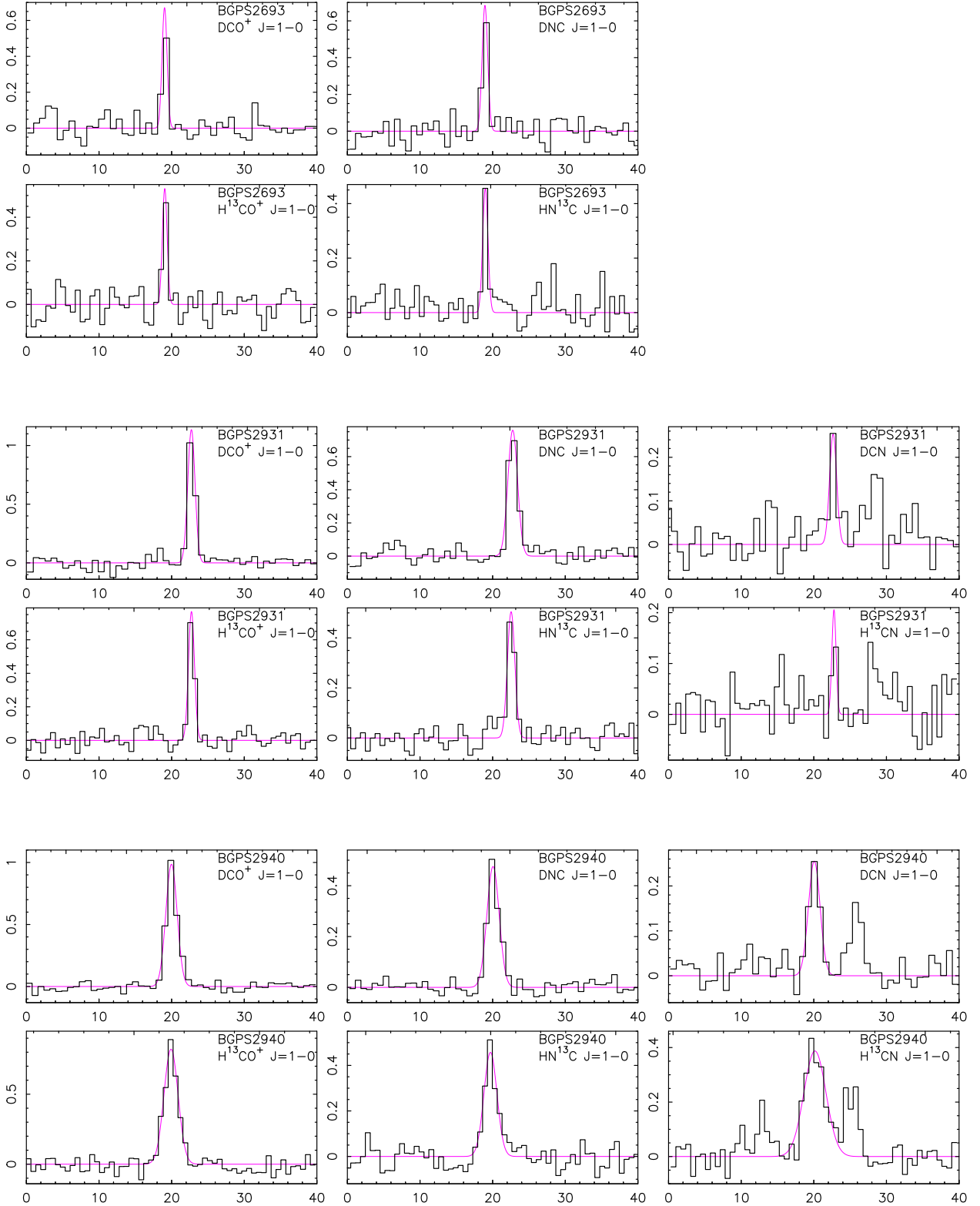


Figure 21. Averaged DCO^+ , H^{13}CO^+ , DNC , HN^{13}C , DCN , and H^{13}CN $J=1-0$ spectra of the 11 OTF sources. These spectra are averaged from the region enclosed by blue squares in Figures 10–20. These regions represent the peak regions of the deuterated molecular lines. The Gaussian fitting result for each spectrum is shown in magenta. The x-axis is velocity in km s^{-1} , and the y-axis is T_{mb} in kelvin.

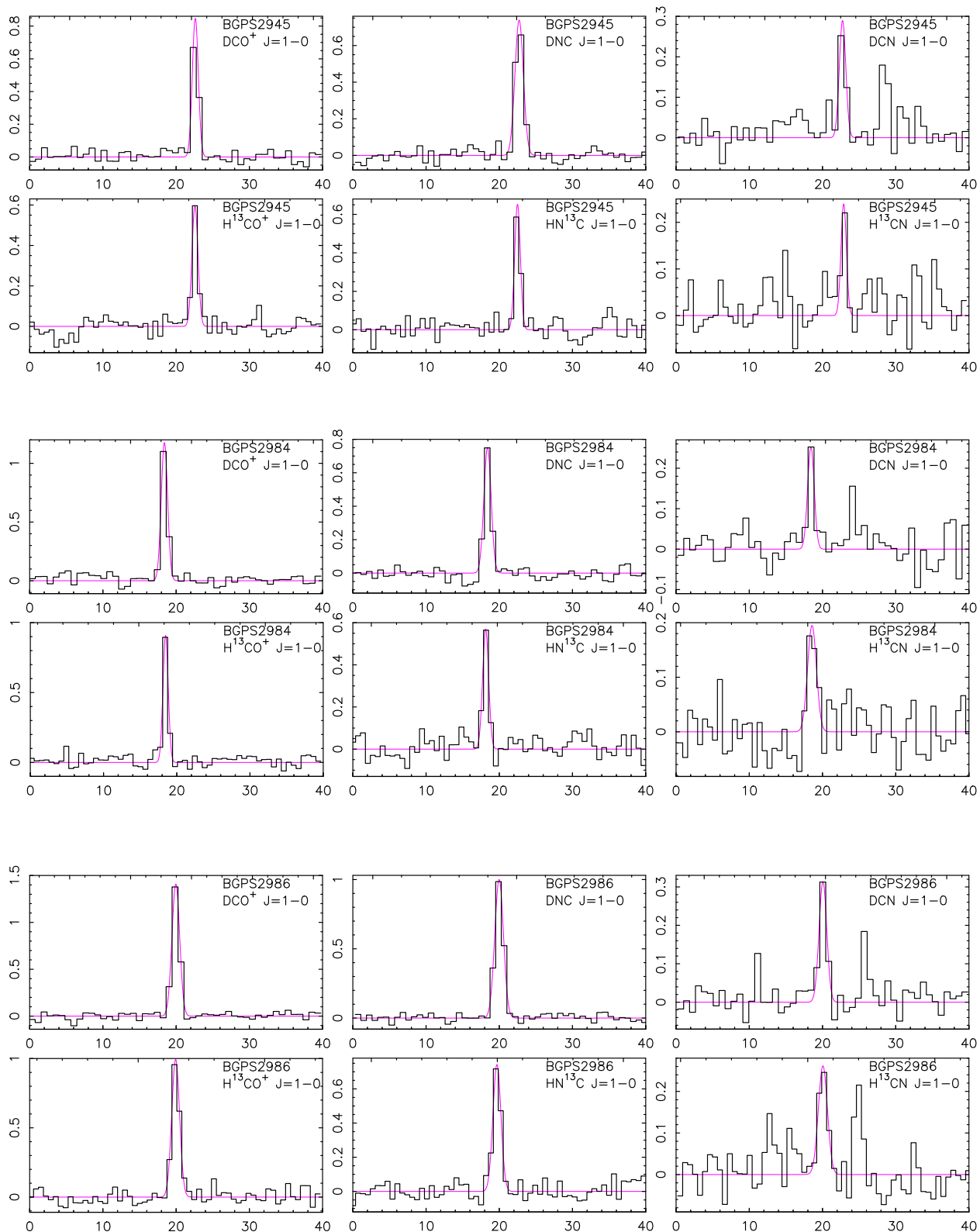


Figure 21. Continued.

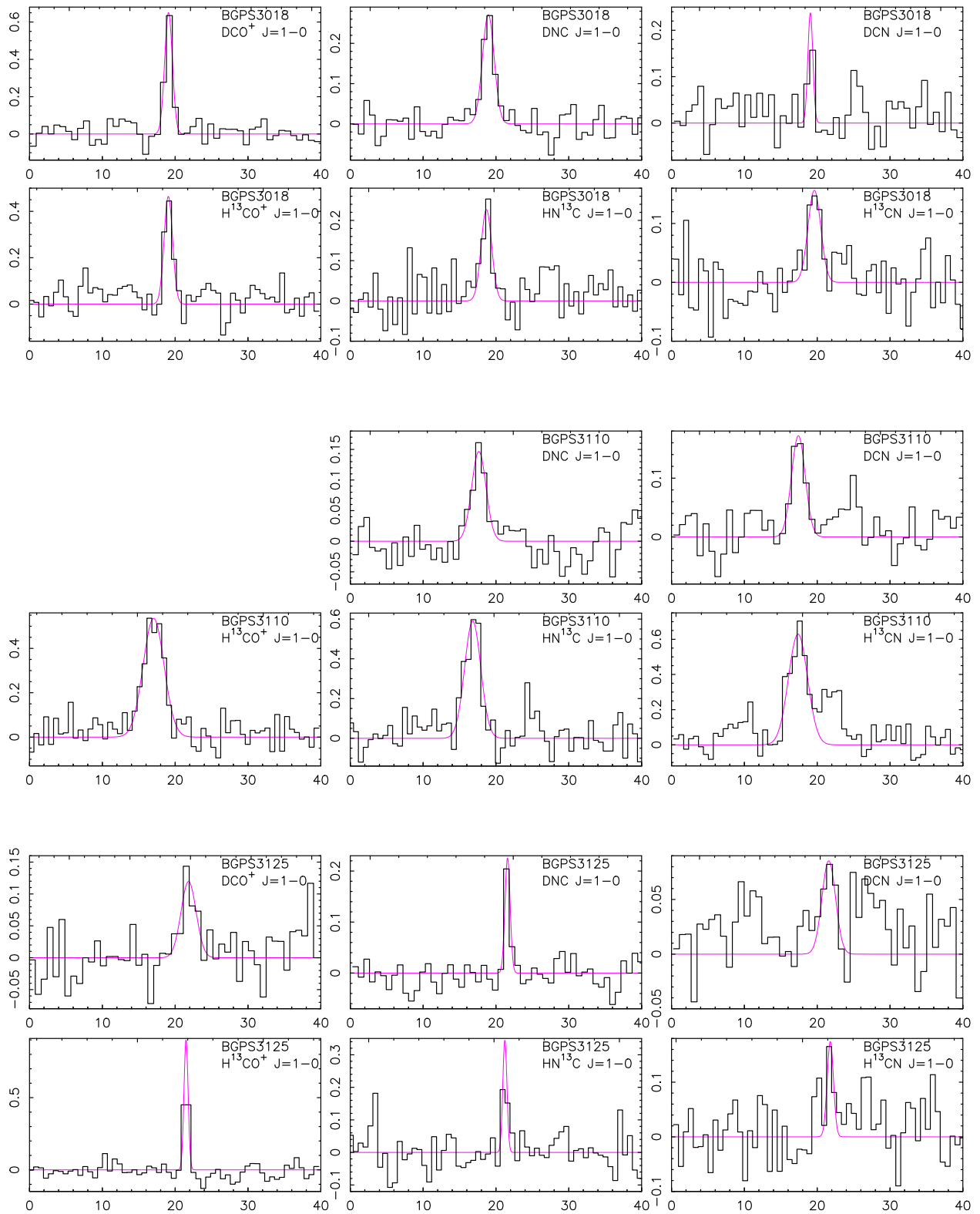


Figure 21. Continued.

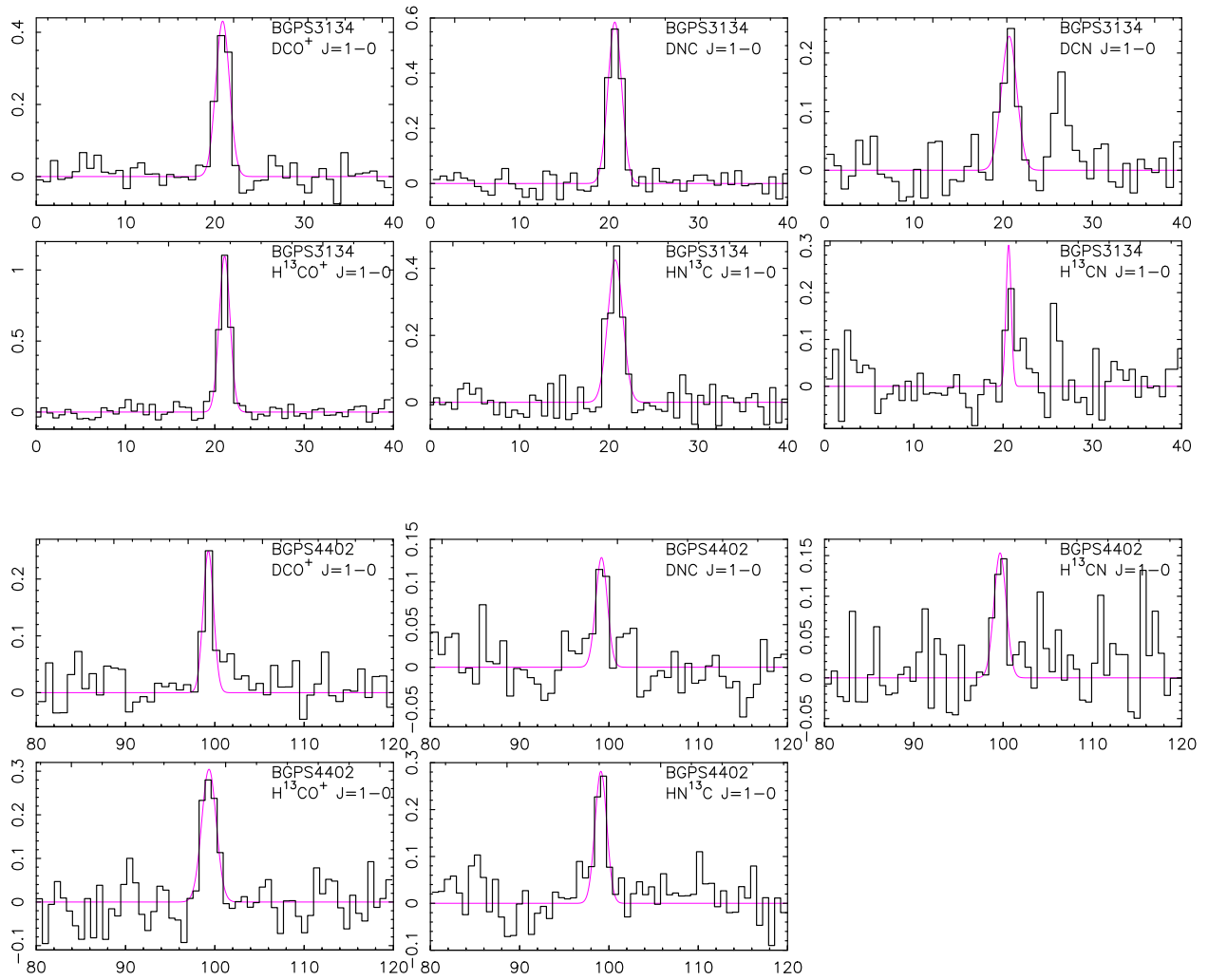


Figure 21. Continued.

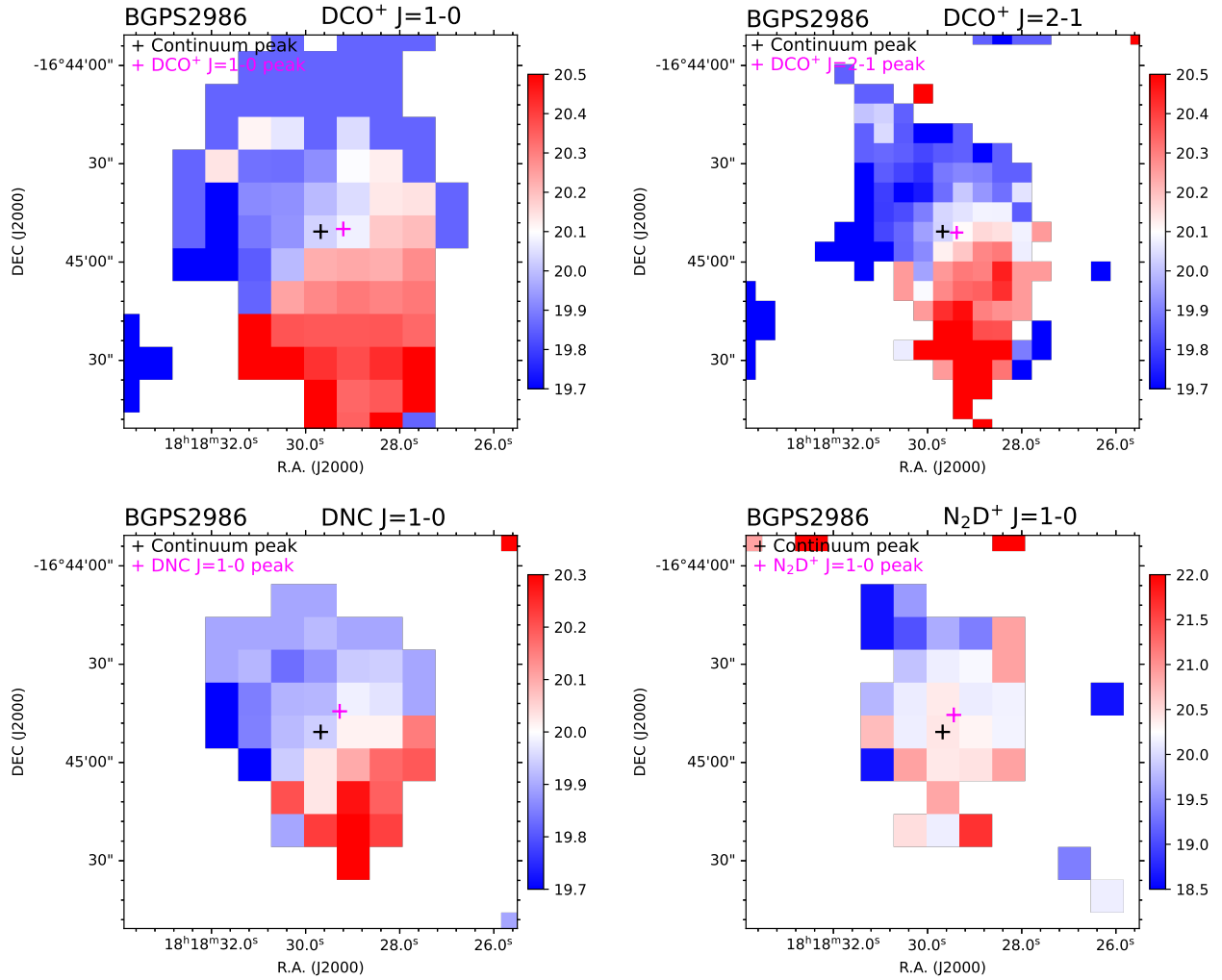


Figure 22. Velocity field of deuterated molecules for BGPS2986. The crosses represent integrated intensity peaks of different lines and 1.1mm continuum peak.

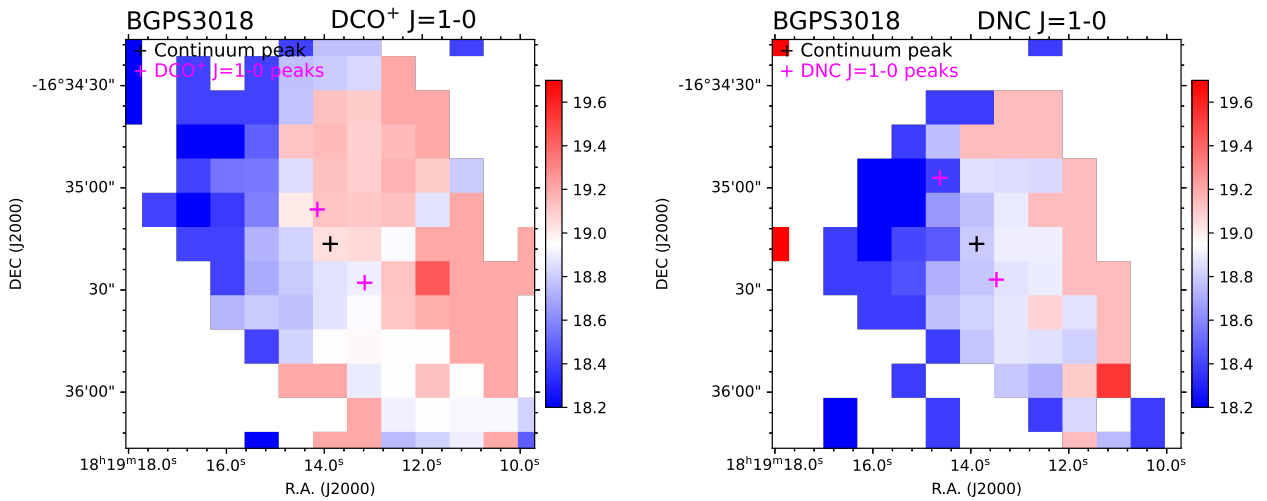


Figure 23. Line width distribution of deuterated molecules for BGPS3018.

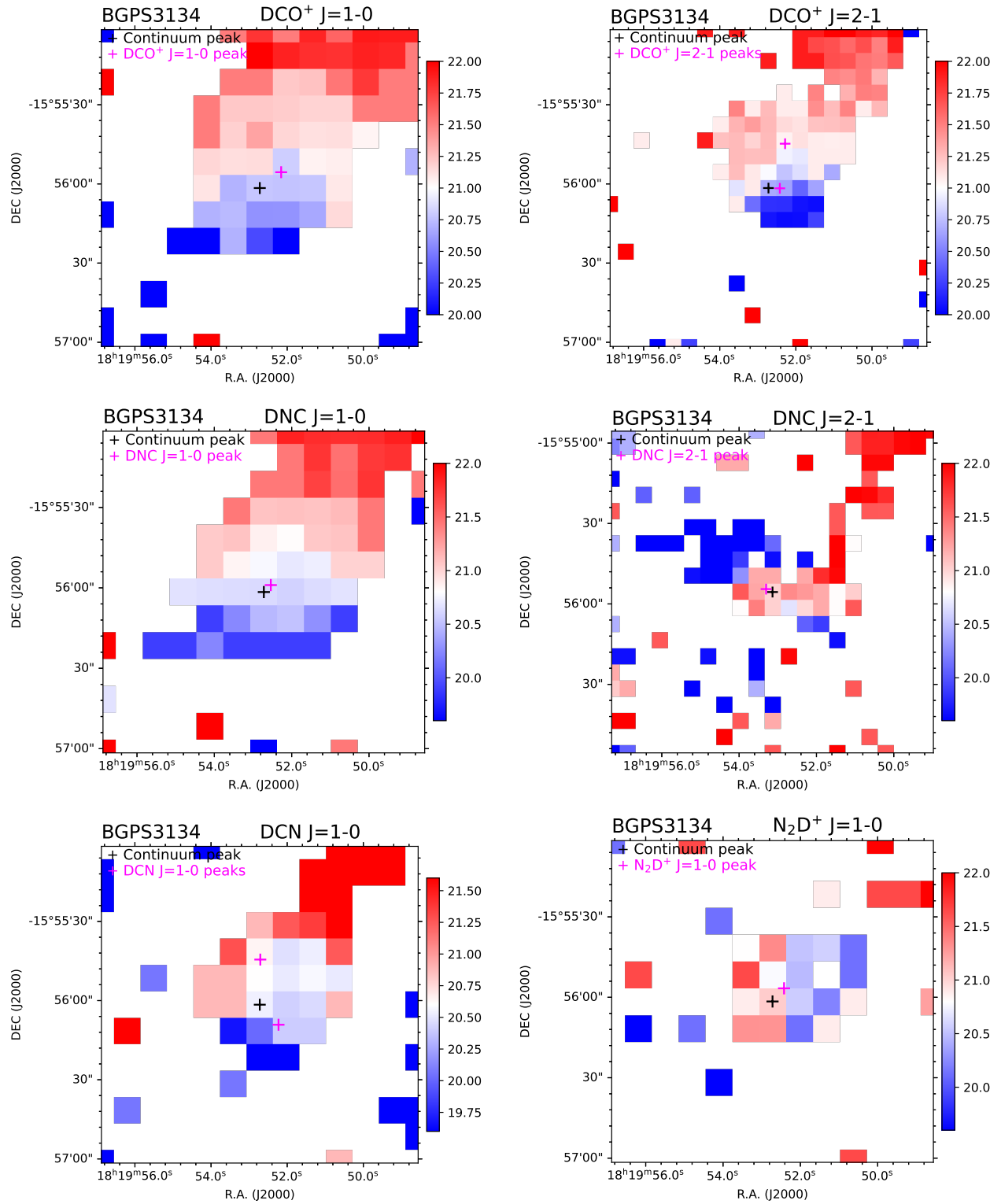


Figure 24. Line width distribution of deuterated molecules for BGPS3134.

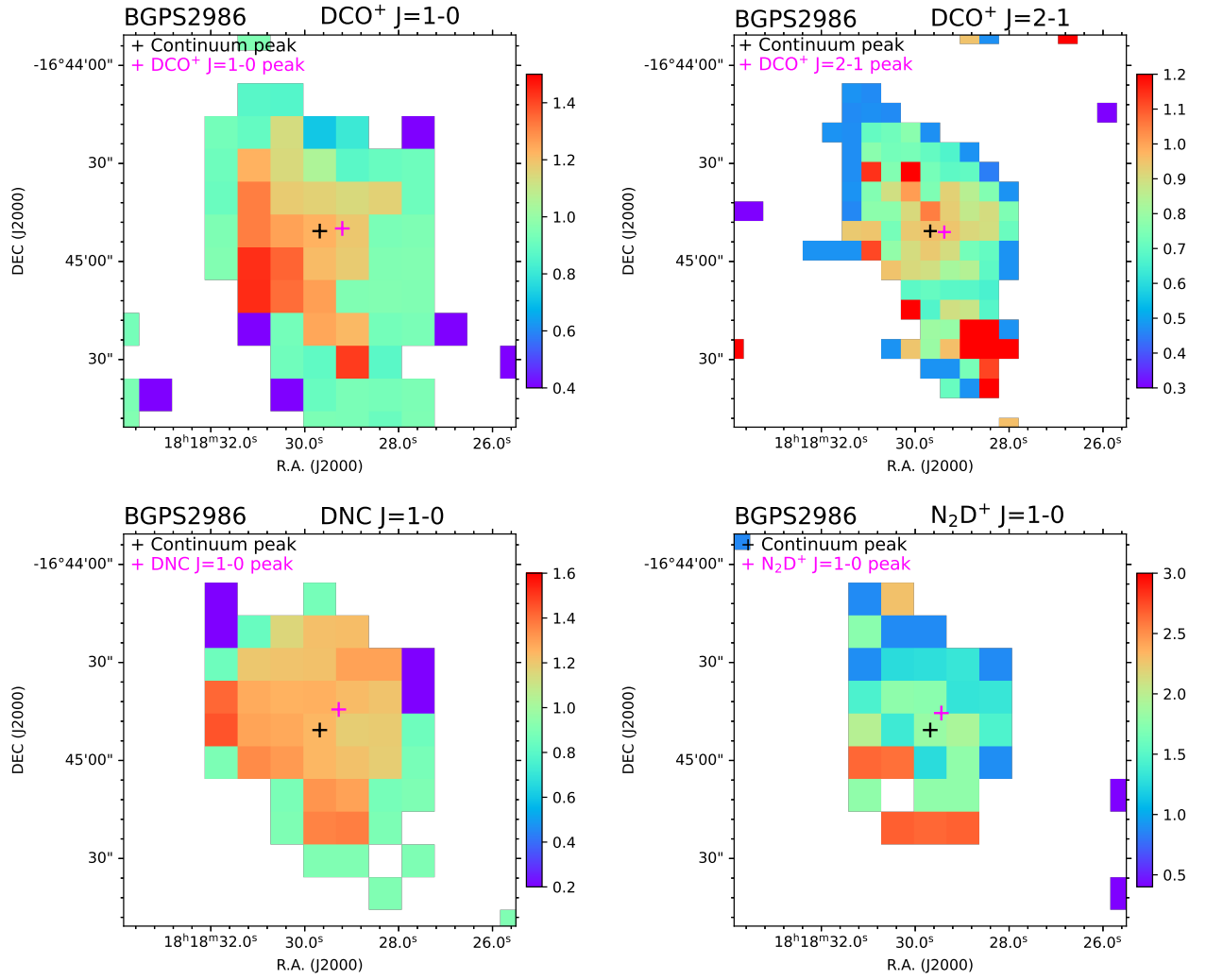


Figure 25. Line width distribution of deuterated molecules for BGPS2986. The crosses represent integrated intensity peaks of different lines and 1.1mm continuum peak.

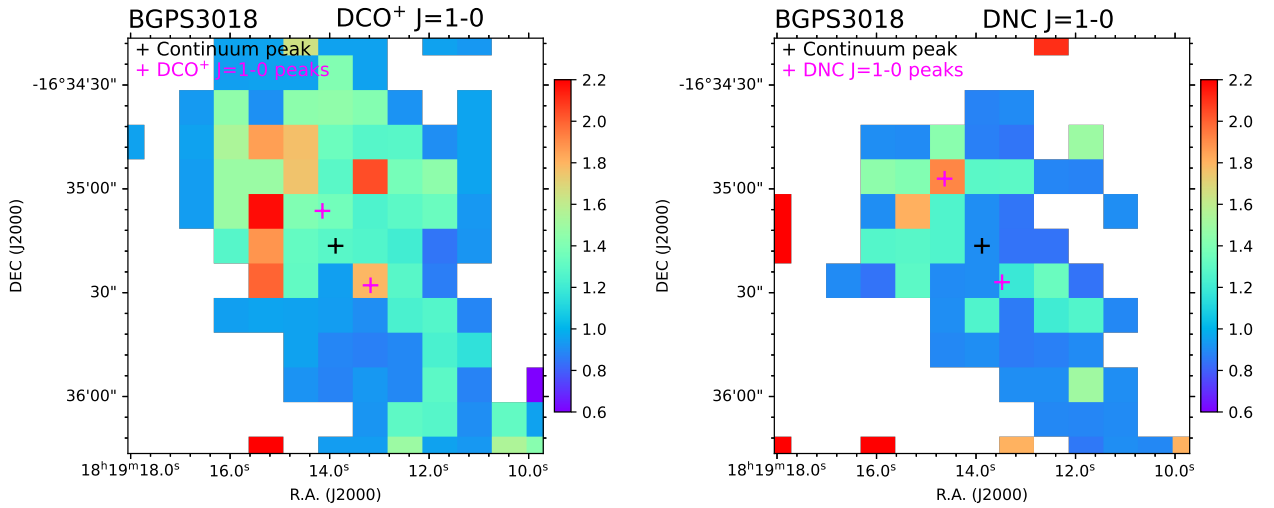


Figure 26. Line width distribution of deuterated molecules for BGPS3018.

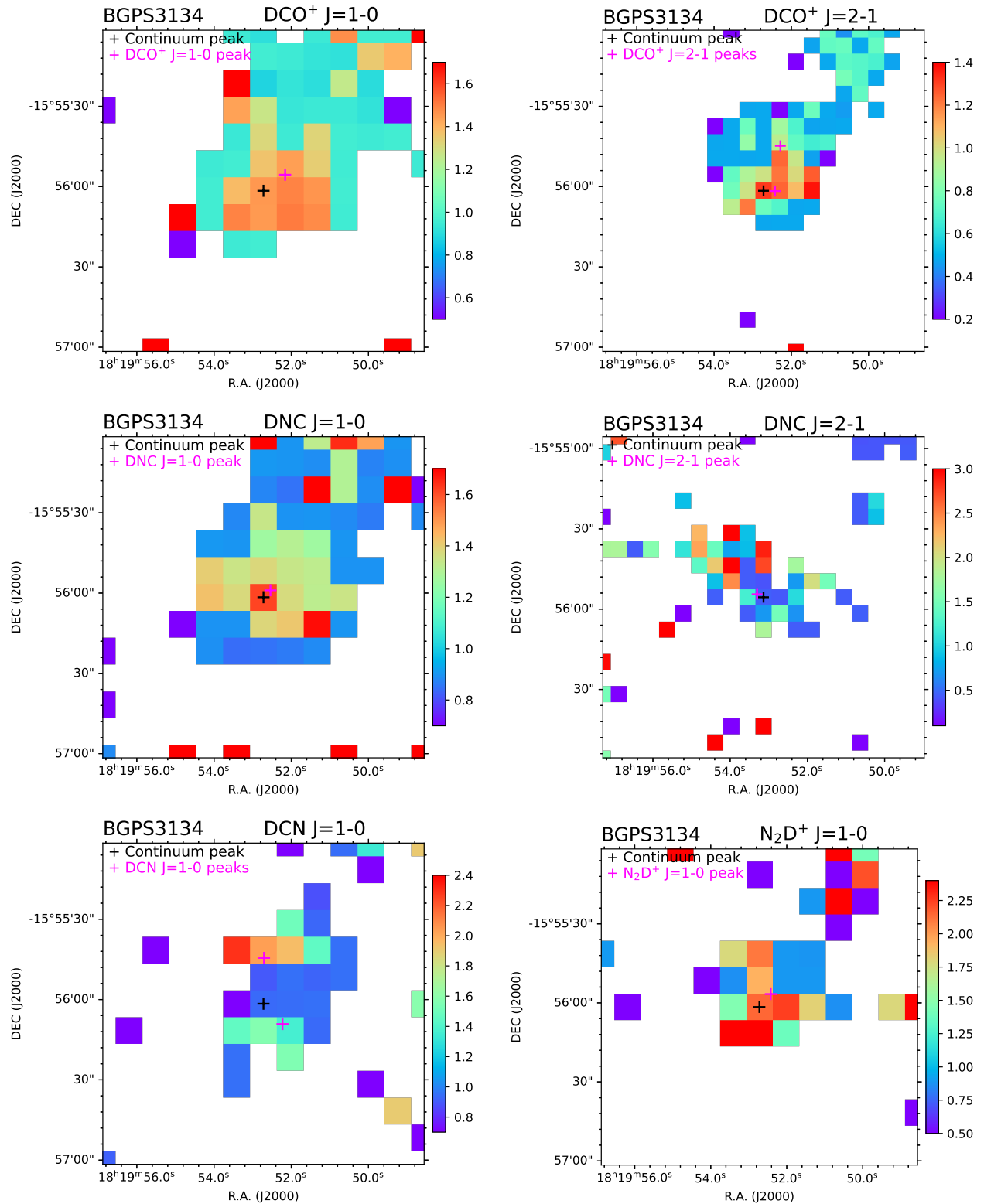


Figure 27. Line width distribution of deuterated molecules for BGPS3134.

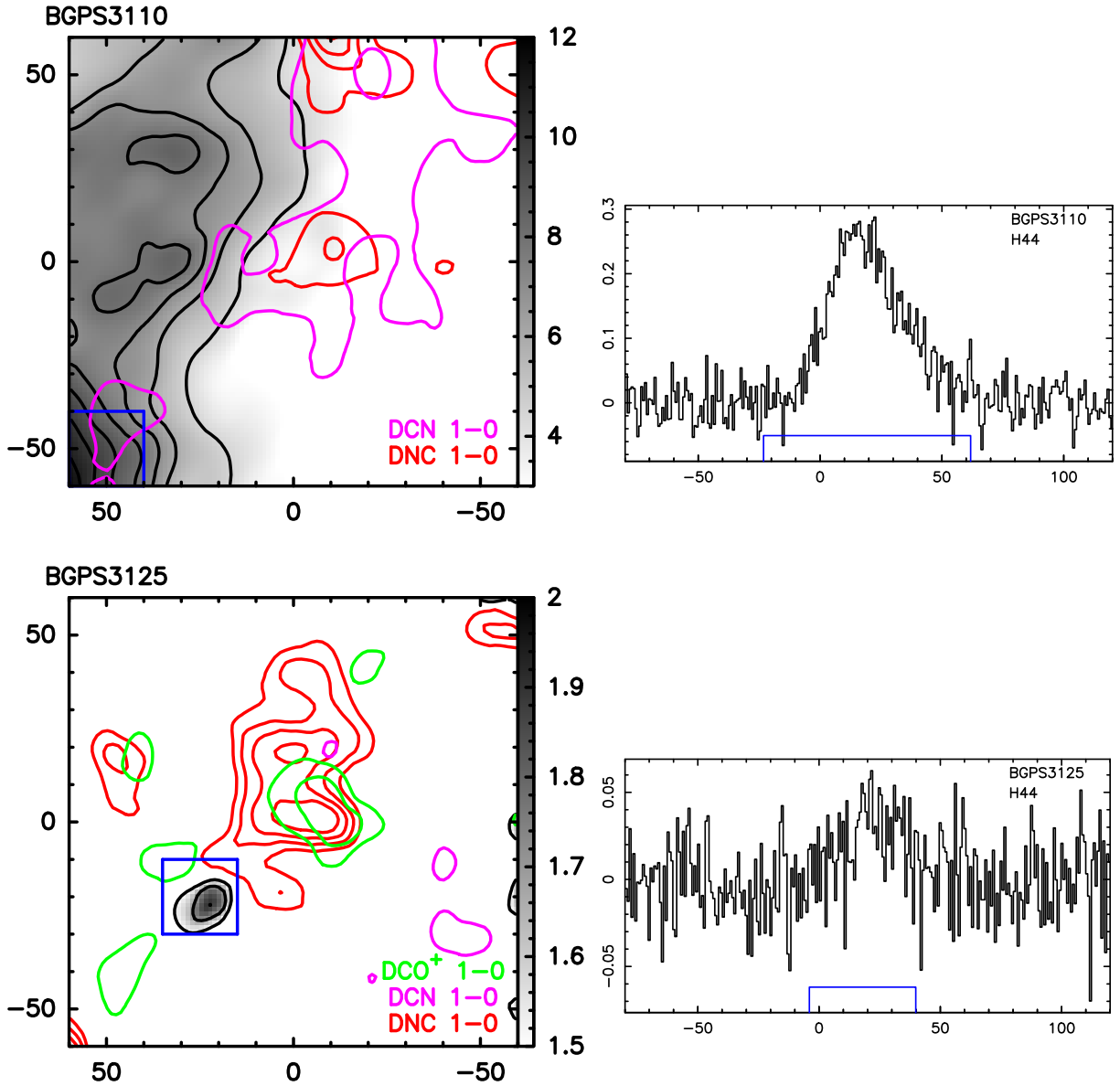


Figure 28. Left: The H44 α (black contours and grey-scale maps) versus deuterated lines (color contours) distributions for BGPS3110 and BGPS3125. Right: The H44 α spectra for BGPS3110 and BGPS3125. The velocity range that we derived the velocity-integrated intensity maps are shown in the spectra with blue lines. The spectra are averaged from the regions enclosed by blue lines in the velocity-integrated intensity maps. The black contours start from 3σ in steps of 1σ , with $\sigma = 1.5$ and 0.2 K km s^{-1} for BGPS3110 and BGPS3125. The color contours of the deuterated lines are the same as those in Figure 17 and 18.

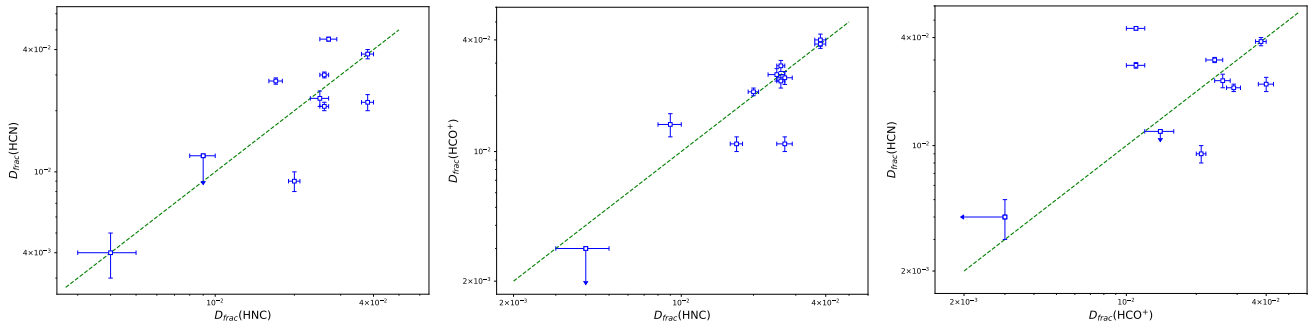


Figure 29. Left: $D_{\text{frac}}(\text{HNC})$ versus $D_{\text{frac}}(\text{HCN})$. Middle: $D_{\text{frac}}(\text{HNC})$ versus $D_{\text{frac}}(\text{HCO}^+)$. Right: $D_{\text{frac}}(\text{HCN})$ versus $D_{\text{frac}}(\text{HCO}^+)$. The arrows show the upper limits of the estimated deuteration fractions. The green dashed lines represent $x = y$.

APPENDIX

A. INTEGRATED MAPS OF HCO^+ , HCN , HNC , AND N_2H^+ $J=1-0$

In this section, we present the HCO^+ , HCN , HNC , and N_2H^+ $J=1-0$ integrated maps for each source in the OTF observations in Figures 30–40.

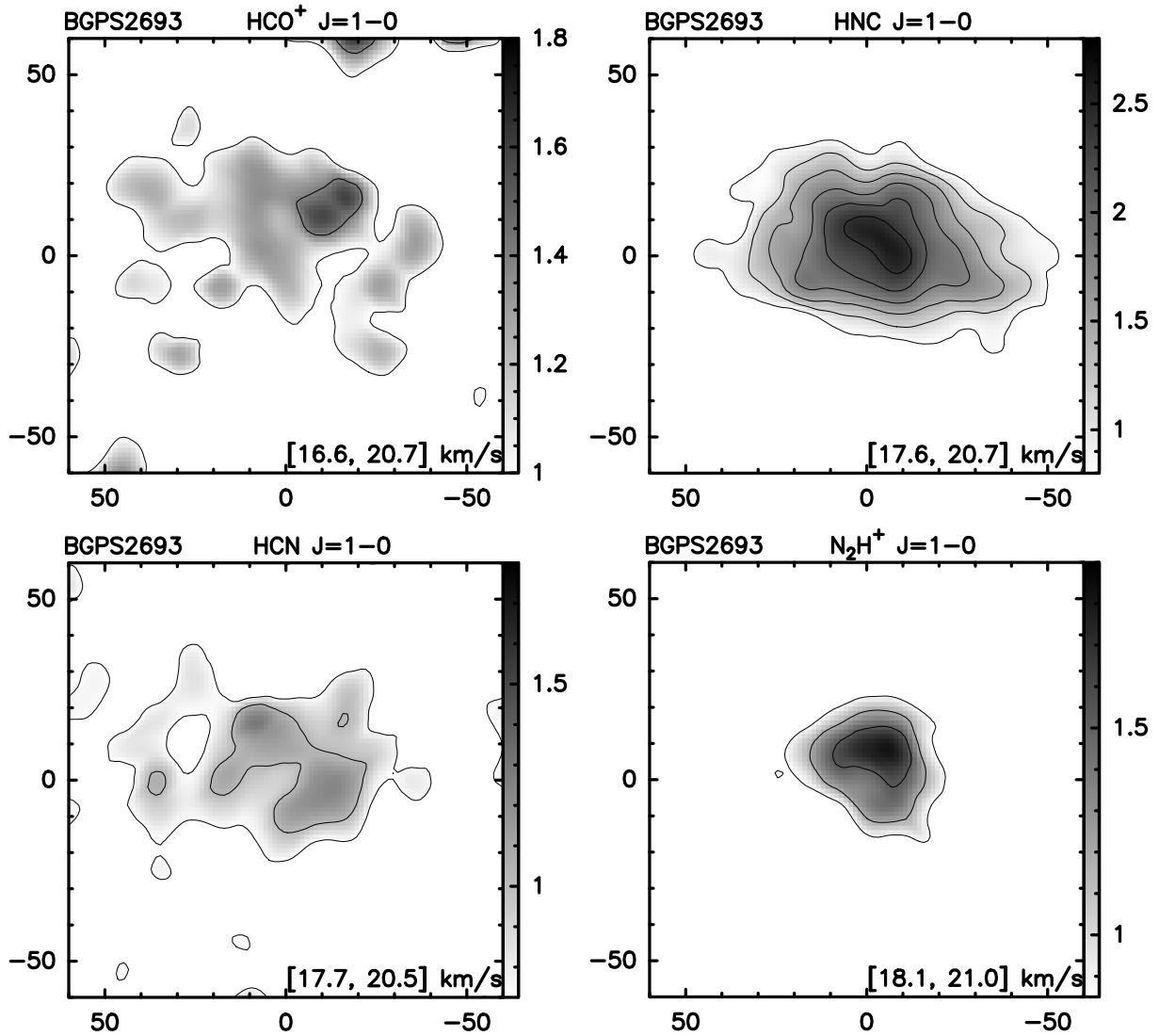


Figure 30. HCO⁺, HCN, HNC, and N₂H⁺ $J=1-0$ integrated maps of BGPS2693. The integrated velocity range is shown at the right-bottom corner. For HCO⁺, HCN, HNC, and N₂H⁺ $J=1-0$, the contours start from 5σ in steps of 2σ , with $\sigma = 0.20$, 0.15 , 0.16 , and 0.17 K km s⁻¹.

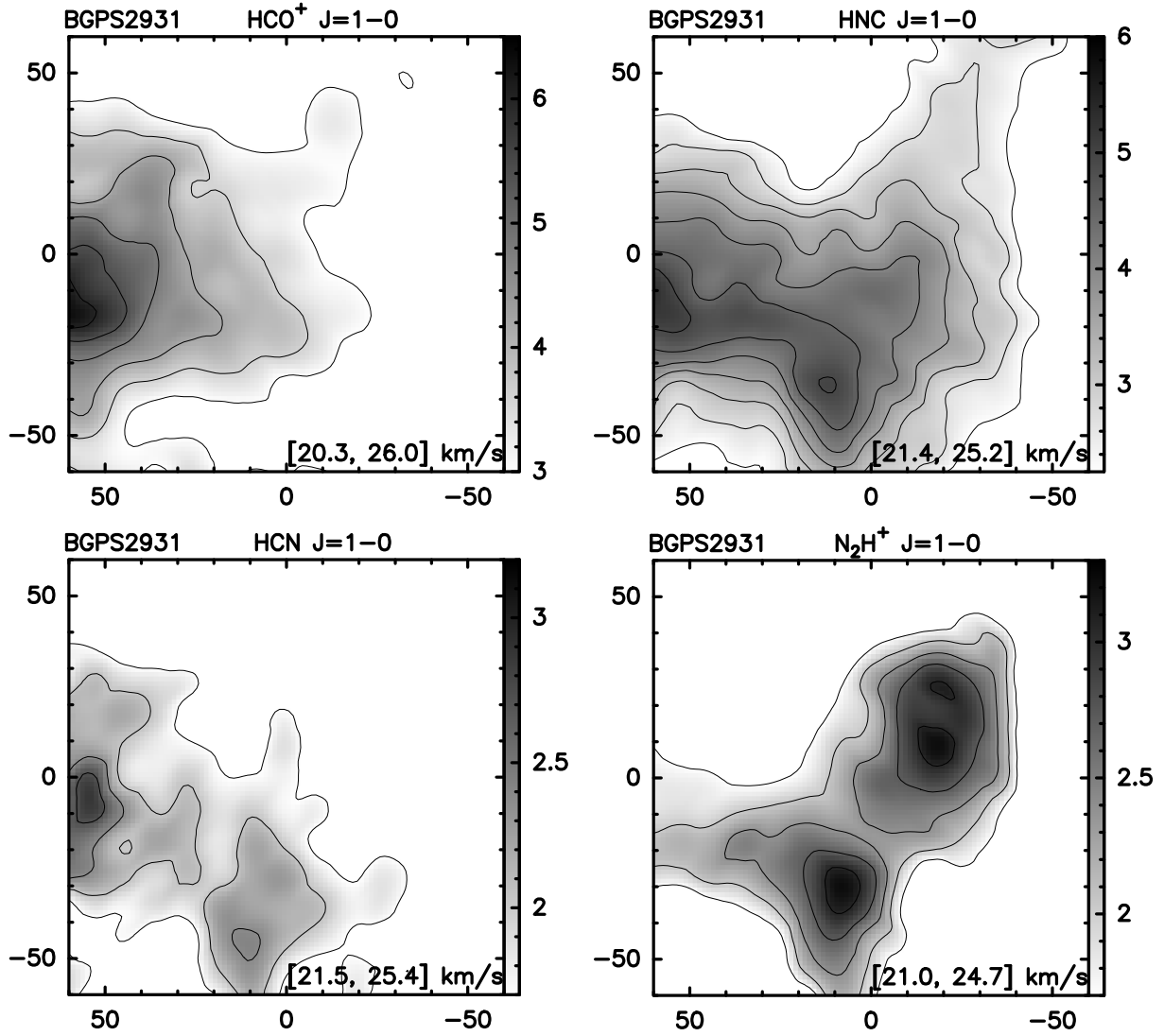


Figure 31. HCO⁺, HCN, HNC, and N₂H⁺ $J=1-0$ integrated maps of BGPS2931. The integrated velocity range is shown at the right-bottom corner. For HCO⁺ and HNC $J=1-0$, the contours start from 15σ in steps of 3σ , with $\sigma = 0.20$ and 0.15 K km s⁻¹. For HCN and N₂H⁺ $J=1-0$, the contours start from 10σ in steps of 2σ , with $\sigma = 0.17$ and 0.17 K km s⁻¹.

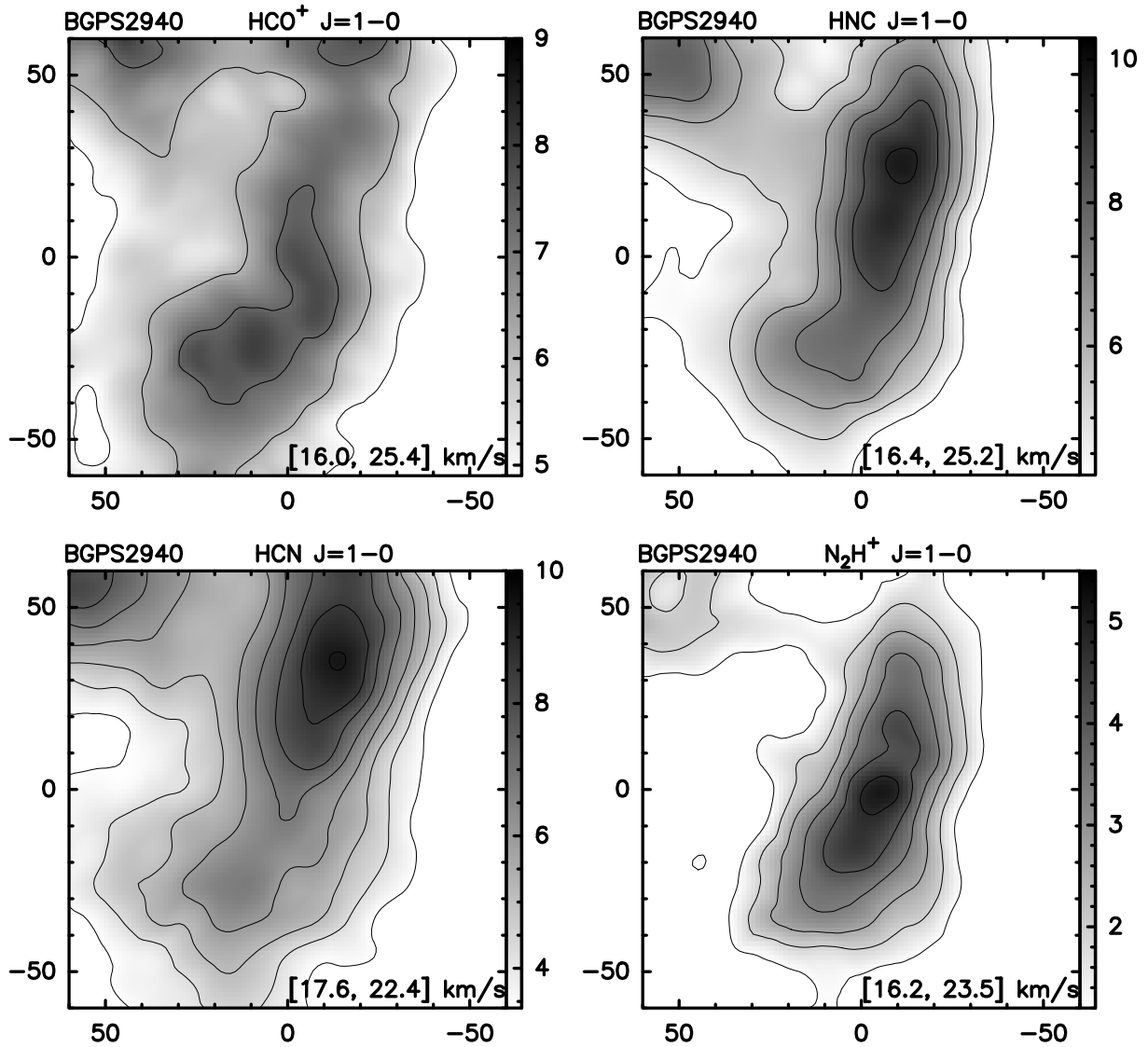


Figure 32. HCO^+ , HCN , HNC , and $\text{N}_2\text{H}^+ J=1-0$ integrated maps of BGPS2940. The integrated velocity range is shown at the right-bottom corner. For HCO^+ , HCN , and $\text{HNC } J=1-0$, the contours start from 20σ in steps of 5σ , with $\sigma = 0.25$, 0.17 , and 0.21 K km s^{-1} . For $\text{N}_2\text{H}^+ J=1-0$, the contours start from 5σ in steps of 3σ , with $\sigma = 0.24 \text{ K km s}^{-1}$.

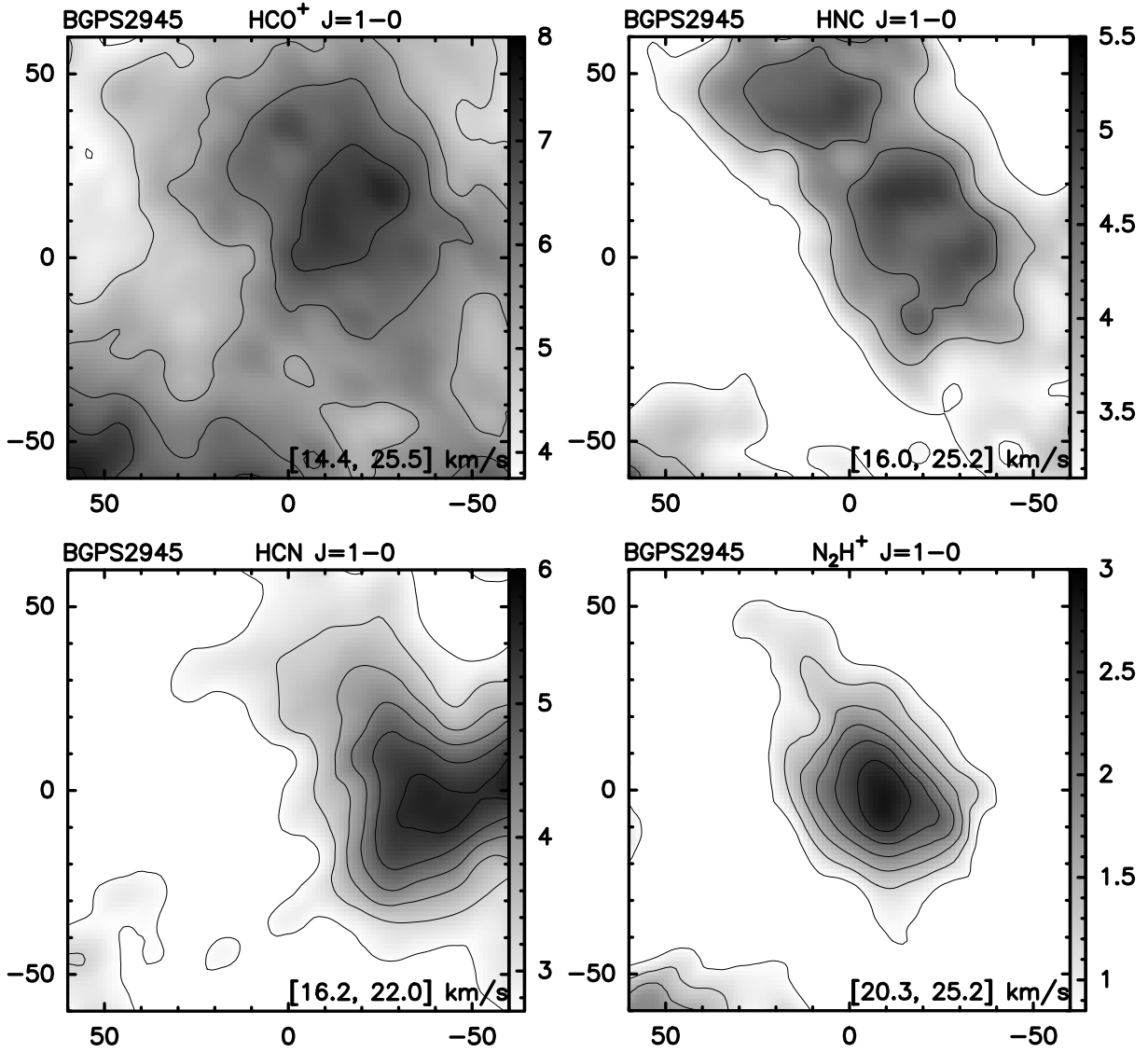


Figure 33. HCO^+ , HCN , HNC , and N_2H^+ $J=1-0$ integrated maps of BGPS2945. The integrated velocity range is shown at the right-bottom corner. For HCO^+ , HCN , and HNC $J=1-0$, the contours start from 15σ in steps of 3σ , with $\sigma = 0.25$, 0.18 , and 0.21 K km s $^{-1}$. For N_2H^+ $J=1-0$, the contours start from 5σ in steps of 2σ , with $\sigma = 0.17$ K km s $^{-1}$.

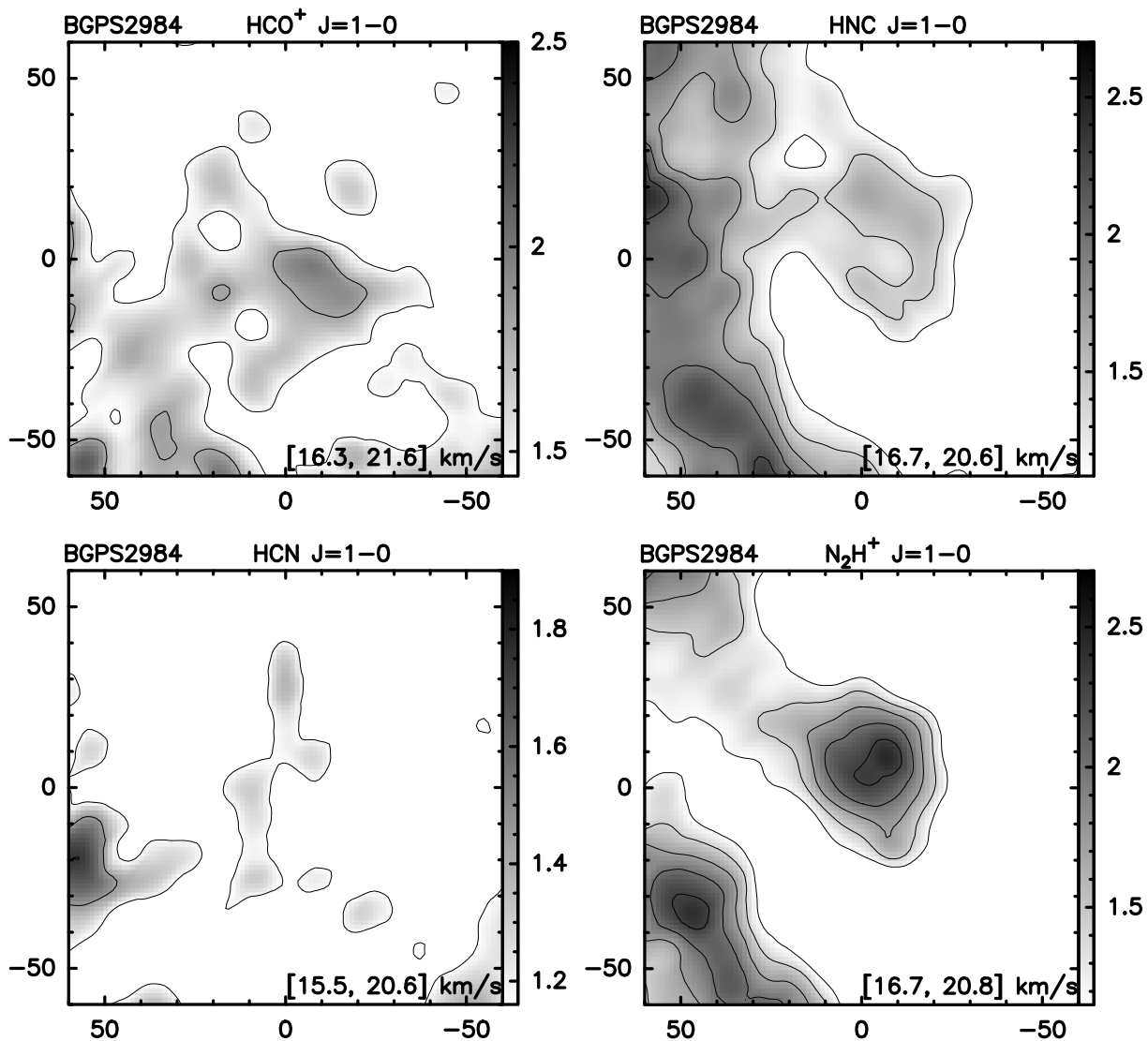


Figure 34. HCO^+ , HCN, HNC, and N_2H^+ $J=1-0$ integrated maps of BGPS2984. The integrated velocity range is shown at the right-bottom corner. For HCO^+ , HCN, HNC, and N_2H^+ $J=1-0$, the contours start from 8σ in steps of 2σ , with $\sigma = 0.18$, 0.17, 0.14, and 0.15 K km s^{-1} .

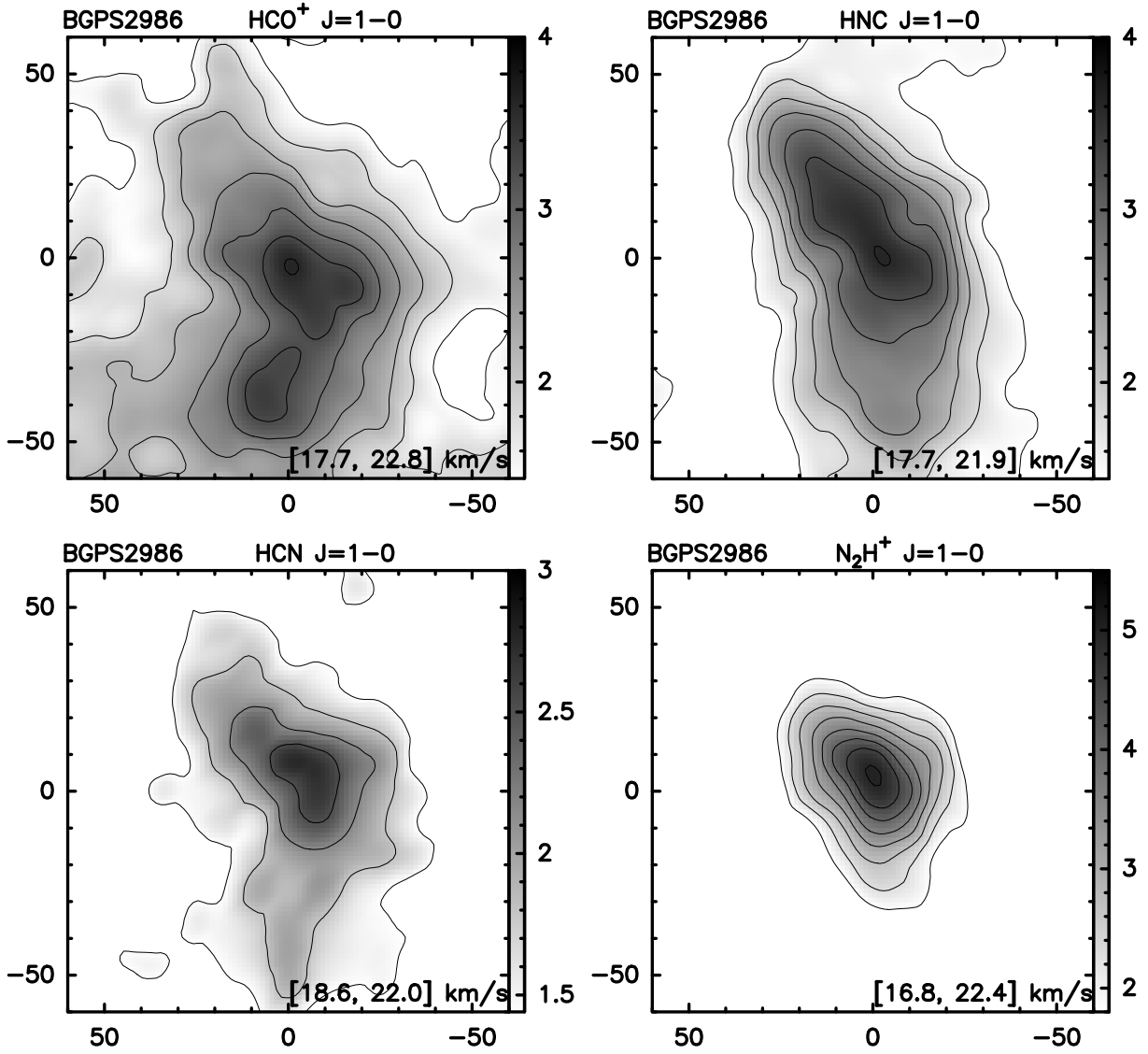


Figure 35. HCO^+ , HCN , HNC , and $\text{N}_2\text{H}^+ J=1-0$ integrated maps of BGPS2986. The integrated velocity range is shown at the right-bottom corner. For HCO^+ , HCN , HNC , and $\text{N}_2\text{H}^+ J=1-0$, the contours start from 12σ in steps of 3σ , with $\sigma = 0.12$, 0.12 , 0.12 , and 0.15 K km s^{-1} .

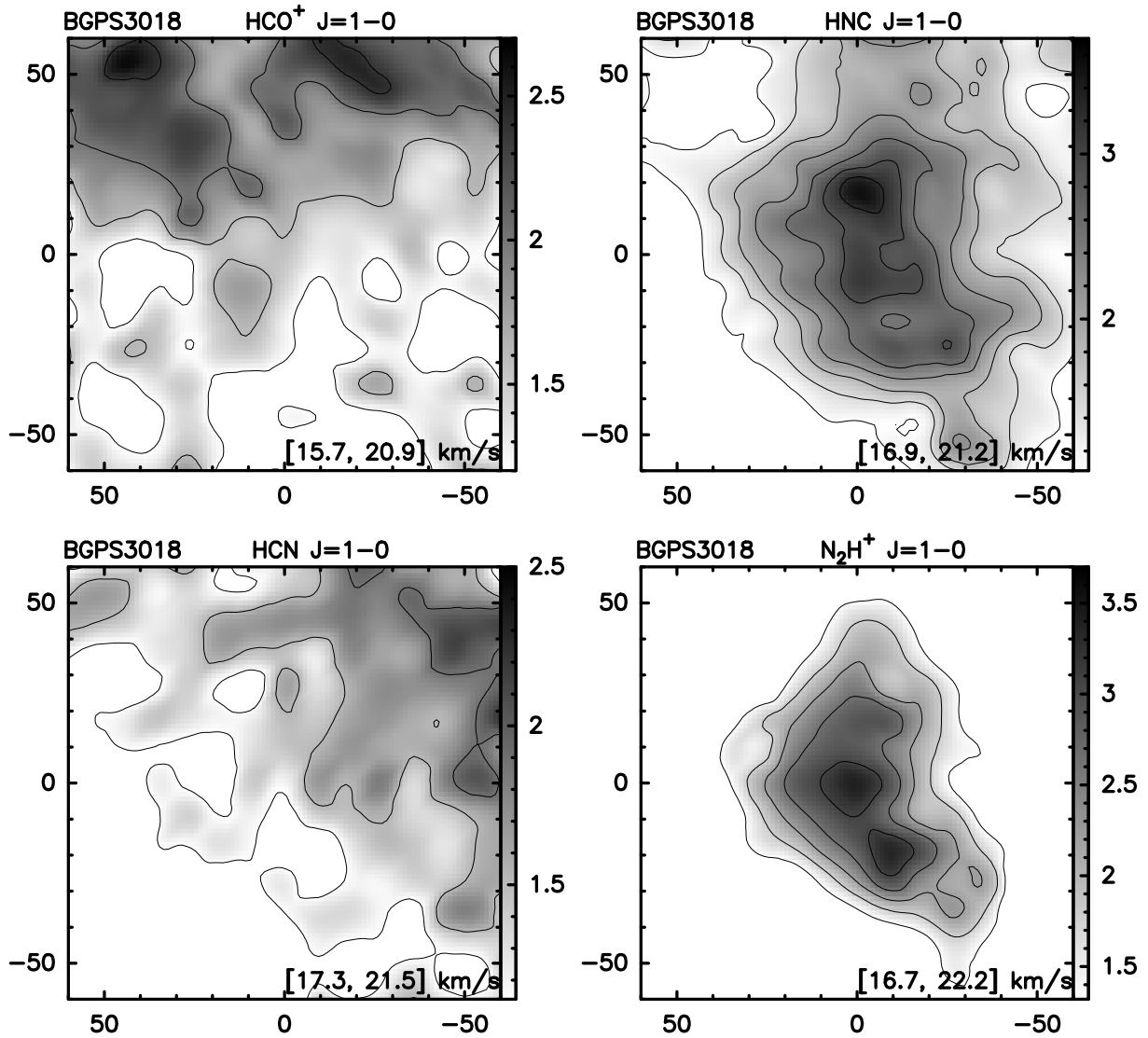


Figure 36. HCO⁺, HCN, HNC, and N₂H⁺ $J=1-0$ integrated maps of BGPS3018. The integrated velocity range is shown at the right-bottom corner. For HCO⁺, HCN, HNC, and N₂H⁺ $J=1-0$, the contours start from 6σ in steps of 2σ , with $\sigma = 0.20$, 0.19 , 0.18 , and 0.22 K km s⁻¹.

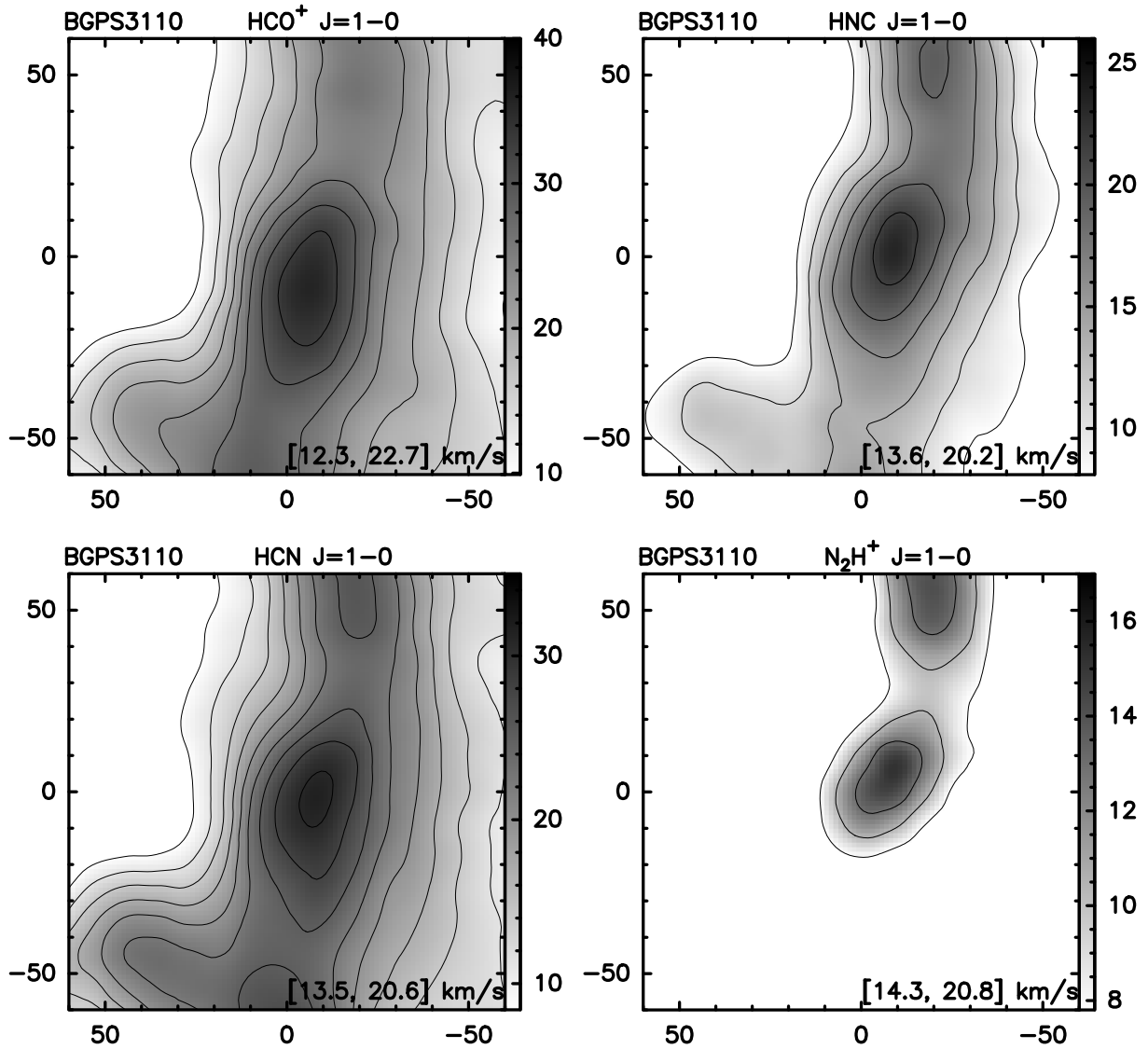


Figure 37. HCO^+ , HCN , HNC , and N_2H^+ $J=1-0$ integrated maps of BGPS3110. The integrated velocity range is shown at the right-bottom corner. For HCO^+ , HCN , HNC , and N_2H^+ $J=1-0$, the contours start from 30σ in steps of 10σ , with $\sigma = 0.33, 0.28, 0.27,$ and 0.26 K km s^{-1} .

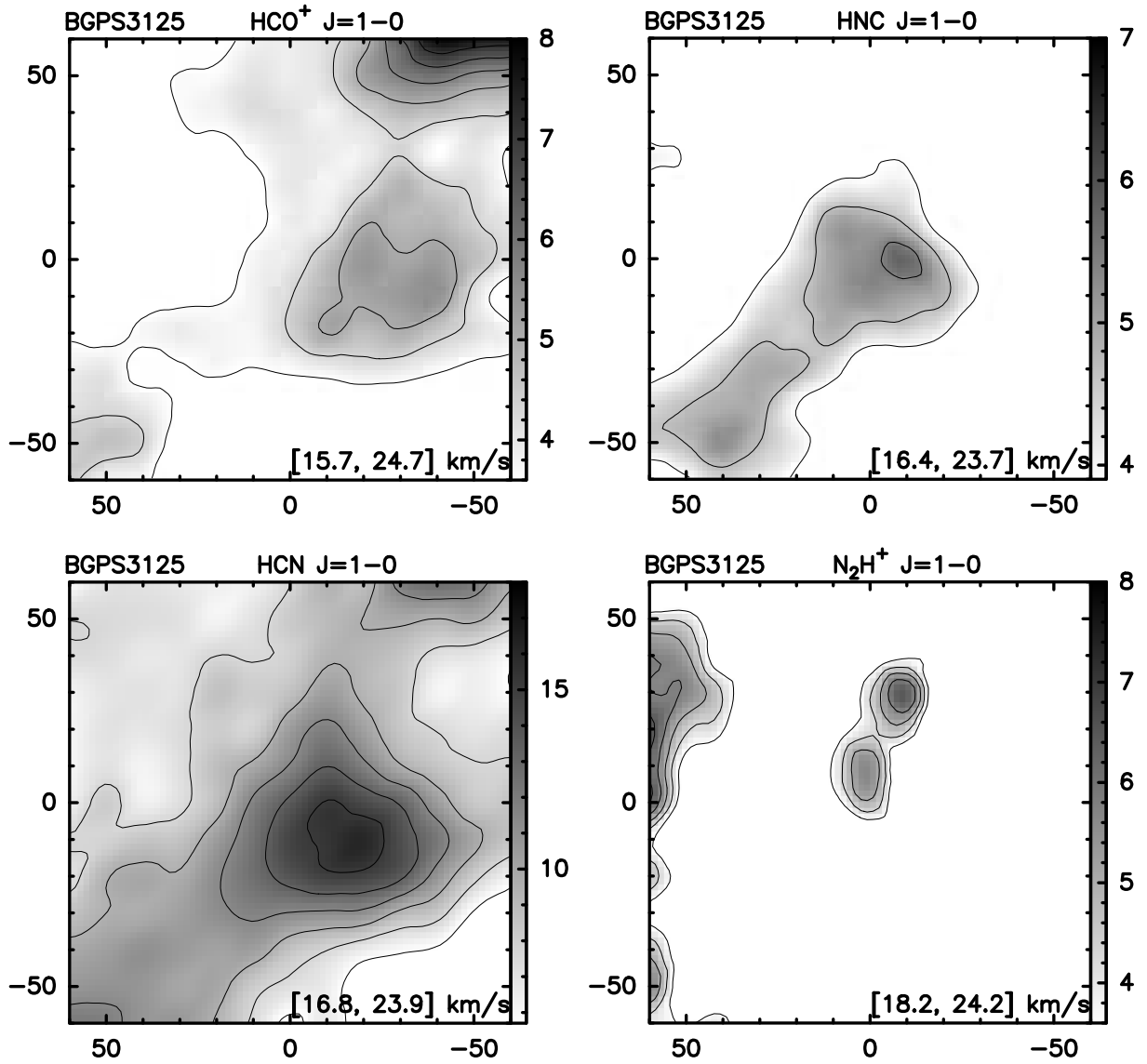


Figure 38. HCO^+ , HCN , HNC , and N_2H^+ $J=1-0$ integrated maps of BGPS3125. The integrated velocity range is shown at the right-bottom corner. For HCO^+ , HNC , and N_2H^+ $J=1-0$, the contours start from 15σ in steps of 3σ , with $\sigma = 0.24$, 0.26 , and 0.24 K km s^{-1} . For $\text{HCN } J=1-0$, the contours start from 30σ in steps of 10σ , with $\sigma = 0.19 \text{ K km s}^{-1}$.

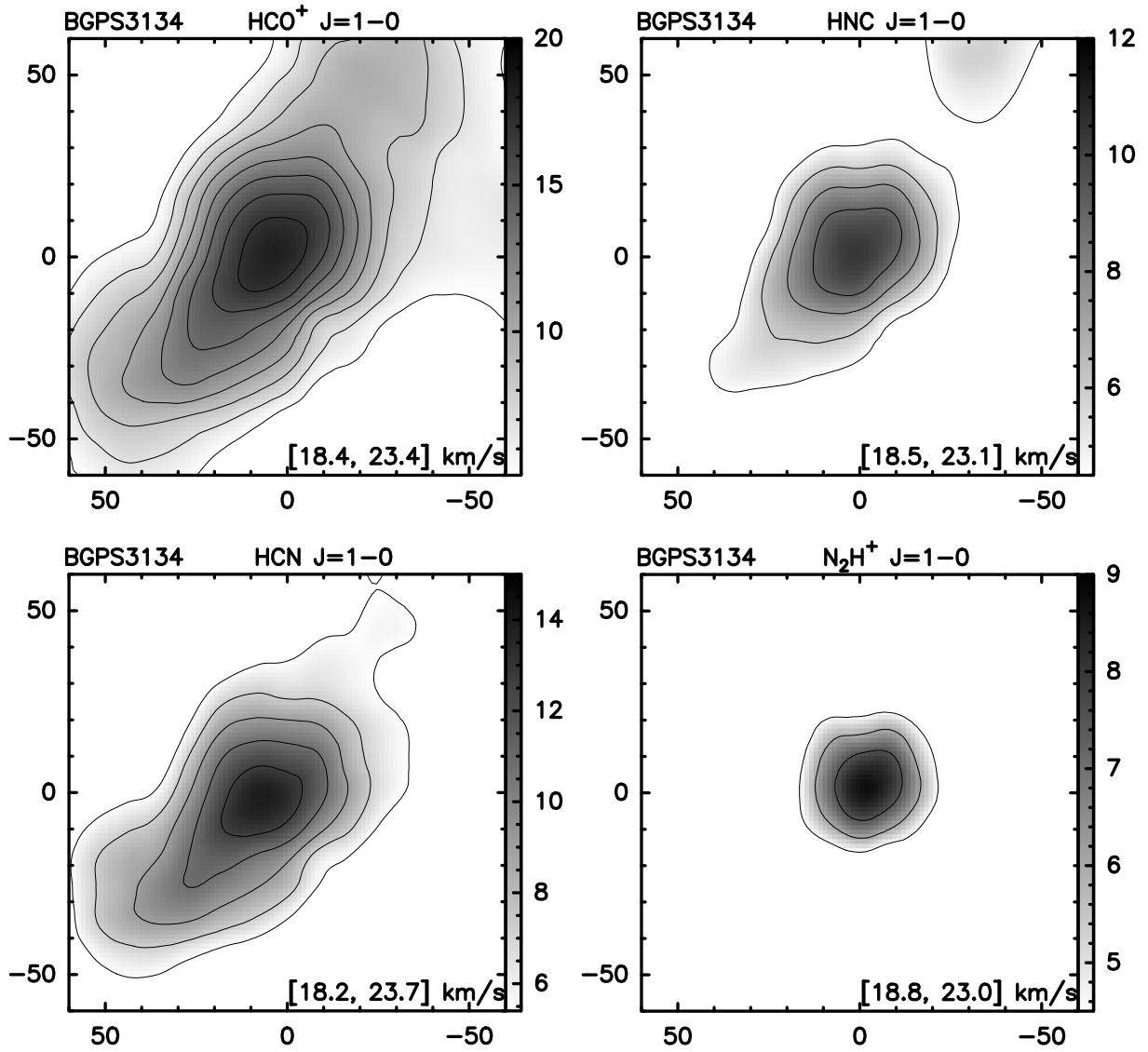


Figure 39. HCO⁺, HCN, HNC, and N₂H⁺ $J=1-0$ integrated maps of BGPS3134. The integrated velocity range is shown at the right-bottom corner. For HCO⁺, HCN, HNC, and N₂H⁺ $J=1-0$, the contours start from 30σ in steps of 10σ , with $\sigma = 0.17, 0.18, 0.15,$ and 0.15 K km s⁻¹.

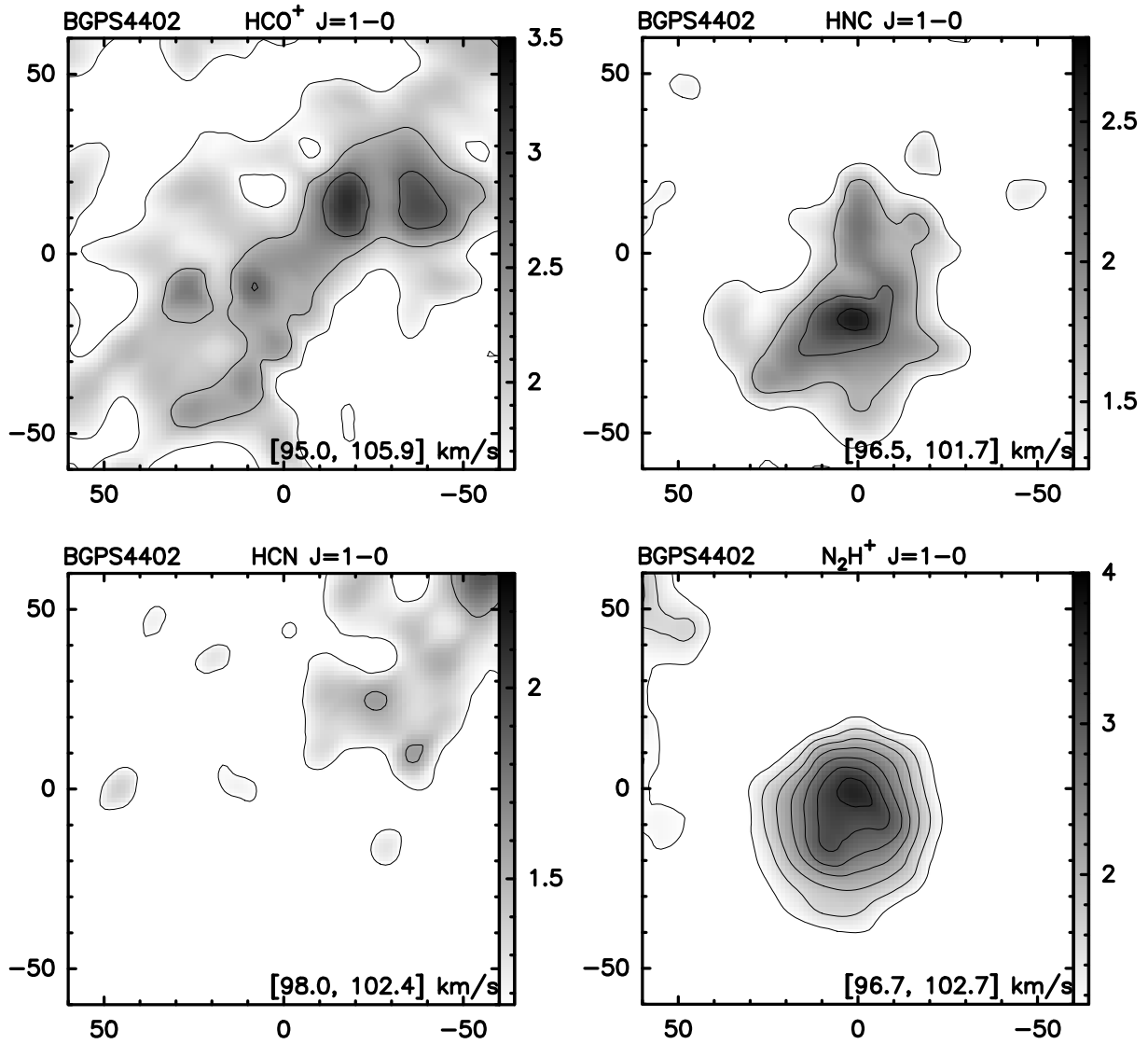


Figure 40. HCO^+ , HCN, HNC, and N_2H^+ $J=1-0$ integrated maps of BGPS4402. The integrated velocity range is shown at the right-bottom corner. For HCO^+ , HCN, HNC, and N_2H^+ $J=1-0$, the contours start from 6σ in steps of 2σ , with $\sigma = 0.27$, 0.19, 0.21, and 0.19 K km s^{-1} .

B. VELOCITY FIELD AND LINE WIDTH DISTRIBUTION OF SOURCES IN THE OTF OBSERVATION

In this section, we present the velocity field and line width distribution of sources in the OTF observation in Figures 41–48 and 49–56.

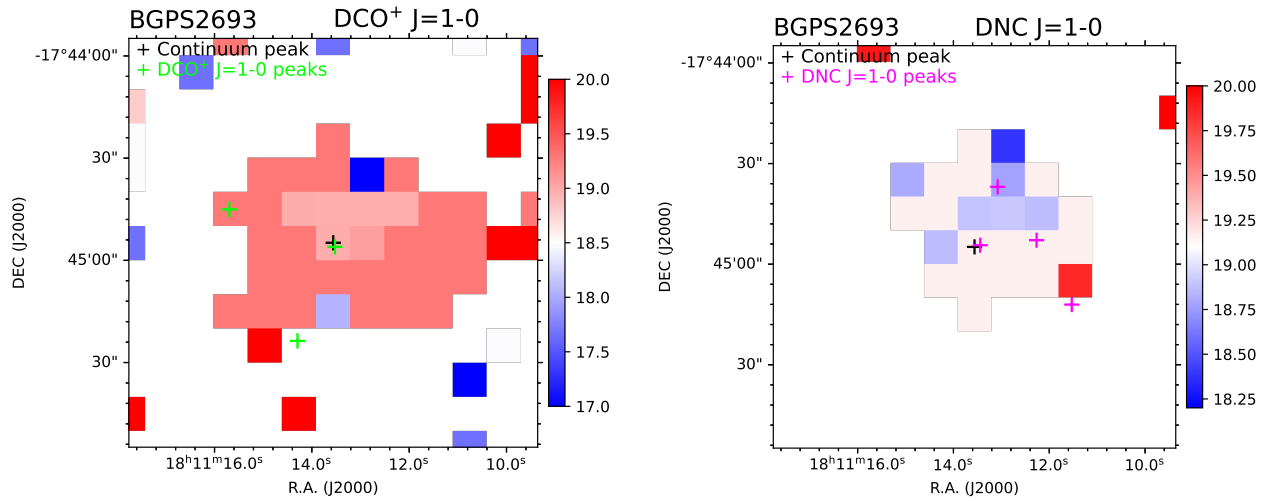


Figure 41. Line width distribution of deuterated molecules for BGPS2693.

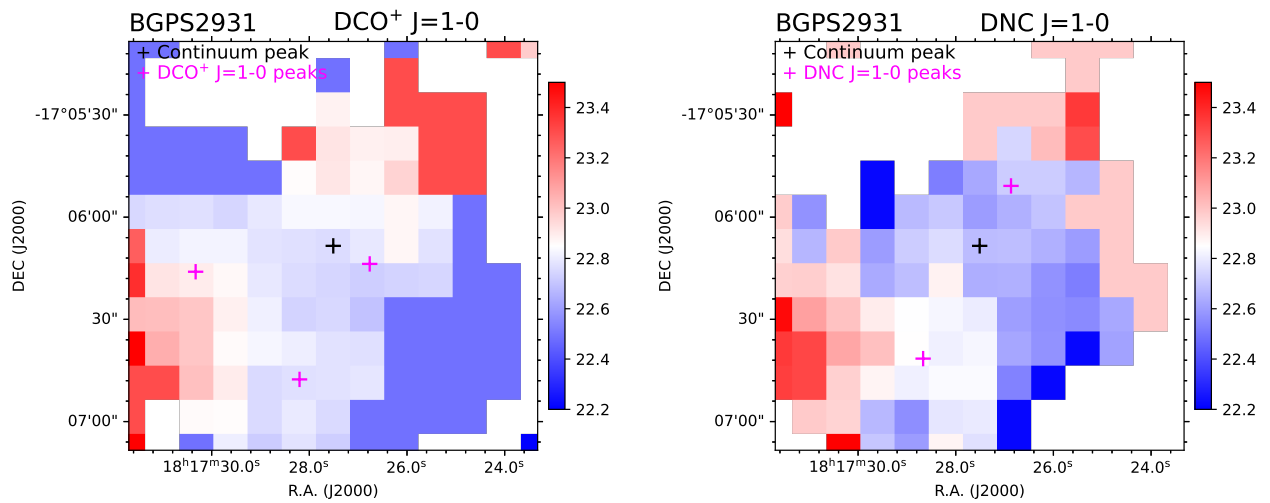


Figure 42. Line width distribution of deuterated molecules for BGPS2931.

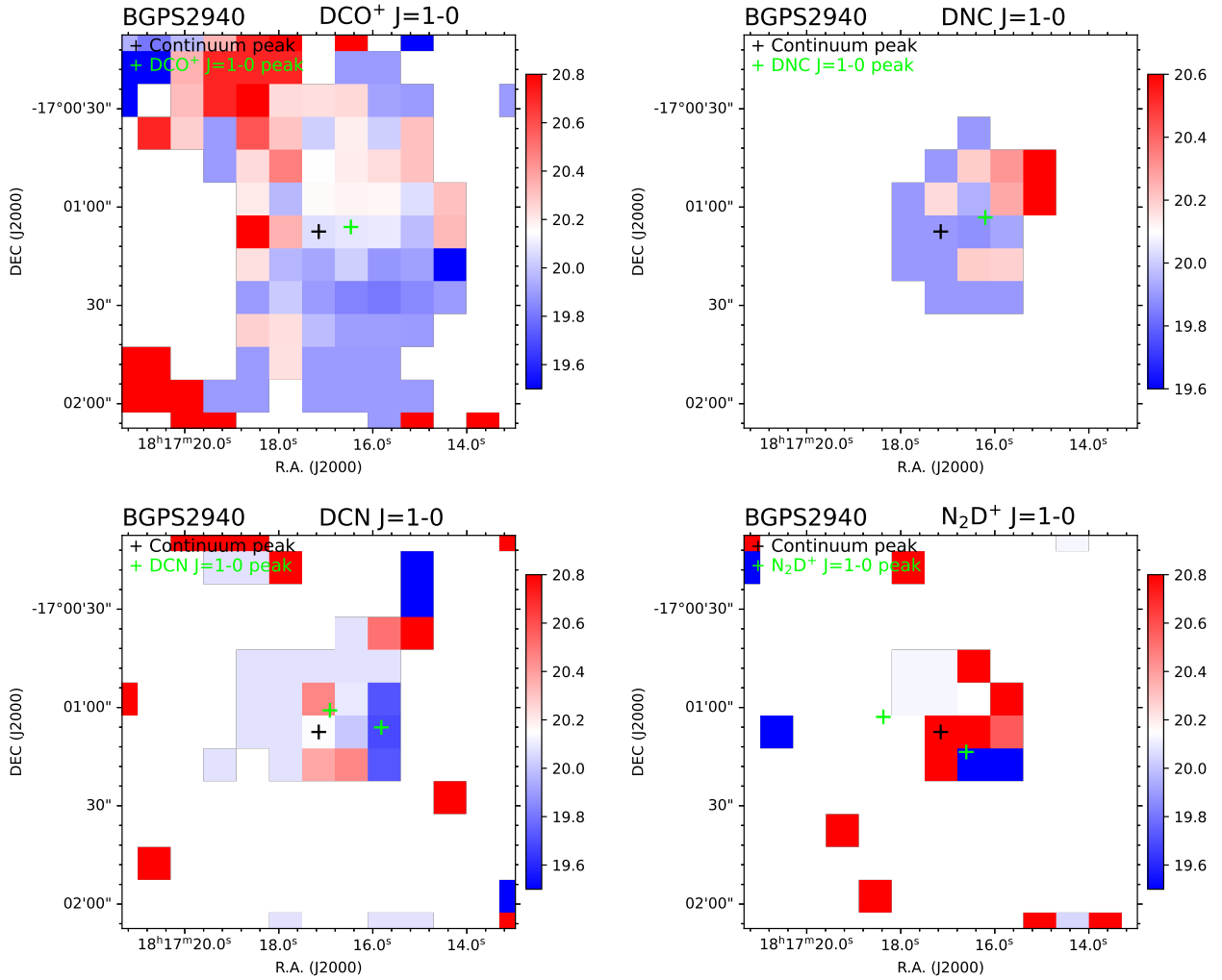


Figure 43. Line width distribution of deuterated molecules for BGPS2940.

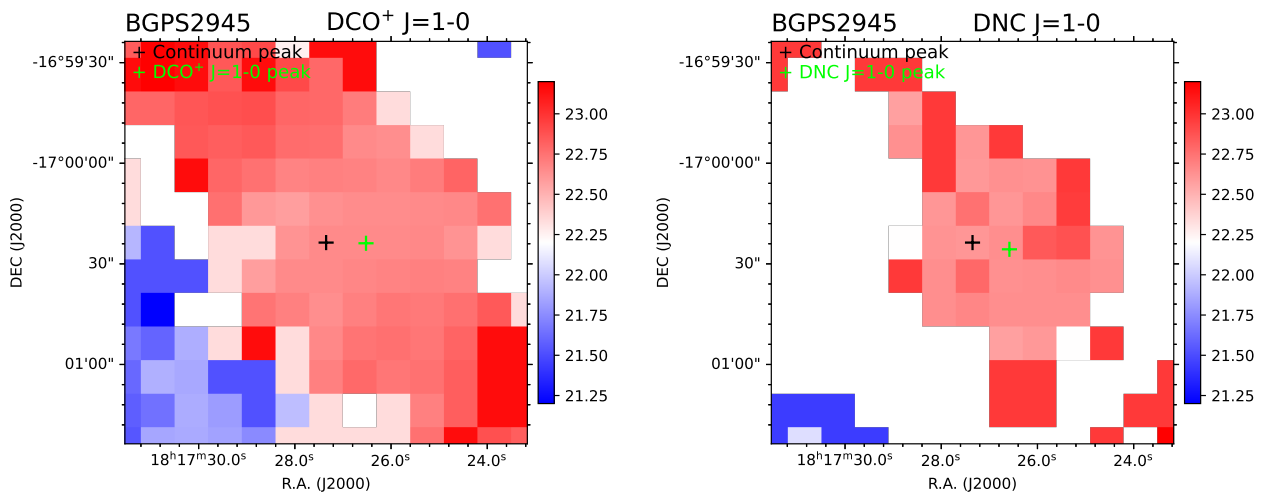


Figure 44. Line width distribution of deuterated molecules for BGPS2945.

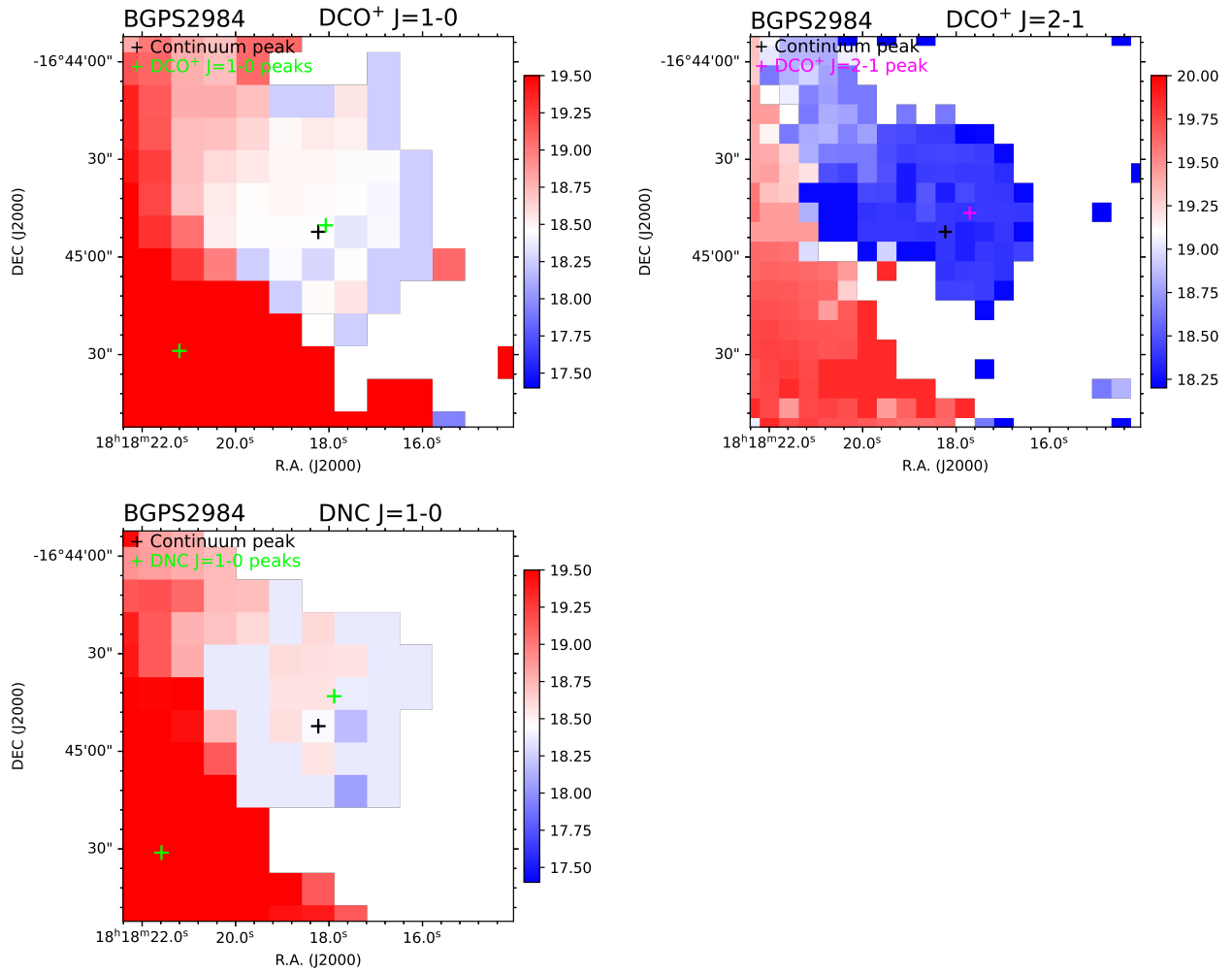


Figure 45. Line width distribution of deuterated molecules for BGPS2984.

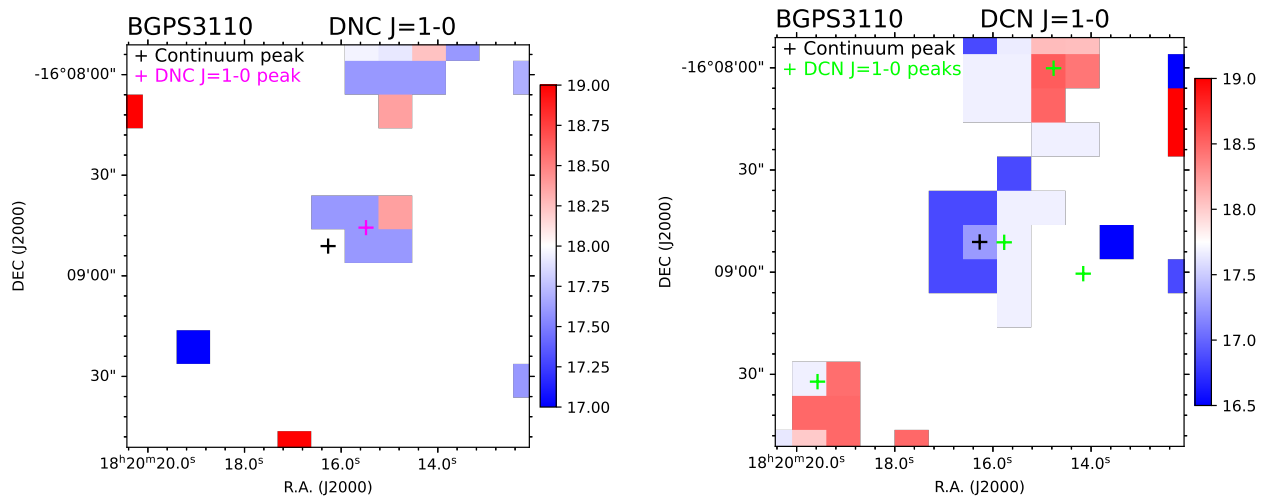


Figure 46. Line width distribution of deuterated molecules for BGPS3110.

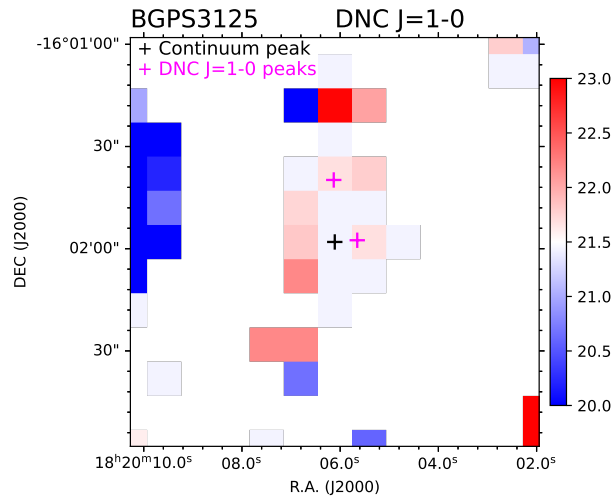


Figure 47. Line width distribution of deuterated molecules for BGPS3125.

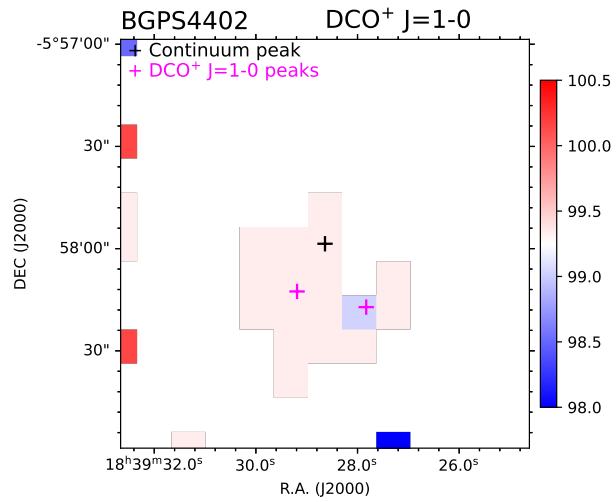


Figure 48. Line width distribution of deuterated molecules for BGPS4402.

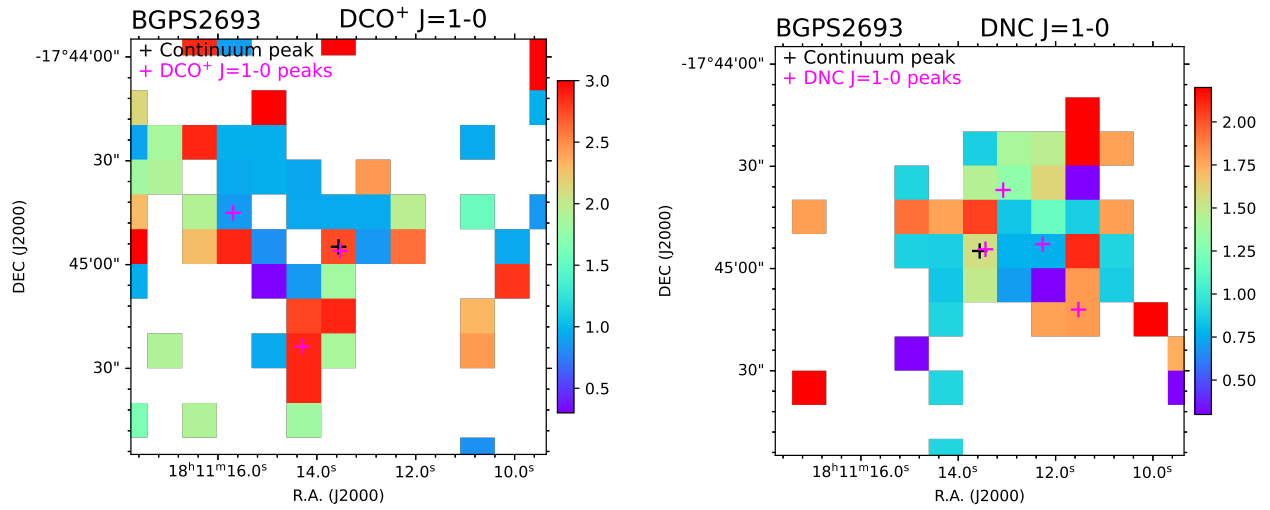


Figure 49. Line width distribution of deuterated molecules for BGPS2693.

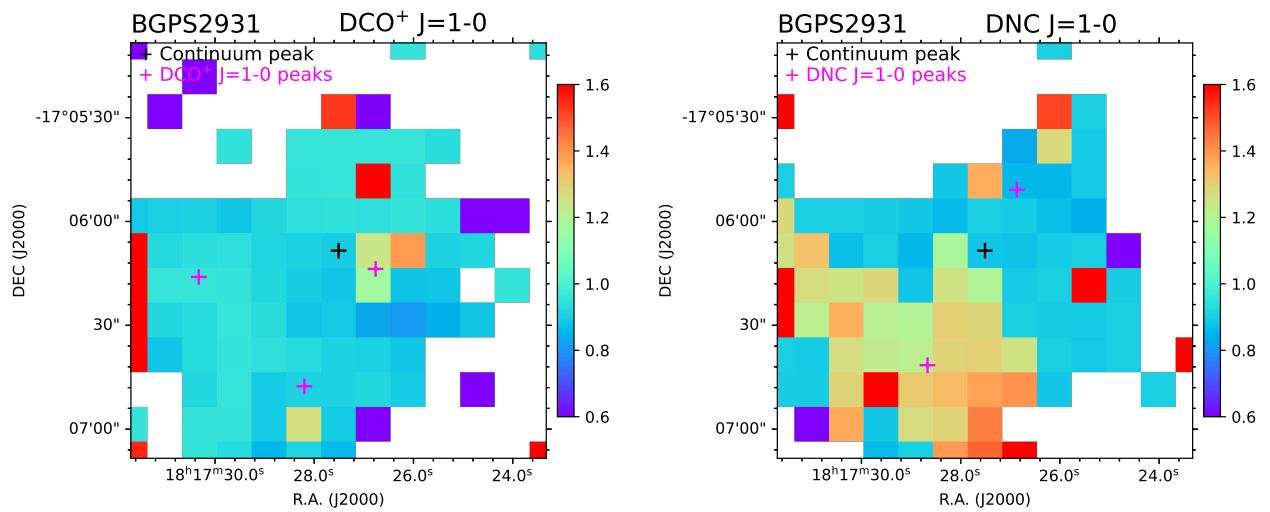


Figure 50. Line width distribution of deuterated molecules for BGPS2931.

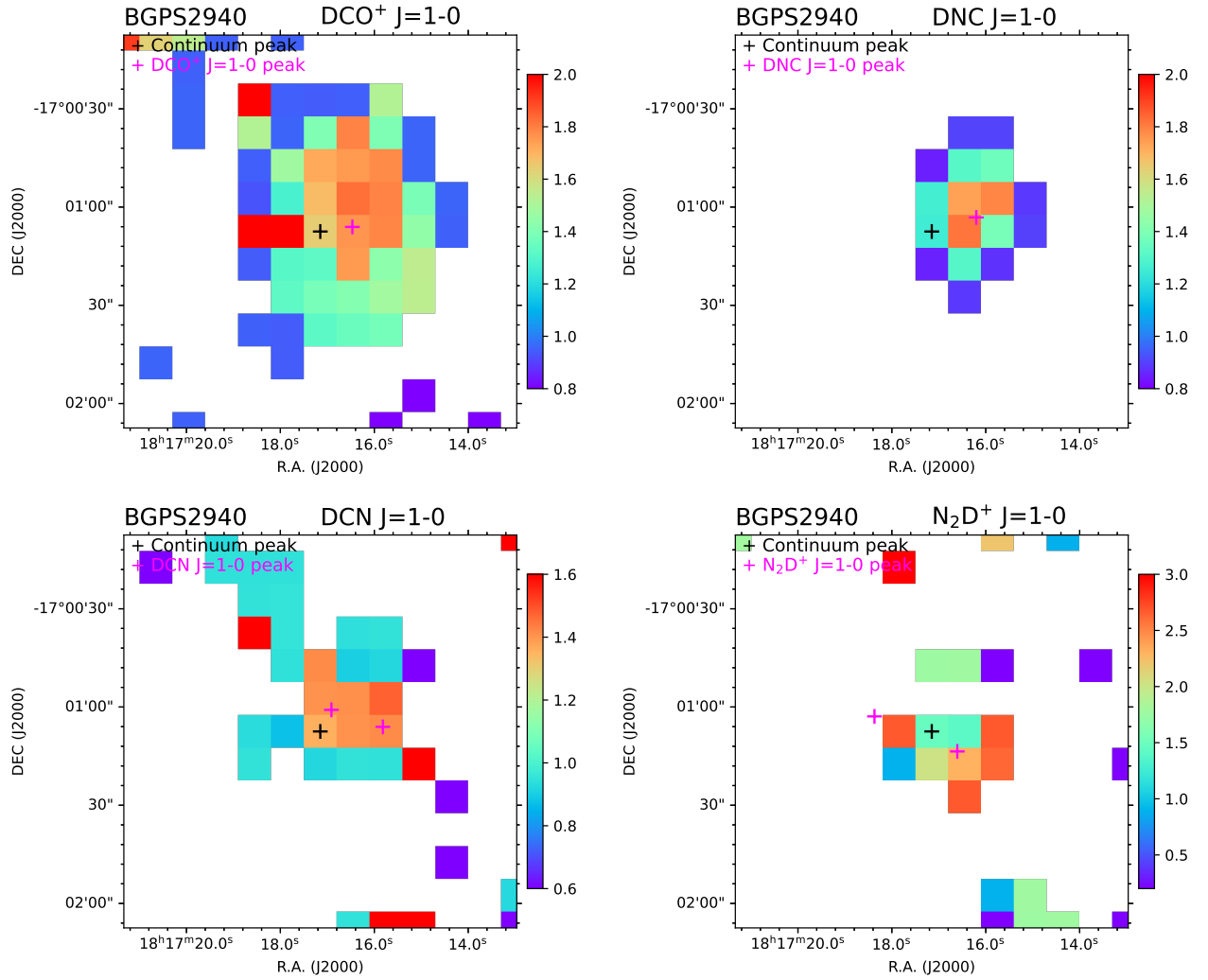


Figure 51. Line width distribution of deuterated molecules for BGPS2940.

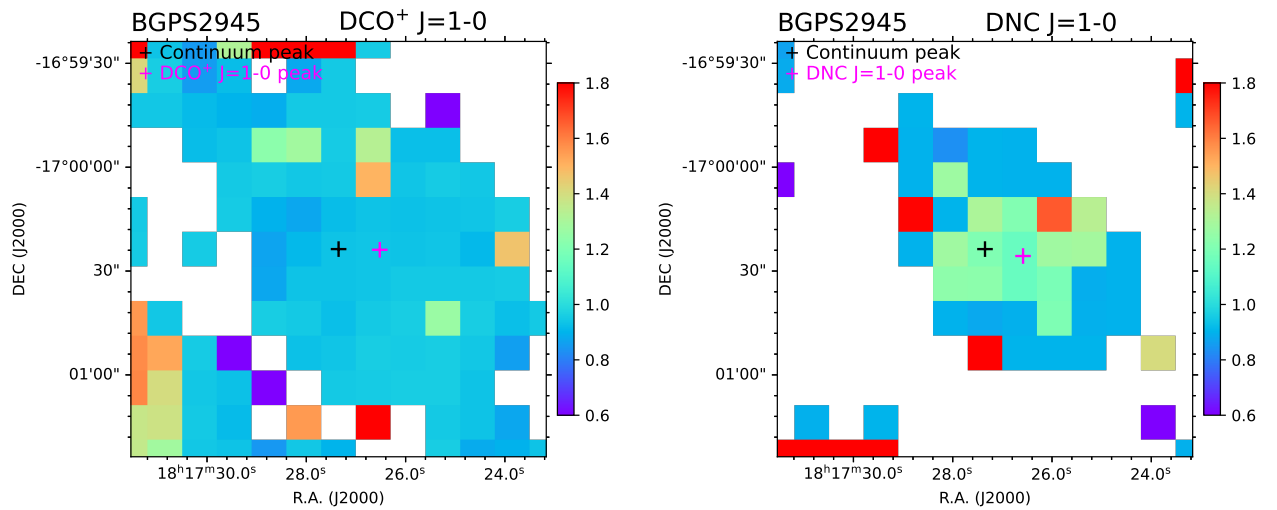


Figure 52. Line width distribution of deuterated molecules for BGPS2945.

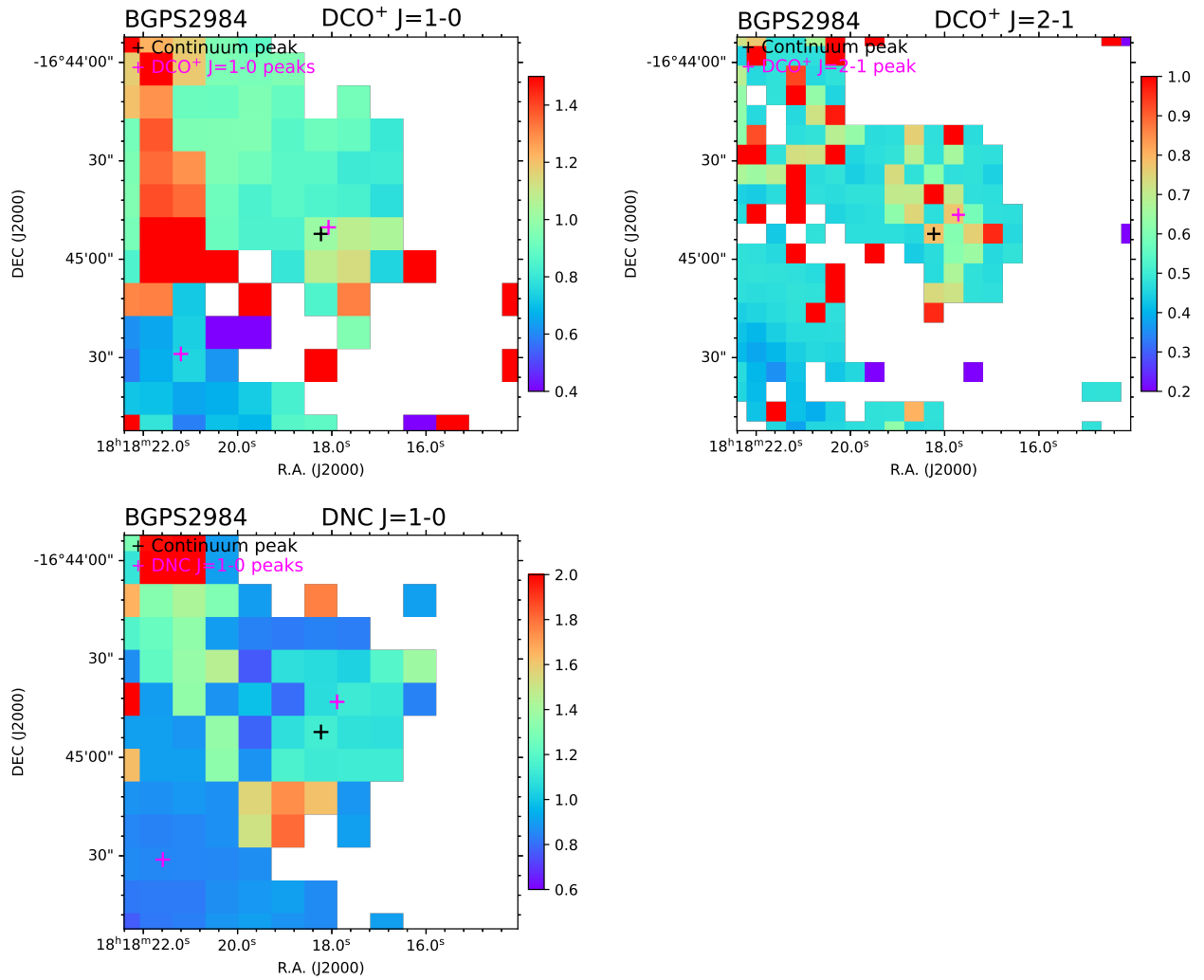


Figure 53. Line width distribution of deuterated molecules for BGPS2984.

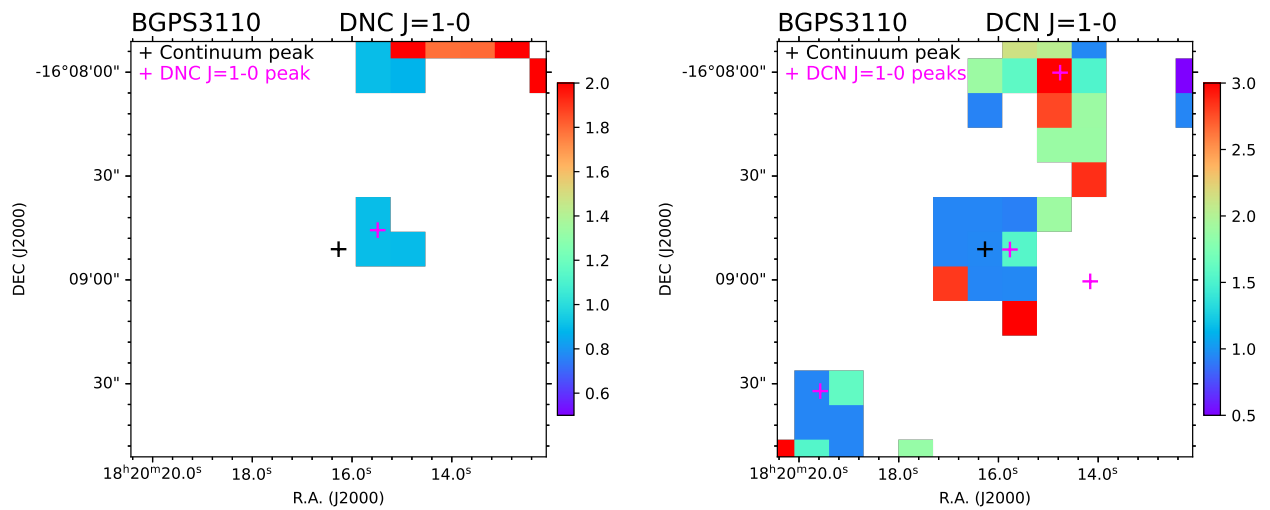


Figure 54. Line width distribution of deuterated molecules for BGPS3110.

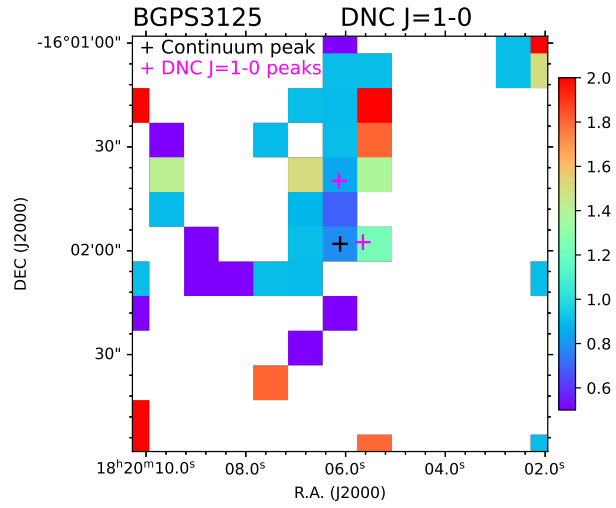


Figure 55. Line width distribution of deuterated molecules for BGPS3125.

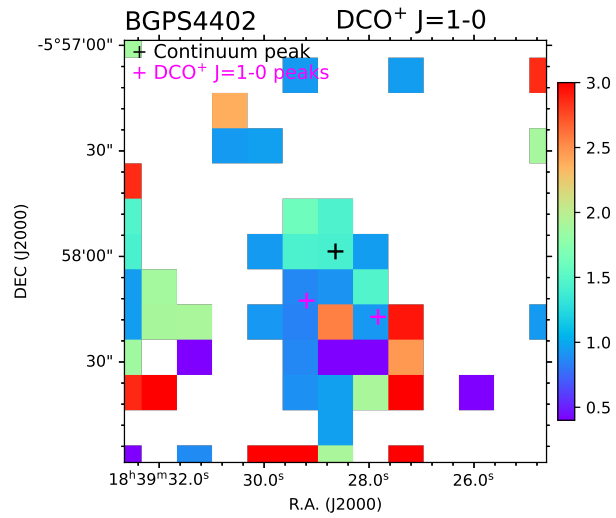


Figure 56. Line width distribution of deuterated molecules for BGPS4402.